

**HEAT TRANSFER ON WHEEL-BRAKE SYSTEM AT CRITICAL  
THERMAL CONDITIONS**

A Thesis

Presented to

The Academic Faculty

by

Pavel Kovalenko

In Partial Fulfillment

of the Requirements for the Degree

Master of Science in the

School of Mechanical Engineering

Georgia Institute of Technology

May 2021

**COPYRIGHT 2021 BY PAVEL KOVALENKO**

**HEAT TRANSFER ON WHEEL-BRAKE SYSTEM AT CRITICAL THERMAL  
CONDITIONS**

Approved by:

Dr. S. Mostafa Ghiaasiaan, Advisor

School of Mechanical Engineering

*Georgia Institute of Technology*

Dr. Comas Haynes

Georgia Tech Research Institute

*Georgia Institute of Technology*

Dr. Zhuomin Zhang

School of Mechanical Engineering

*Georgia Institute of Technology*

Date Approved: 01/21/2021

*To my lovely wife Ellen*

## ACKNOWLEDGEMENTS

First, I would like to express my deepest sense of gratitude to Professor Ghiaasiaan for his patient guidance, encouragement, understanding, and excellent advice throughout this thesis. He has been my advisor and teacher at multiple stages of graduate school, and I could not wish for a better advisor.

I am highly indebted to the George W. Woodruff School of Mechanical Engineering for the tremendous support and resources I have been provided throughout my coursework. I am thankful to the staff and IT support that helped me with my needs working on the thesis remotely. I would like to thank Mrs. Henry for her continuous support with my administrative questions.

I would like to extend my sincere gratitude to my supervisor, Henry Renegar. He inspired my interest in the automotive wheel manufacturing and provided continuous guidance throughout my employment with Superior Industries Int. and graduate coursework. He has been incredibly kind with his knowledgeable advice and proctored all my exams during my Master's tenure. I truly appreciate all that he has done for me.

My sincere appreciation goes to Superior Industries Int. for all the resources I have been provided and the opportunity to become a well-rounded engineer. The thesis topic has been inspired within the walls of Superior Industries during discussions with my colleagues.

Most important thanks and love go to my wife, Ellen, for her inexhaustible support and love. With her on my side, the sun shines a little brighter and my smile is a little wider. A special thanks and love are to my mom, Lidia, and my sister, Anya. Thanks to their love and support, I am who I am now.

# TABLE OF CONTENTS

	Page
ACKNOWLEDGEMENTS	iv
LIST OF TABLES	viii
LIST OF FIGURES	ix
LIST OF SYMBOLS AND ABBREVIATIONS	xiii
SUMMARY	xv
<b>CHAPTER</b>	
1 Introduction	1
1.1 Background	2
1.1.1 History of Brake-Wheel Systems	2
1.1.2 Wheel-Brake System Design	3
1.1.3 Composite Materials in Wheel Design	7
1.2 Purpose	8
2 Literature Survey	11
2.1 Heat Transfer by Convection	11
2.2 Heat Transfer by Thermal Radiation	13
2.3 Thermal Design of Brake System	14
2.4 Numerical Modeling	18
2.5 Closing Remarks	25
3 Simulated System	26

3.1 Computational Model	26
3.2 Meshing Scheme and Grid Convergence	29
4 Theory	32
4.1 Flow Regime	32
4.2 Turbulence Models	34
4.3 Governing Equations	39
4.3.1 Standard $k - \varepsilon$ Model	43
4.3.2 Standard $k - \omega$ Model	44
4.3.3 Shear Stress Transport (SST) $k - \omega$ Model	46
4.3.4 Turbulent Heat Transfer	47
4.3.5 Near-Wall Turbulence Modeling and Wall Functions	48
4.4 Calculated Parameters	52
4.5 Inlet, Initial, and Boundary Conditions	55
5 Results and Discussion	57
5.1 General Remarks	57
5.1.1 Convergence	58
5.1.2 Grid Dependency Study	58
5.2 RANS Turbulent Models Comparison	60
5.2.1 Aerodynamic Results	61
5.2.2 Heat Transfer Results	65
5.3 Effect of Parameter Variations on Heat Transfer	68
5.3.1 Parametric Tests	68

5.3.2 Aerodynamic Results	69
5.3.3 Heat Transfer Results	74
5.4 Brake System Configurations Comparison	83
5.4.1 Aerodynamic Results	83
5.4.2 Heat Transfer Results	87
6 Conclusion and Recommendations	89
6.1 Concluding Remarks	89
6.2 Recommendations for Future Work	90
APPENDIX A: Additional Equations	92
APPENDIX B: ANSYS Fluent Results Side View	94
REFERENCES	96

## LIST OF TABLES

	Page
Table 4.1: List of Evaluated Parameters Figure 1.2: Overview of Wheel Areas	52
Table 4.2: List of Post-Processing Results Calculated with ANSYS Fluent	54
Table 4.3: Air Properties for an Incompressible Fluid	55
Table 4.4: Wheel's angular velocity as a function of vehicle velocity	56
Table 5.1: Details on various grid configurations with estimated parameters	58
Table 5.2: Monitored variables on the wheel-brake system using the RANS models	59
Table 5.3: Varied parameters	67
Table 5.4: Calculated Parameters for brake rotor with and without vents	86

## LIST OF FIGURES

	Page
Figure 1.1: Wheel-Brakes System [1]	2
Figure 1.2: Overview of Wheel Areas	4
Figure 1.3: The Basic Disc Brake System Design (wheel not depicted) [6]	5
Figure 1.4: The 3D View of the Brake System	5
Figure 1.5: The Basic Front Disc Brake System Design (Back View) [7]	6
Figure 1.6: Polyetherimide/Carbon Fiber Composite Wheel Developed by Sabic, Kringlan Composites [8]	7
Figure 1.7: Overheated Brakes [9]	9
Figure 1.8: Porsche Dyno test [10]	9
Figure 2.1: Simplified Analytical Problem [12]	12
Figure 2.2: Schematic Representation of the CFD Airflow Cooling for the Brakes and the Engine [18]	15
Figure 2.3: Temperature Measurement on the Brake Disc with an Infrared Camera [11]	16
Figure 2.4: Brake Temperature versus Time for Multiple Brake Applications [19]	17
Figure 2.5: Temperatures on Three Different Brake Disc Styles during Braking [11]	18
Figure 2.6: Three Brake Discs (a) Solid (b) with Vents (Read Left to Right) [22]	19
Figure 2.7: Temperature Variation through Radius on Both Designs	20

Figure 2.8: Variation of Heat Transfer Coefficient of Various Surfaces for three Different Brake Discs	21
Figure 2.9: Air Velocity Streamlines for Two Different Duct Designs	22
Figure 2.10: Surface HTC per Part. The Values are Compared to the Baseline HTC	22
Figure 2.11: Velocity Vectors with Magnitude and Streamlines through the Vents	23
Figure 2.12: Heat Transfer Increase due to Radiation on Various Brake Disc Surfaces at Different Temperatures	24
Figure 3.1: Schematic Illustration of the Computational Model	26
Figure 3.2: Section View of Wheel with Tire and Solid Brake Disc	27
Figure 3.3: Section View of Wheel with Tire and Brake Disc with Vents	28
Figure 3.4: Wheel-Brake System in Simulation Domain	30
Figure 3.5: Illustration of Refined Mesh around the Wheel	31
Figure 3.6: Inflated Mesh next to Solid Surfaces for Capturing Flow Boundary Layer	32
Figure 4.1: Qualitative Presentation of the Energy Spectrum in Isotropic Turbulence [28]	33
Figure 4.2: Classification of Turbulence Models [29]	35
Figure 4.3: Turbulence Resolution by Three Leading Computational Approaches [30]	36
Figure 4.4: Popular RANS Turbulence Models	37
Figure 5.1: Depiction of the plane for the illustration of the results	60
Figure 5.2: Velocity profile for a)Realizable $k - \varepsilon$ , b)Standard $k - \omega$ c) SST $k - \omega$	61

Figure 5.3: Pressure profile for a) Realizable $k - \varepsilon$ , b) Standard $k - \omega$ c) SST $k - \omega$	62
Figure 5.4: Kinetic Energy for a) Realizable $k - \varepsilon$ , b) Standard $k - \omega$ c) SST $k - \omega$	63
Figure 5.5: Temperature of the air for a) Realizable $k - \varepsilon$ , b) Standard $k - \omega$ c) SST $k - \omega$	65
Figure 5.6: Temperature on the surface of the wheel for a) Realizable $k - \varepsilon$ , b) Standard $k - \omega$ c) SST $k - \omega$	66
Figure 5.7: Mass Flow Rate	68
Figure 5.8: Drag Coefficient	69
Figure 5.9: Air velocity for vehicle velocities a) 0.1 m/s, b) 1 m/s, c) 3 m/s, d) 6 m/s, e) 10 m/s	70
Figure 5.10: Pressure for vehicle velocities a) 0.1 m/s, b) 1 m/s, c) 3 m/s, d) 6 m/s, e) 10 m/s	71
Figure 5.11: Kinetic Energy for vehicle velocities a) 0.1 m/s, b) 1 m/s, c) 3 m/s, d) 6 m/s, e) 10 m/s	72
Figure 5.12: Inner Rim Surface Temperature vs. Vehicle Velocity for variable brake rotor temperatures	73
Figure 5.13: Heat Flux on the rim vs. vehicle velocity for variable brake rotor temperatures	74
Figure 5.14: Rim Heat Transfer Coefficient vs. vehicle velocity for variable brake rotor temperatures	75
Figure 5.15: Nusselt Number on the rim vs. vehicle velocity for variable brake rotor Temperatures	75

Figure 5.16: Heat transfer coefficient versus temperature on the inner rim surface for various parametric variables	76
Figure 5.17: Air Temperature at the vehicle velocity 0.1 m/s and a) 300°C, b) 400°C, c) 500°C, d) 600°C	77
Figure 5.18: Air Temperature at the vehicle velocity 1 m/s and a) 300°C, b) 400°C, c) 500°C, d) 600°C	78
Figure 5.19: Air Temperature at the vehicle velocity 3 m/s and a) 300°C, b) 400°C, c) 500°C, d) 600°C	79
Figure 5.20: Air Temperature at the vehicle velocity 6 m/s and a) 300°C, b) 400°C, c) 500°C, d) 600°C	80
Figure 5.21: Air Temperature at the vehicle velocity 10 m/s and a) 300°C, b) 400°C, c) 500°C, d) 600°C	81
Figure 5.22: Air velocity for a) Solid rotor b) rotor with vents	82
Figure 5.23: Pressure for a) Solid rotor b) rotor with vents	83
Figure 5.24: Kinetic Energy for a) Solid rotor b) rotor with vents	83
Figure 5.25: Air velocity vectors inside the vented rotor	84
Figure 5.26: Air velocity vectors inside the vented rotor (close-up view)	85
Figure 5.27: Air temperature for a) solid rotor b) vented rotor	87
Figure 5.28: Air temperature for a) solid rotor b) vented rotor (Side View)	87
Figure B.1: Velocity profile for a)Realizable $k - \varepsilon$ , b)Standard $k - \omega$ c) SST $k - \omega$	93
Figure B.2: Pressure profile for a)Realizable $k - \varepsilon$ , b)Standard $k - \omega$ c) SST $k - \omega$	93
Figure D.3: Kinetic Energy profile for a) Realizable $k - \varepsilon$ , b) Standard $k - \omega$ c)	

SST  $k - \omega$

94

Figure D.4: Kinetic Energy profile for a) Realizable  $k - \varepsilon$ , b) Standard  $k - \omega$  c)

SST  $k - \omega$

94

## LIST OF SYMBOLS AND ABBREVIATIONS

$C_d$	Drag coefficient
$D$	Outer tire diameter (m)
$D_h$	Hydraulic diameter (m)
$E$	Eddy diffusivity ( $m^2/s$ )
$E$	Turbulence energy spectrum functions based on wave number ( $m^3/s^2$ )
$E_{th}$	Eddy diffusivity for heat transfer ( $m^2/s$ )
$\vec{g}$	Gravitational acceleration vector ( $m/s^2$ )
$h$	Heat transfer coefficient ( $W/m^2 K$ ); height (m)
$k$	Turbulence kinetic energy (J/kg); Thermal conductivity ( $W/m K$ )
$L$	Length (m)
$l$	Length (m)
$l_c$	Characteristic length (m)
$l_D$	Kolmogorov's microscale (m)
$l_M$	Turbulence mixing length (m)
$l_{th}$	Turbulence mixing length for heat transfer (m)
NS	Navier-Stokes equation
$Nu_l$	Nusselt number $hl / k$
$P$	Pressure ( $N/m^2$ )
Pr	Prandtl number = $\mu C_p / k$

$Pr_{tu}$	Turbulent Prandtl number
$p$	Perimeter (m)
$Q$	Volumetric flow rate ( $m^3/s$ )
$q''$	Heat flux ( $W/m^2$ )
$R$	Radius (m)
Re	Reynolds number = $\rho U l/\mu$
$T$	Temperature (K)
$t$	Time (s); thickness (m)
$U$	Internal Energy (J)
$\vec{U}$	Velocity vector (m/s)
$U$	Velocity (m/s)
$U_\tau$	Friction velocity (m/s)
$u$	Velocity in x direction in Cartesian coordinates (m/s)
$u_D$	Kolmogorov's velocity scale (m/s)
$V$	Volume ( $m^3$ )
$v$	Velocity in y direction in Cartesian coordinates (m/s)
$w$	Velocity in z direction in Cartesian coordinates (m/s)
$y$	Normal distance from the nearest wall (m)
$\alpha$	Thermal diffusivity ( $m^2/s$ )
$\delta$	boundary-layer thickness (m)
$\varepsilon$	radiative emissivity; turbulent dissipation rate (W/kg)

$\lambda$	Wavelength (m); second coefficient of viscosity ( $-\frac{2}{3}\mu$ ) (kg/m s)
$\mu$	Viscosity (kg /m s)
$\nu$	Kinematic viscosity (m <sup>2</sup> /s)
$\rho$	Density (kg/m <sup>3</sup> )
$\tau$	viscous stress (N/m <sup>2</sup> )
$\Phi$	Dissipation function (s <sup>-2</sup> )
+	In wall units
·	Time rate
–	Average
in	inlet
lam	Laminar
max	Maximum
tu	Turbulent
$\infty$	Ambient; fully developed
=	Tensor
CFD	Computational fluid dynamics
DES	Detached eddy simulation
DNS	Direct numerical simulation
LES	Large-eddy simulation
RANS	Reynolds-averaged Navier-Stokes
RNG	Renormalized group
RSM	Reynolds Stress Model

## SUMMARY

The increasing efforts in the automotive industry to reduce overall vehicle weight has led to the development of components made out of lighter materials such as composite materials. Further development of the composite materials has made it feasible to manufacture automotive wheels made out of the reinforced thermoplastic composites. The latest composite wheels utilize thermoplastic matrix bonding the carbon fibers. The plastics exhibit a reduced thermal strength compared to metal alloys; therefore, it is necessary to understand the behavior of the thermoplastics exposed to the radiation heat transfer from the brake system at critical thermal conditions. This study investigated the aerodynamic effects and heat transfer phenomena on the wheel-brake system. The radiative and convective heat transfer processes were investigated on a model of the wheel-brake system of the front axle of a vehicle. The front axle and the vehicle, for computational feasibility, were not included in the numerical model. The mass, momentum, and energy conservation equations were solved. The average heat transfer coefficient, average Nusselt number, average heat flux, and the average temperature on the inner surface of the wheel were estimated as a function of the incoming air stream velocity and the brake disc temperature. The computational analysis revealed that the radiative heat transport is the dominant source of heating of the wheel's inner surface. The average temperature on the wheel inner surface increases with the increasing temperature of the brake disc and decreasing velocity of the vehicle. The average heat transfer coefficient on the inner surfaces of the rim increases with the increasing vehicle velocity and the increasing temperature on the inner surface of the rim. Finally, the heat

transfer phenomena were compared for the cases of the brake disc with and without vents. It was found that the vents have insignificant impact on the heating of the wheel.

## CHAPTER 1

### INTRODUCTION

The ongoing efforts for the weight reduction of all components in the modern vehicles drives the wheel manufacturers to consider implantation of composite materials for the wheels on the mass-produced vehicles. The composite materials provide a substantial weight reduction of a produced component by maintaining the required stiffness and the ultimate strength of the product. One particular brake-wheel system shown in Figure 1.1, is a common system that many car manufacturers apply on their vehicles of new generations.

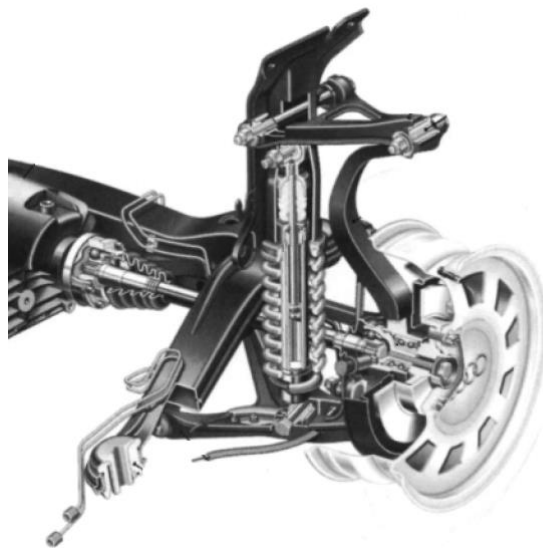


**Figure 1.1:** Wheel-Brakes System [1]

The wheel represents the components that experience the mechanical stresses due to road conditions and require a careful analysis of the wheel design. Since the light-weight materials

are increasingly used in the wheel design, proper analysis and accurate physical models of the thermal processes within the suspension model are needed. A proper rim design of a wheel is a critical part of the structural stability and safety of the whole vehicle. The goal of this study is to investigate the convective and radiative heat transfer among the wheel rim, brake rotor, and brake caliper occurring during critical braking conditions, which corresponds to overheated components. The different vehicle velocity cases are investigated for one wheel's design to get a general understanding of the physics of this system. Different wheel designs, and hence different resulting heat transfer correlation are expected to occur, which will be investigated in the future.

## **1.1 Background**

### 1.1.1 History of Brake-Wheel Systems

The automotive brake system finds its origins in preceding mechanical applications such as bicycles, steam machinery, etc. In 1902, Louis Renault patented a design of a first internal drum brake, which was used on the 1906 Ford Model N. As the cars were getting heavier, the necessary braking forces consequently increased, which required a more efficient brake system design. F.W. Lanchester's patent of 1902, where brake pads act on the both sides of the brake disc surface, offered higher braking forces and could bring a larger

vehicle to a stop faster. The design, however, was more complex and expensive compared with the competing brake designs of the time, so it was utilized only on occasional vehicles of WWII [2]. Only when the brake discs were equipped with a floating caliper, which made it less expensive to fabricate and easy to maintain, the other brake designs lost its popularity. The first mass-produced vehicle with brake discs was Citroën DS-19 and was available to the public in 1955 [3]. Current brake system development focuses on the reduction of the mass. The heavy cast iron brake discs can now be replaced with ceramic C/SiC brake discs, which have excellent mechanical and thermal properties; however, the mass production of such brake discs is still cost-prohibitive and applied mostly on sports cars [4].

### 1.1.2 Wheel-Brake System Design

The wheel consists of several areas with a naming, generally, standardized by the automotive manufacturers, however, it can vary. Figure 1.2 shows a wheel with the most important areas whose naming will be used in the description of the wheel. This study has particular interest in the heat transfer on the rim and the spokes of the wheel, the hub is expected to have a minimal impact from the radiative and convective heat transfer. However, it is possible that the conduction from the brake disc might have a much stronger effect on it. The conduction to the hub from the brake disc would reduce the temperature of the brake disc moving its surface temperature to a lower range.

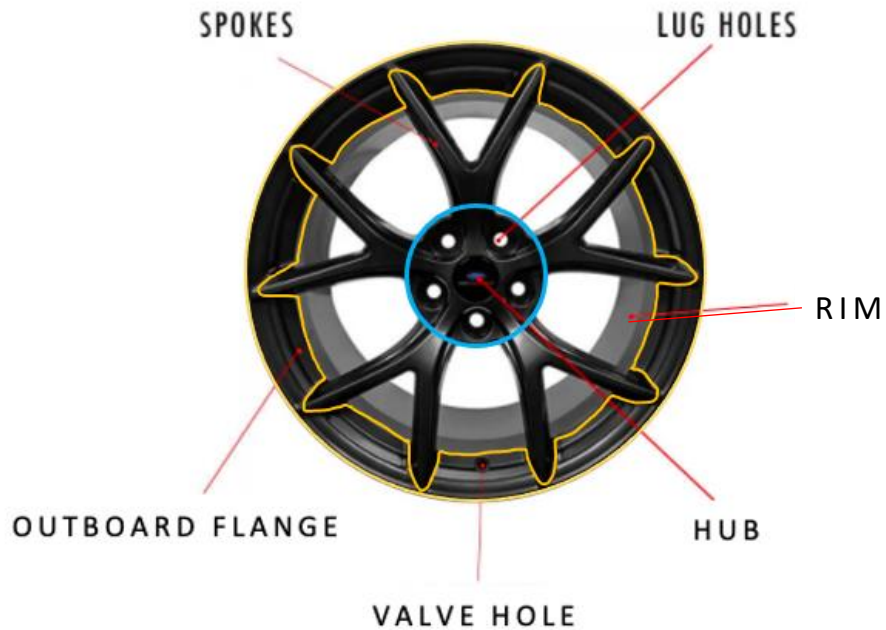


**Figure 1.2:** Overview of Wheel Areas

The basic disc brake system can be seen in Figure 1.3 and Figure 1.4 (wheel not shown). The disc and the wheel that is connected to it rotate together, while the pads of a brake caliper are fixed on a static frame. When braking, the brake pads press against the disc with the assistance of a hydraulic system actuated by a driver. The required magnitude of the friction force that acts on the disc depends on the size of the disc. The larger the disc diameter the smaller the magnitude of the friction force that is necessary to stop a vehicle and vice versa, when the braking power is set equal for both cases. On a smaller brake disc, a higher pressure has to be applied on the pads, which translates into the higher heat generation on the brake system. Therefore, an effective cooling system for the brakes has to be incorporated as well [5].

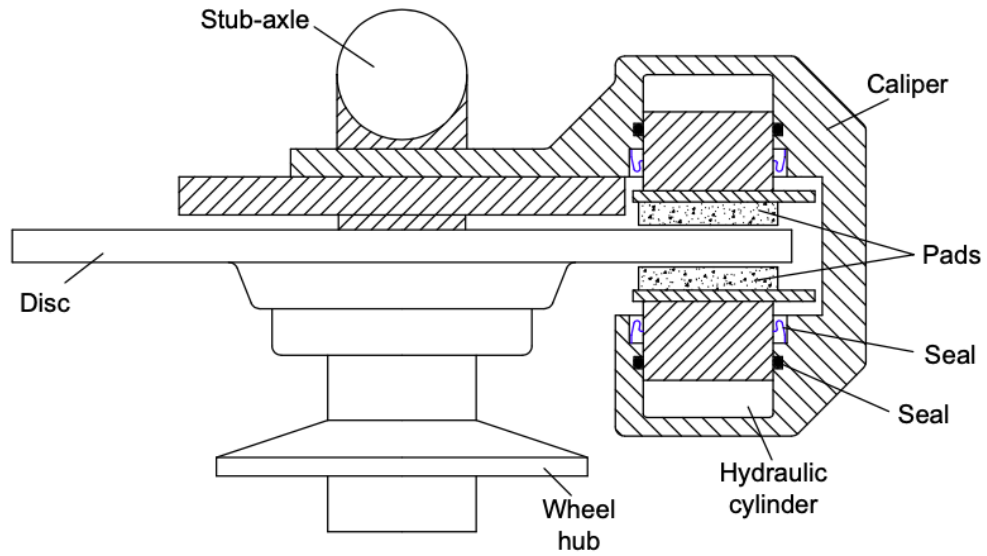


**Figure 1.3:** The Basic Disc Brake System Design (wheel not depicted) [6]



**Figure 1.4:** The 3D View of the Brake System

The brake system is designed in a way that a vehicle is able to pass some specified industry and safety requirements. A couple of these requirements are a set length of a braking path at a given initial velocity and a limit of discs temperature, that is allowed in normal operating conditions. As the braking distances need to be relatively short, a lot of resulting heat is generated at the braking system through friction between the pads and the discs. The heat is transferred through pads and disc to all surrounding components through conduction, convection, and radiation. Figure 1.5 depicts the components which are subject of the most impact of the generated heat. A typical performance car has larger brake calipers and discs, which are radially constrained by the inner rim diameter of the wheel with a specified clearance among these components.



**Figure 1.5:** The Basic Front Disc Brake System Design (Back View) [7]

The greatest amount of braking force and, therefore, the highest thermal stresses are experienced at the front wheels, as during the braking the additional weight of the vehicle tends to move forward caused by inertial forces. To address this factor, a front axle of

modern vehicles typically has larger discs equipped with internal venting channels to extract accumulated heat through convection of propelled air streams within them.

### 1.1.3 Composite Materials in Wheel Design

The continuous efforts of reducing the vehicle weight drive the development of vehicle's components from being made of cast iron or metal-based alloys to reinforced thermoplastic composites with comparable stiffness and strength. That is accomplished by significantly reducing the weight of the redesigned components. The wheels on most cars of today are primarily made of steel and aluminum alloys. Some performance car manufacturers and engineering institutions have already started implementing carbon fiber reinforced plastics in developing the entire wheel. Figure 1.6 depicts one of these wheels.



**Figure 1.6:** Polyetherimide/Carbon Fiber Composite Wheel Developed by Sabic, Kringlan Composites [8]

The cost of production still prohibits the mass-production of cars with composite wheels, but efforts are continuously being made to reduce the manufacturing cost.

## **1.2 Purpose**

The previous sections discussed the current stand of technology in the design of brake-wheel system and the increasing implementation of thermoplastic composites in the design of automotive wheels. The thermoplastics are a great matrix material for binding the reinforcing fibers, however, they have a much lower melting point than the metals commonly used for fabrication of the wheels. As it can be seen in Figures 1.7 and 1.8 the extreme operating conditions can heat up the brake discs to glowing temperatures. The accumulated heat in the discs dissipates through conduction, convection, and radiation to the surrounding vehicle components and the air stream. It is important that these heat transfer processes dispose of the heat efficiently so that the temperature on the brake disc does not reach a certain threshold. It has been experimentally demonstrated that the brake disc can reach temperatures of up to 700 °C. At temperatures above 600 °C, however, the tribological properties of the brake pads significantly deteriorated [4]. At such elevated temperatures more heat radiates to the wheels. It is also possible that in certain wheel designs, which do not allow much air circulation, the heat can be transferred by convection from discs to the wheel. If the wheel is made of a thermoplastic material, it can heat up to a temperature at which the thermoplastic can lose its structural stability.



**Figure 1.7:** Overheated Brakes [9]



**Figure 1.8:** Porsche Dyno test [10]

The purpose of this study is to investigate the heat transfer phenomena occurring between the brake system and the wheels. The aerodynamic effects of the air stream between these components are also analyzed to demonstrate whether it is crucial to have a certain degree of air circulation to guarantee effective cooling of a wheel and the braking system. The convective and radiation heat transfer as well as thermal dispersion are calculated and analyzed with the aid of numerical solutions of the momentum and thermal energy equations. A few turbulence models are compared and discussed in terms of their performance and robustness. The experimental results for verification of the obtained simulations are not available for this simulated system, however, this work provides a valuable initial insight in the heat transfer phenomena on the wheel-brake system.

## CHAPTER 2

### LITERATURE SURVEY

#### 2.1 Heat Transfer by Convection

The convective heat transfer on the wheel-brakes system depends, for the most part, on the geometry of the wheel, if the initial conditions are set the same. The boundary conditions on the wheel surface would differ though, as the wheel geometry, observed in a complex dynamic system, dictates the resulting boundary layer forming on the wheel. For example, for a wheel without any windows between its spokes, the convective heat transfer rate is expected to decrease, as the air gets entrapped in the region between the wheel and the brakes, which, consequently, would lead to heating up of this air to the temperature of its surroundings. Car manufacturers consider that effect when designing a wheel-brakes system for new vehicles [11]. The aerodynamic effects induced by the window design of a wheel in this study will be briefly discussed in another chapter.

There have been developed a few simplified analytical models of the cooling of a rotating disc by a air stream of the ambient temperature that has its inlet velocity vector parallel to the vector of the disc's angular velocity. Figure 2.1 illustrates the concept of this problem. The solution of this problem gives an approximate solution for the air flow field, heat transfer coefficients on the disc's surface, and the resulting heat flux on the disc-air interface.

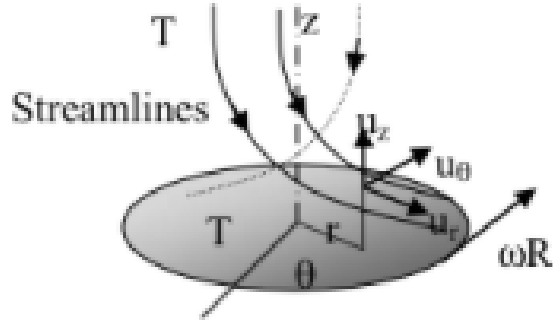


**Figure 2.1:** Simplified Analytical Problem [12]

The surface heat flux is obtained from the temperature difference between the disc surface and the air film immediately next to the surface

$$\dot{q}_{conv} = h(T_{disc} - T_{film}) \quad (2.1)$$

The heat transfer coefficient can be derived from the equation below

$$h = \frac{k_{disc}(\partial T/\partial n)|_{solid}}{T_{disc} - T_{film}} = \frac{k_{film}(\partial T/\partial n)|_{fluid}}{T_{disc} - T_{film}} \quad (2.2)$$

Nondimensionalized representation of the local heat transfer coefficient can be obtained from

$$Nu = \frac{hL}{k_{film}} \quad (2.3)$$

The solution of these equations, consequently, allows the estimation of the temperature field of the air stream. This study, however, solves this heat transfer problem numerically, taking in account the complex geometry and turbulence models, but the principle remains the same.

## 2.2 Heat Transfer by Thermal Radiation

The second mechanism by which the brakes emit heat to the environment is thermal radiation. The radiation heat transfer is mostly significant when a large temperature difference exists between the emitting body and its surrounding. The Stefan-Boltzmann law (2.4) illustrates that the heat transfer rate dependency on the temperature is to the power of four. For an isothermal object surrounded by a large, isothermal enclosure, for example, the radiative heat transfer rate from the object to the enclosure is

$$\dot{Q}_{rad} = \varepsilon\sigma_b A(T_{brake}^4 - T_{sur}^4) \quad (2.4)$$

That makes the radiation an important element of heat transfer on the wheel-brakes system, as the temperatures on the disc reach 700 °C in certain cases. Noyes and Vickers (1969) and Limpert (1975) estimated that the radiation from the brake discs at the normal braking conditions accounts for less than 5 percent of the total heat dissipated [13]. That applies for the case when a significant amount of heat is dissipated by convection instead of radiation. If the convective heat transfer is less efficient then it implies that the radiation will account for a larger percentage of the dissipated heat.

The emissivity value for a disc and the wheel varies depending on the surface finish and the temperature. For the polished cast iron, the emissivity value is 0.64. This number is used in this study. The same value has been used for an experimental work on the brake disc cooling by Stephens [14].

### **2.3 Thermal Design of Brake System**

Before a brake system is ready to be integrated into the final design of the vehicle, a detailed thermal and structural analysis of the brakes has to be performed in order to meet various criteria, which primarily center around vehicle safety requirements. These requirements are set by the National Highway Traffic Safety Administration (NHTSA) to make sure that the vehicles are safe to drive in most of the road situations. On most major vehicles, the NHTSA independently performs validation tests to monitor the compliance of the vehicle design with its standards. For example, its brake test includes measurement of the total braking distance, maximum pedal force, and brake lining temperature among others. The OEMs also perform their brake tests internally, often specifically designed for a particular vehicle. Within the industry the brake test can have a different methodology and set of measured data, depending on the preferences of the manufacturer. It is a rule, however, to perform a brake cooling analysis for a new vehicle, as the roads with high speed limits and traffic density increase the need for more effective cooling of the brakes.

The insufficient brake cooling increases the risk of thermal brake failure such as brake fade and fluid vaporization, reduced component life, wheel bearing damage, and damaged seals. These failures are caused primarily by the conduction among the components. When the brake disc reaches critical temperatures, the radiation heat transfer to the wheel must be controlled as well to prevent tire damage. The heat radiated to the tire can cause damage at tire temperatures as low as 200 °F (93 °C) [15]. Therefore, the directed airflow from the

moving vehicle has to dissipate a significant amount of heat by the means of convection. The thermoplastic composite wheels are sensitive to the elevated temperatures as well and a proper thermal design has to be performed. After a literature search no documented research on the impact of the radiation heat transfer to the thermoplastic composite wheels has been found.

The latest development of Computational Fluid Dynamics (CFD) increasingly contributes to the experimental work on new vehicles and their components. Reports from the experimental aerodynamic testing are often accompanied by the data from the CFD analysis. It represents a less expensive alternative with faster results, which makes it an attractive tool. Figure 2.2 shows a schematic representation of how the CFD evaluates the airflow around the vehicle's components of interest. The CFD analysis, however, will not replace the wind tunnel experiments in the foreseeable future. The large-scale wind tunnel facilities are still being built, as it is the most reliable source of the aerodynamic analysis of the vehicle we have now [17].

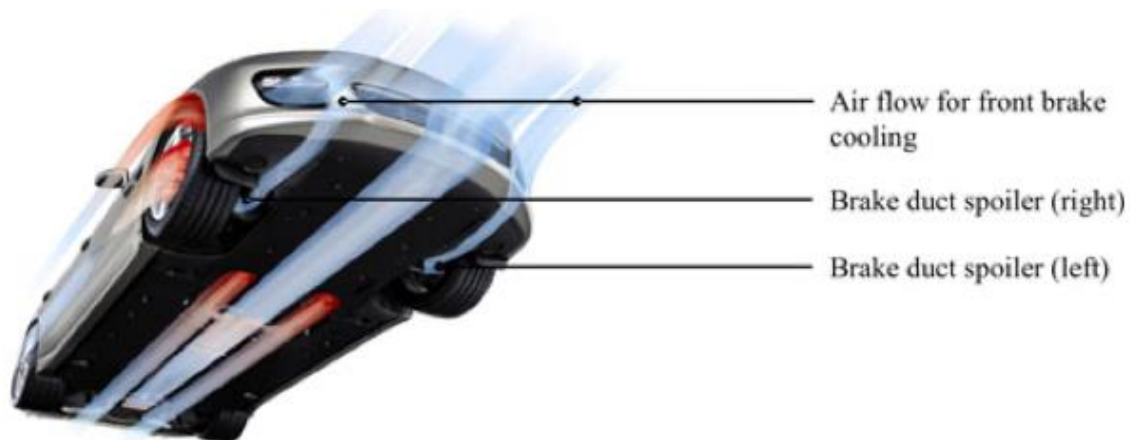


**Figure 2.2:** Schematic Representation of the CFD Airflow Cooling for the Brakes and the Engine [18]

The most common brake testing is usually conducted on a test track or on a brake dynamometer. These tests, however, are performed at the final stages of the vehicle development and there are some limitations on what data can be collected. It is also challenging to keep the variables under control. The temperature measurements on the brakes are performed with infrared thermometers or with thermocouples placed inside the rotor, while the thermocouple signal is transmitted wirelessly. Figure 2.3 illustrates collected data with an infrared camera during a brake test. It is not easy to know the emissivity value with complete confidence, as this value is not constant and depends on the temperature and the surface finish of the observed object.

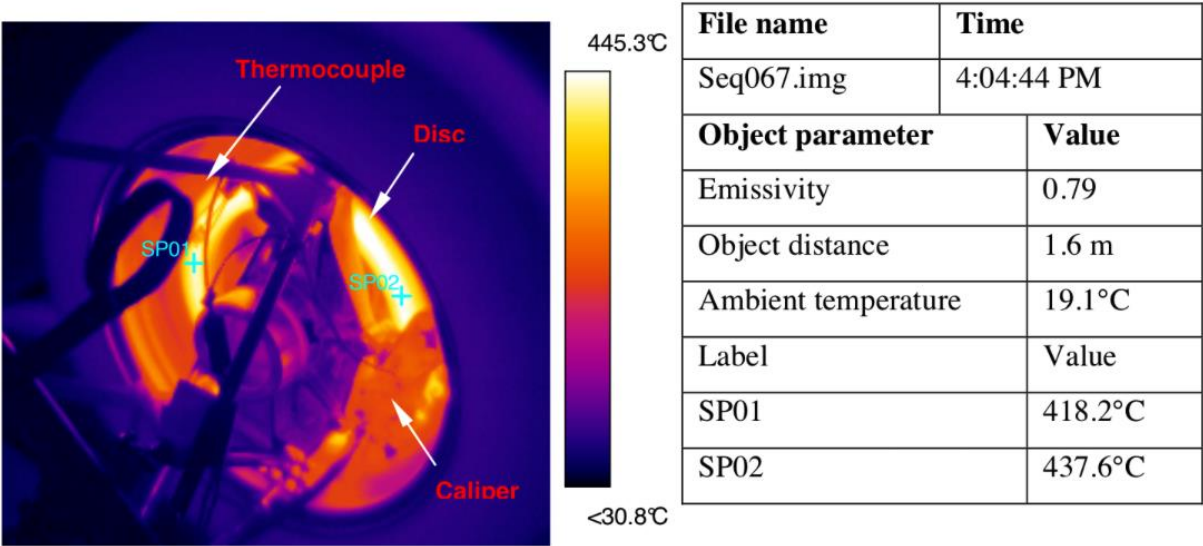


**Figure 2.3:** Temperature Measurement on the Brake Disc with an Infrared Camera [11]

The temperature measurement of the disc during a fade testing provides an insight on how the disc temperature responds to the periodic braking and cooling cycles. Figure 2.4 depicts these measurements performed on a cast iron disc during a fade test. It shows that the

repeated braking increases the peak temperature of the disc at each application of the brakes, so long as the disc does not have enough time to cool down. At extreme braking conditions the thermal failure of the brakes may occur.

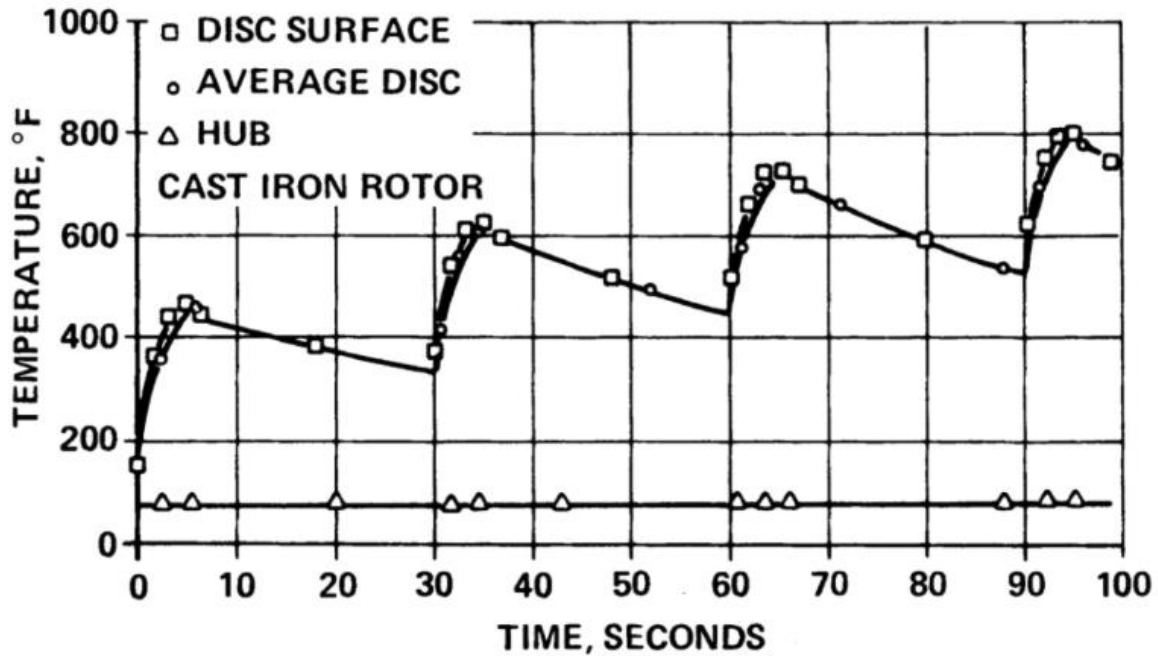


**Figure 2.4:** Brake Temperature versus Time for Multiple Brake Applications [19]

The mass of the disc determines its thermal storage capability. The smaller the brake disc the quicker it will get hot during braking and faster it will cool. For the larger disc these effects are converse. The presence of the vents in the disc will have a favorable effect on the cooling of the disc. These thermal phenomena are illustrated in Figure 2.5, where experimental temperature data collected by Stephens (2006) [11] are plotted for a continuous braking under application of a constant brake torque. The experiment was conducted for three discs with variable design features. The first disc is 287 mm in diameter without vents,

the second disc is 303 mm in diameter with vents, and the third disc is 303 mm in diameter without vents.

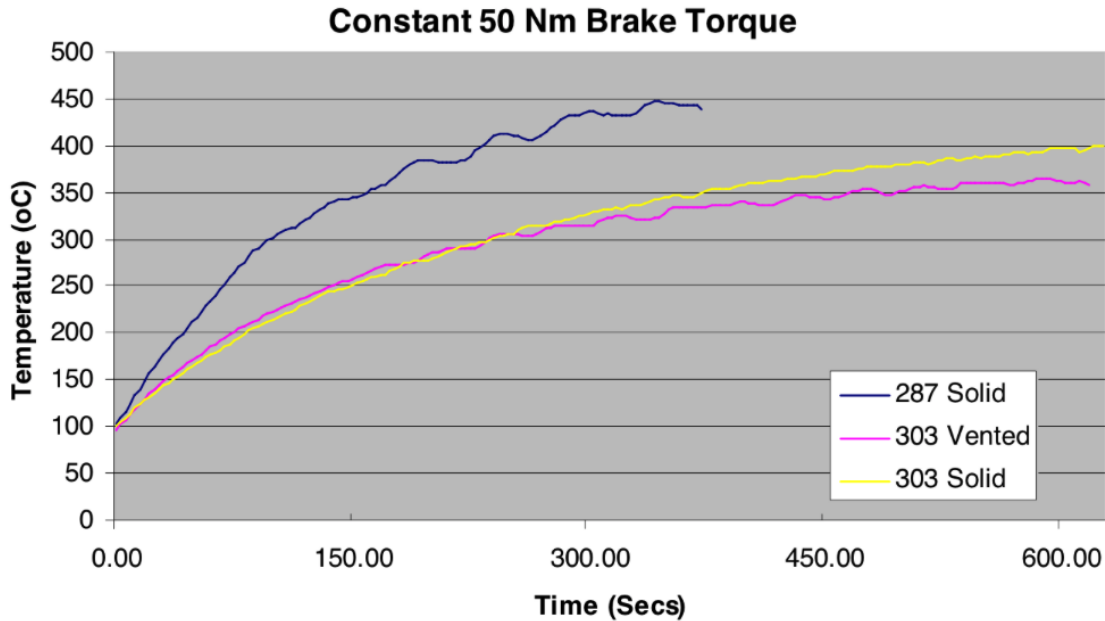


**Figure 2.5:** Temperatures on Three Different Brake Disc Styles during Braking [11]

## 2.4 Numerical Modeling

In the last fifty years, extensive numerical research has been conducted on the brake disc cooling and wheel aerodynamics. The first numerical models consisted of slightly more than one hundred grid nodes. A significant increase in the number of nodes has been possible only with the further development of the computer processors. That also made it possible to solve the conservation equations with fewer simplifying assumptions and, consequently, greater confidence in the calculated results. However, even today, the numerical modelling

provides the best results when they are performed along with experiment, which, generally, helps to utilize the wind tunnel testing more efficiently [20]. A considerable amount of error of up to 30% is normal when performing numerical analysis on a complex geometry, especially when the engineering disciplines are coupled for the analysis. Still today many simplifications and assumptions on a numerical model need to be taken in order to be able to complete a study within a meaningful time frame using reasonable resources. Even though such a high error may be present, the strongest quality of the numerical methods is when the results for different design choices are compared with each other. That provides a valuable insight on the system responses in the sensitivity study.

Belhocine and Bouchetara [21] conducted a series of transient thermo-fluid simulations for two different designs of brake discs and compared their thermal and mechanical behavior during braking. The first design is a solid disc, while the second brake disc has cooling vents. The outer dimensions of both discs are the same, but their mass varies as the venting system eliminates some material making a whole disc lighter. Figure 2.6 illustrates these discs.

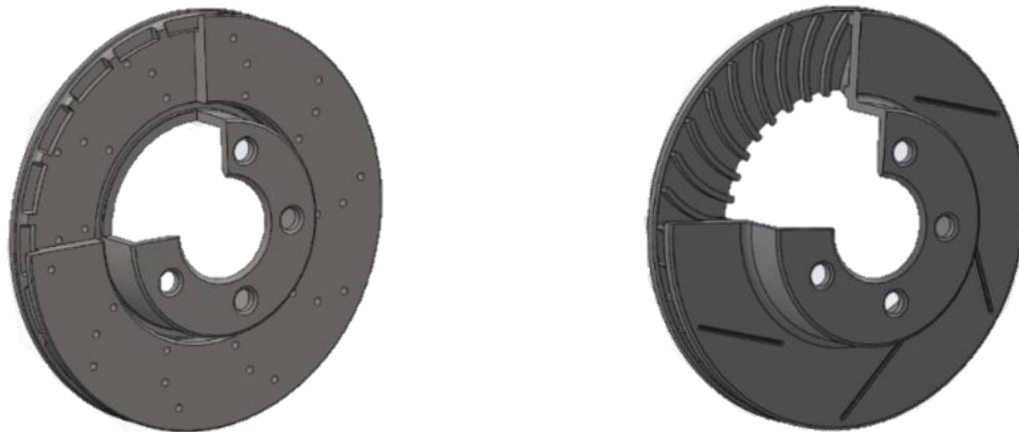


**Figure 2.6:** Three Brake Discs (a) Solid (b) with Vents (Read Left to Right) [22]

They found that the brake disc with vents has a lower overall temperature than the solid disc. That goes in line with the expectations that a larger cooling surface area of a vented disc would transfer more heat to the environment. The graph depicting the temperature comparison for the two discs is shown in Figure 2.7. They also found that the braking mode plays a significant role in the disc temperature profile. Fourteen braking cycles have been simulated for two braking modes. The first mode has a sawtooth-braking style, while the second mode has an idle between each braking cycle. For the case where the braking phase did not have an idle, the temperature of the disc would rise faster. The rate of the temperature increase would depend on the duration of the idle intervals.

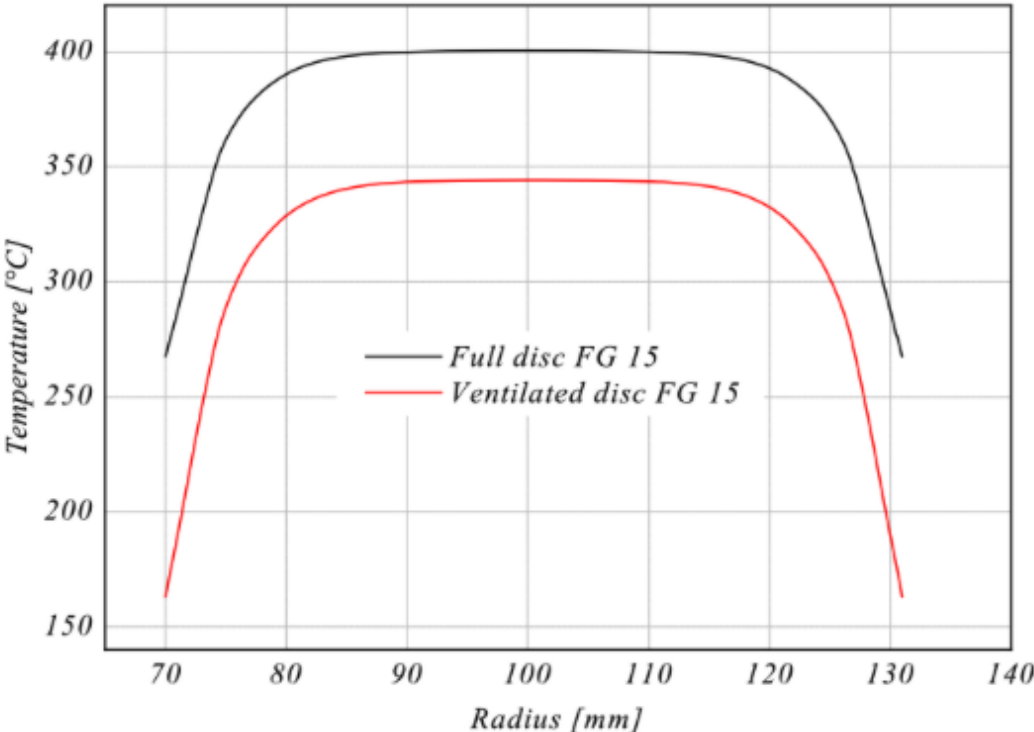


**Figure 2.7:** Temperature Variation through Radius on Both Designs

In addition, the study illustrates in Figure 2.8, how the heat transfer coefficients on different surfaces of the three discs change over time as the brake discs slow down to a complete stop. It can be seen that the heat transfer coefficient decreases drastically as the air motion abates, and the natural convection would have to take the place of the forced convection.

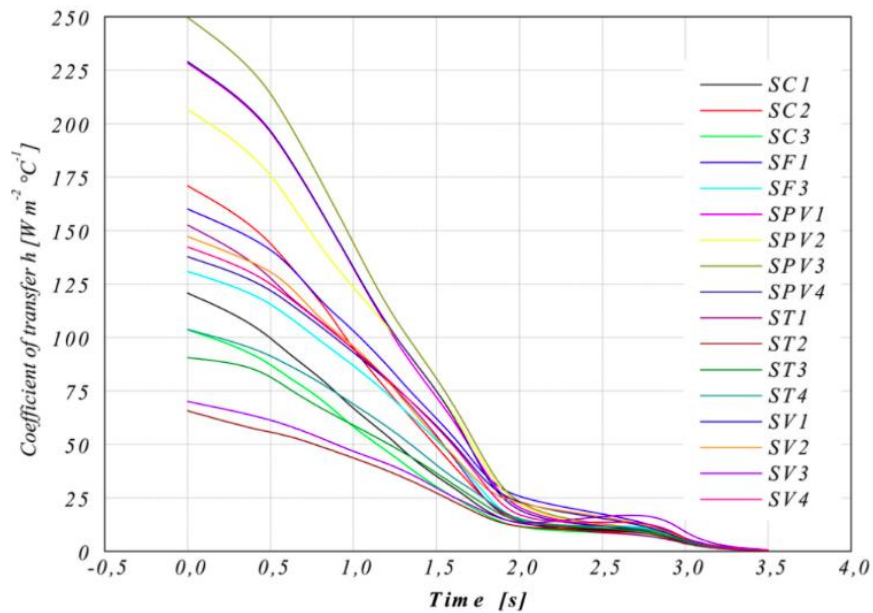


**Figure 2.8:** Variation of Heat Transfer Coefficient of Various Surfaces for three Different Brake Discs

Hunt et al [23] developed steady-state numerical simulations of air stream and heat transfer on the front disc and the caliper of the sports car GT3. This particular car is equipped with a duct system that guides the incoming airstream from the front of the car to the brake disc and the caliper shown in Figure 2.9. The objective of these simulations was to optimize the duct air flow, in order to increase the heat transfer coefficient on the caliper. The temperature of the caliper needs to be controlled as increase in its temperature heats up the brake oil inside it.

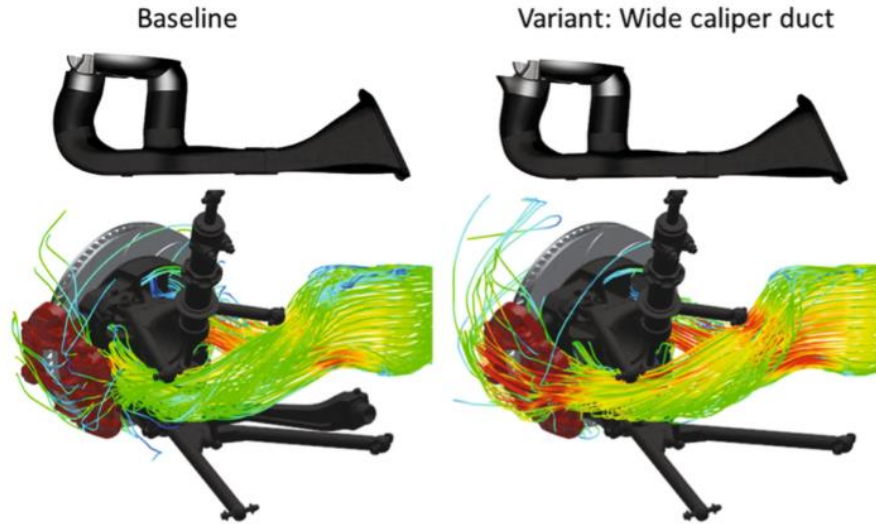


**Figure 2.9:** Air Velocity Streamlines for Two Different Duct Designs

This practical application of the numerical simulation successfully optimized the airflow in the duct in order to reduce the caliper temperature. Figure 2.10 depicts how the heat transfer coefficient varies for each component of the braking system. Even though a significant increase of the caliper cooling was achieved, the other surfaces experienced a decrease in the cooling. The optimization of the caliper cooling compromised to a certain degree the cooling of the brake disc, but the proper temperature of the braking oil was an objective of this study.

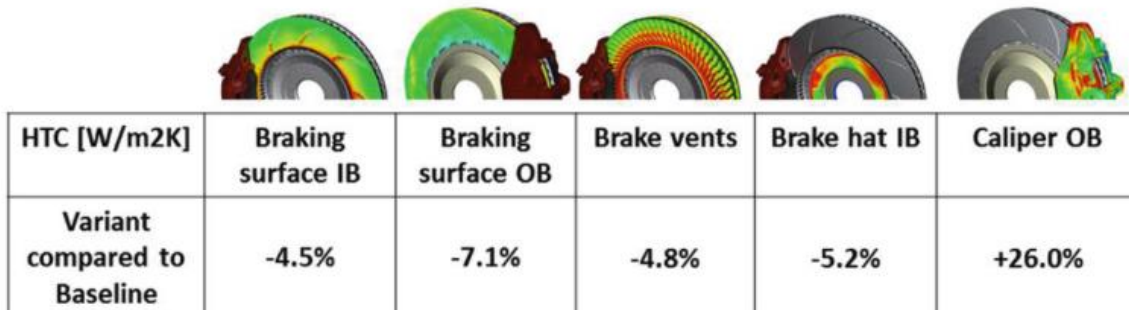


**Figure 2.10:** Surface HTC per Part. The Values are Compared to the Baseline HTC

Dekker and Krishnan [24] performed an aerodynamic analysis of the air flow in the brake disc vents and around a disc-caliper system. Figure 2.11 shows the visualization of the flow around their model. Different venting designs such as width and an angle as well as the test conditions have been evaluated in this study. One of the objectives of the study was to evaluate how different venting modifications impact the heat transfer on the brake disc when radiation and convection heat transfer mechanisms are coupled.

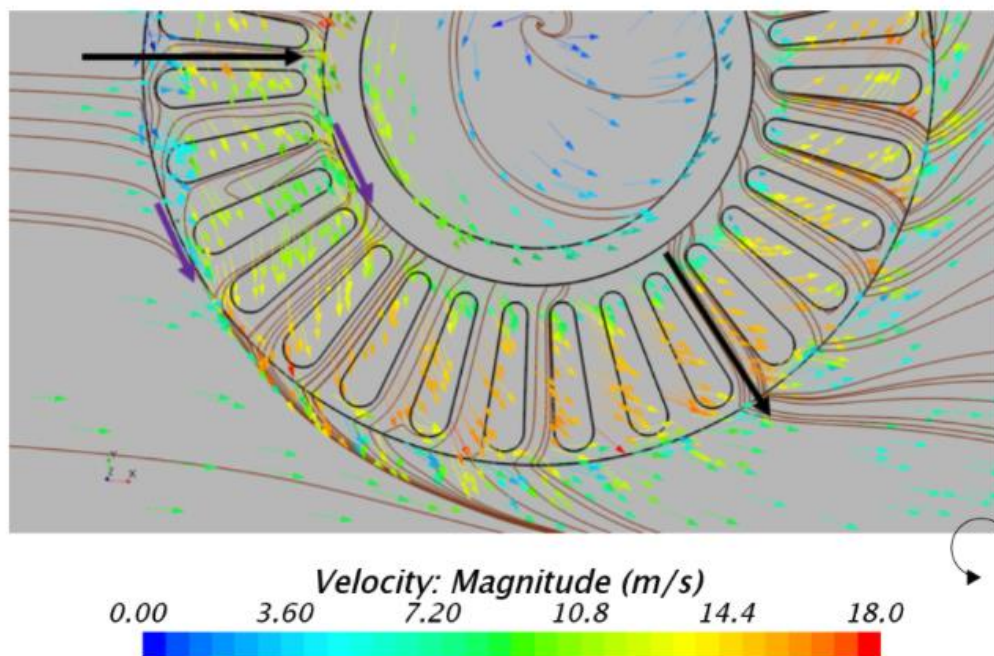


**Figure 2.11:** Velocity Vectors with Magnitude and Streamlines through the Vents

They found that the radiation heat transfer is significant at higher temperatures of the brake disc and it is recommended to consider it in the analysis at the temperatures above 300 °C. Figure 2.12 shows how a total heat transfer rate due the convection would increase, if radiation heat transfer was added to the numerical model. Different areas of the brake discs are evaluated separately, where the outer surfaces of the brake discs radiated more heat to the environment than the surfaces in the vents. That is explained with the lower temperature

gradient in the surface-to-surface radiation model in vents than in the outer surfaces that radiate into the environment. Additionally, the study monitored the total computation time when radiation was added to the model. On average, the 90% increase in the computational time has been observed.

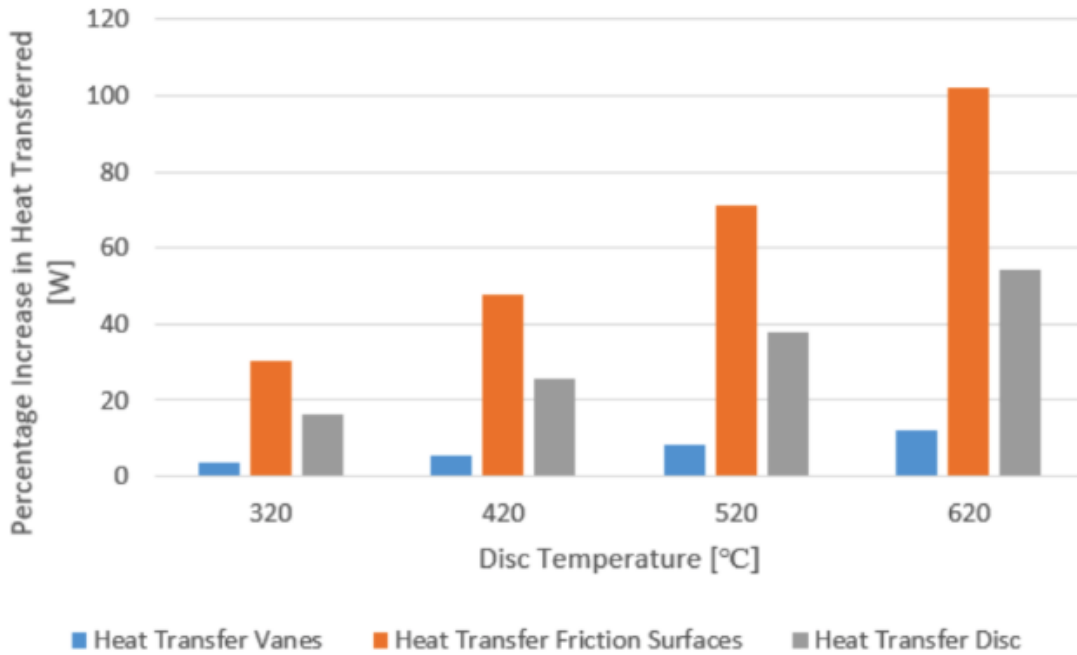


**Figure 2.12:** Heat Transfer Increase due to Radiation on Various Brake Disc Surfaces at Different Temperatures

Noyes and Vickers [25] developed a thermal model of a brake disc for estimation of the friction surface temperature and the overall heat dissipation on the disc. They concluded that after 10 braking cycles from 60 mph, 60% of the energy dissipated by convection, 34% stored in the solids, and the remainder dissipated by radiation and conduction. The model, however, consisted of a stand-alone brake disc.

## 2.5 Closing Remarks

The literature survey revealed that the heat transfer and aerodynamic phenomena on the brake system qualitatively are well understood. That has been possible with utilization of the wind tunnel testing accompanied by the numerical simulation and mathematical models. The strength of the numerical analysis lies in the ability to find an optimum solution for the specific number of the requirements or constraints. Even though it is common to have a large deviation between the measured and the calculated results, it is still possible to draw meaningful conclusions on how to make a physical system more efficient and safer.

There have not been found any literature addressing the radiation heat transfer between the brake system and the wheel. It has been determined that the radiation is most powerful at the higher temperatures which may cause tire damage, as the wheel starts storing the radiated heat from the brakes. Also, no information has been found on the thermal exchange between the thermo-plastic composite wheels and the brake system. The goal of this study is to understand the heat transfer from the brake system to the wheel at critical braking conditions and determine if the structural integrity of the thermo-plastic composite wheel might get compromised by this heat transfer process.

## CHAPTER 3

### SIMULATED SYSTEM

#### 3.1 Computational Model

The computation model in this study consists of three-dimensional components of the wheel-brake system. As the radiation and, potentially, convection heat transfer phenomena between the wheel and the brake system are the objective of the study, the system is simplified to a certain degree, in order to eliminate unnecessary computational efforts on secondary components. The components shown in Figure 3.1 are the brake disc, caliper, wheel, tire, and air in the tire (not shown). Also, the wheel is modelled as rolling on a road.

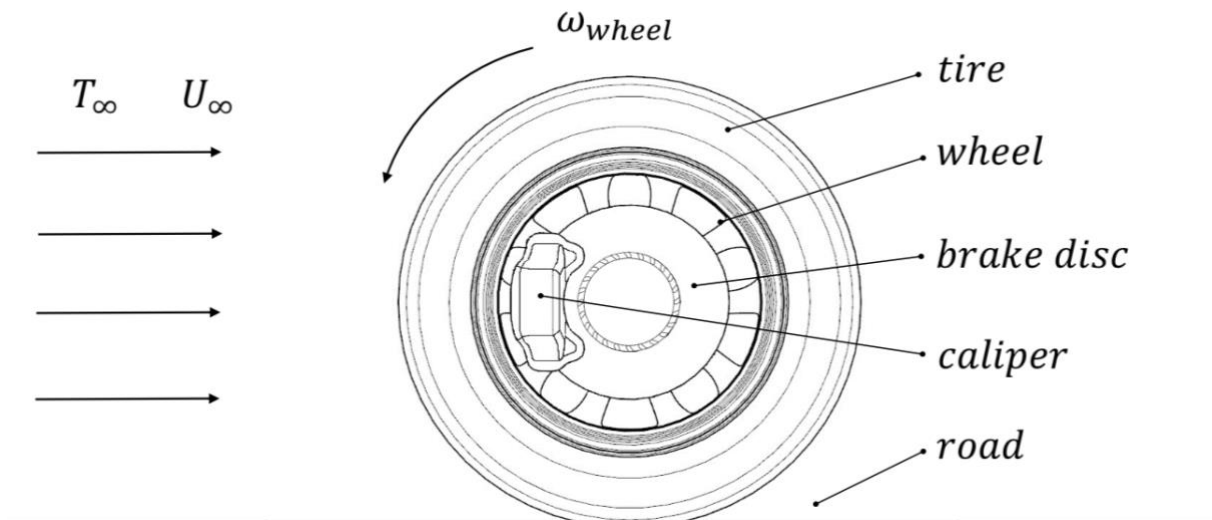


**Figure 3.1:** Schematic Illustration of the Computational Model

The three-dimensional model of the first simulation model is shown in Figure 3.2. The brake disc is modeled without a venting system. The model of the wheel and the tire remain the same throughout all simulations investigated in this study. The goal for the simulation of this model is to demonstrate the impact of pure radiation from the disc toward the inner surface of the rim without any convection heat transfer effects that a venting system may have on the rim. A more descriptive simulation setup will be discussed in the following chapter, along with the initial and boundary conditions placed on the model. In addition, the models are simulated for different velocities of the moving vehicle.

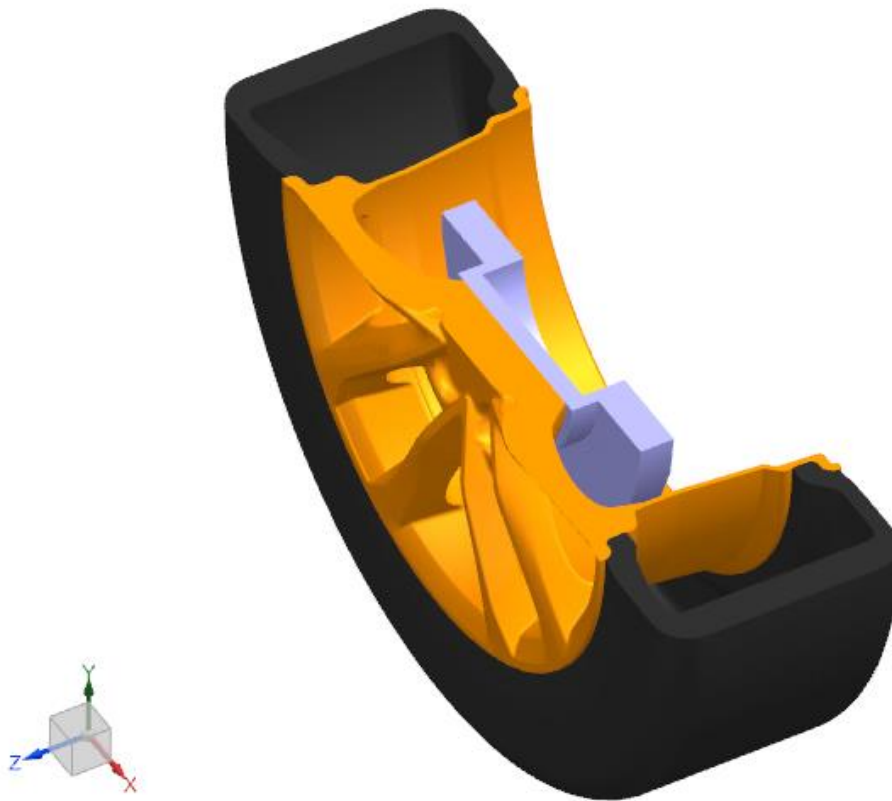


**Figure 3.2:** Section View of Wheel with Tire and Solid Brake Disc

The second simulation of the wheel-brake system model takes into consideration the venting system installed on the brake disc. Figure 3.3 depicts the brake disc with a spiral venting system; the only difference from the first model. The vents are oriented in such a way, so that the air gets sucked in with the vector toward the rim. Hypothetically, that would direct the heating air stream toward the rim and eventually increase its temperature to a certain degree. In this simulation, the convective heat transfer effects caused by the venting system will be investigated for any thermal impact on the rim. To isolate this heat transfer effect from the radiation, the high temperature surface is modeled only on the internal walls of the vents, while radiation heat transfer from the outer surfaces of the disc is deactivated. That will be discussed more in depth in the next chapter.

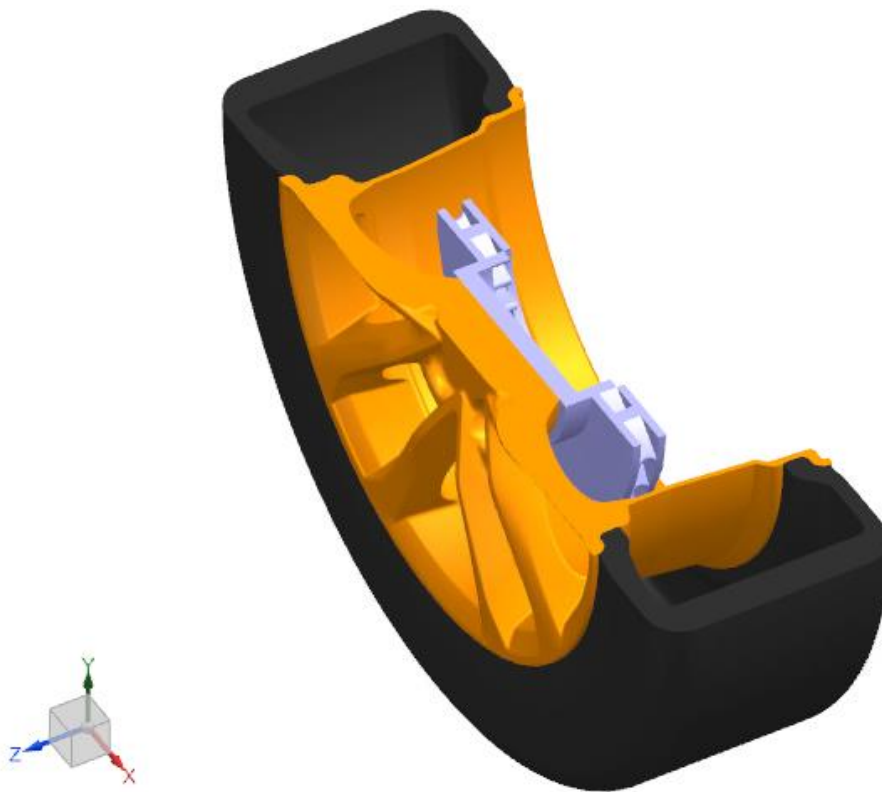


**Figure 3.3:** Section View of Wheel with Tire and Brake Disc with Vents

### 3.2 Meshing Scheme and Grid Convergence

The CFD simulation was performed with ANSYS Fluent 2020 R1 version. Figure 3.4 illustrates the simulation model within the software. The wheel-brake system is placed into a large domain, which eliminates any airflow disturbances caused by the wheel on the far points from it. That improves the convergence of the simulation and helps to avoid erroneous simulation runs by the software.

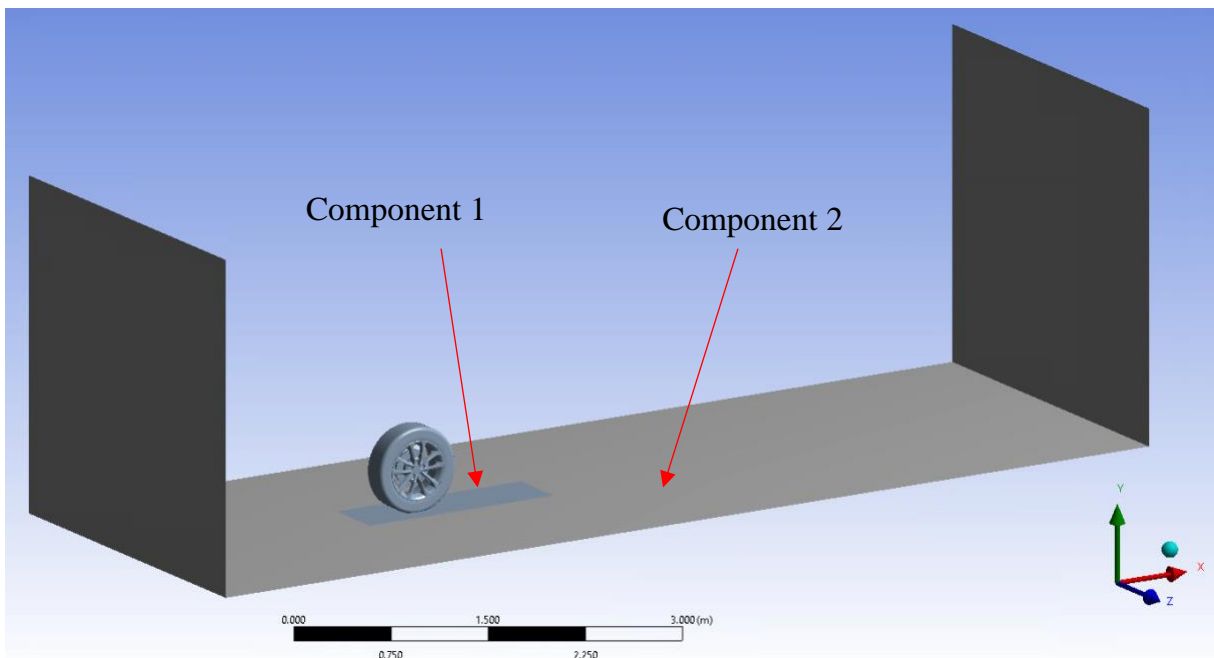


**Figure 3.4:** Wheel-Brake System in Simulation Domain

The model consists of two components, as shown above, that are connected to each other through a contact region between them. That allows meshing the wheel geometry, for the reduction of the calculation time, with a finer mesh. The significantly larger component number two can be modeled with a coarser mesh. The component one is meshed with the

node dimension equal 6 mm. The component two is modeled with the element size of 200 mm. The total number of the nodes in the model is around 1.3 million. Figure 3.5 shows the mesh constructed on the wheel-brake system.

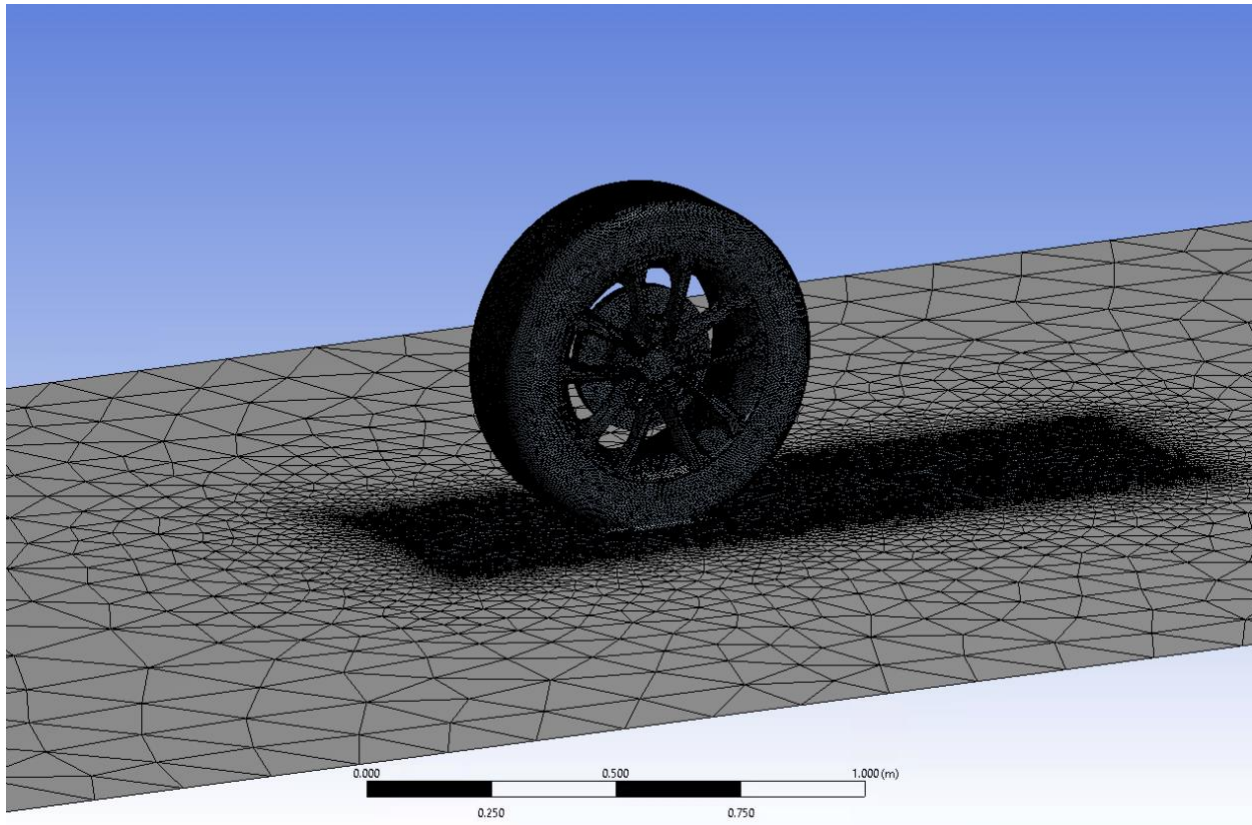


**Figure 3.5:** Illustration of Refined Mesh around the Wheel

The inflation on the surfaces of the wheel-brake geometry contains 14 grid layers, while the surfaces of the geometry are modeled with the no-slip condition. The walls of the components are modeled as having slip and no inflation layers. Figure 3.6 shows the cross-sectional view of the wheel and the brake disc constructed with the tetrahedral mesh. The 14 grid layers are depicted as thin finite volume elements if compared to the elements next to them. The thickness of these inflation layers has been chosen the way so that the flow

boundary layer is captured. The flow boundary layer modeling will be discussed in the next chapter.

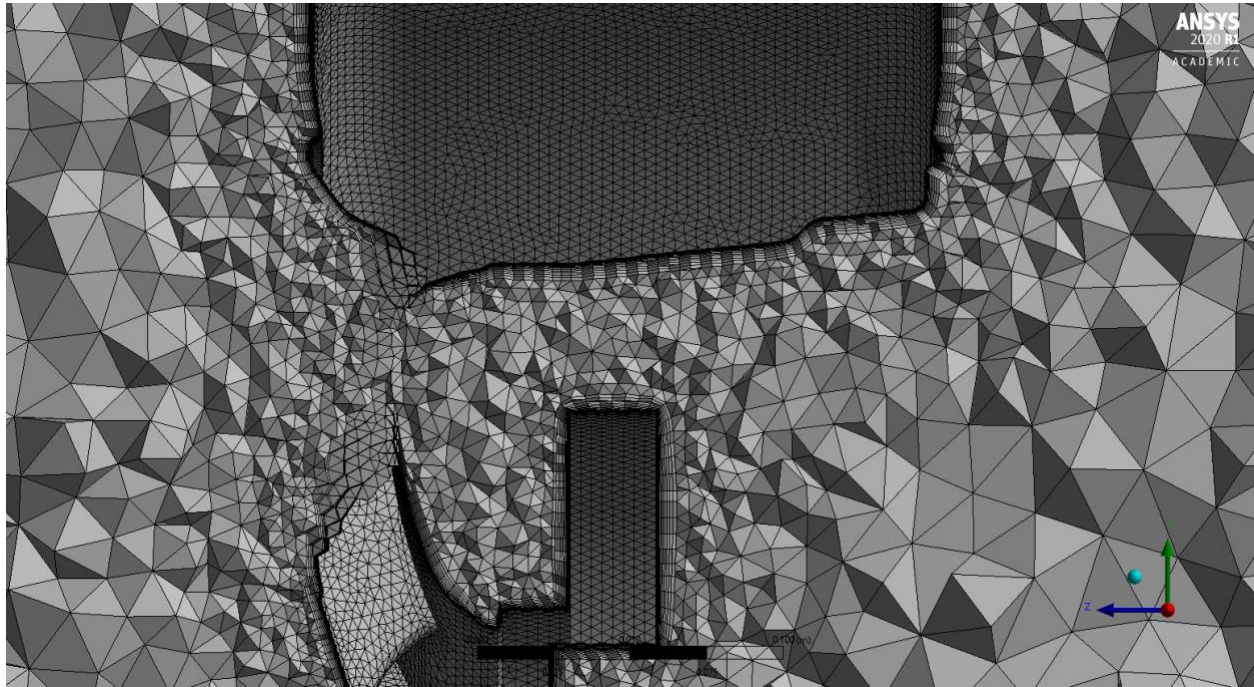


**Figure 3.6:** Inflated Mesh next to Solid Surfaces for Capturing Flow Boundary Layer

The grid convergence tests are performed on the model to ensure that the simulation results are independent of the mesh. These results are discussed in the following chapters.

## CHAPTER 4

### THEORY

#### 4.1 Flow Regime

In this study, the aerodynamic and heat transfer phenomena on the inner side of the wheel and around the brake system are simulated with Reynolds Averaged Navier-Stokes Simulation (RANS) turbulence models, which are discussed in detail and compared with similar turbulence models later in the chapter. The Reynolds number is a dimensionless quantity that is defined as the ratio of inertia forces to the viscous forces in the fluid (4.1),

$$Re_{L_c} = \frac{\rho_f U_\infty L_c}{\mu_f} \quad (4.1)$$

where  $L_c$  is a characteristic length of the object,  $\rho_f$  is the fluid density,  $U_\infty$  is the upstream velocity, and  $\mu_f$  is the fluid dynamic viscosity.

The flow regime around the geometry of the wheel, which in its nature is a blunt body, is expected to experience the boundary layer separation. This expectation is based on the experimental observations made on the formation of the boundary layer and the region of separation by the air flow across a cylinder, as there are some geometric similarities. Giebt [26] in his experimental work observed that even at lower Reynolds numbers  $> 5$ , the

boundary layer on a cylinder starts to experience flow separation creating a low-pressure region, which also is a source for the pressure drag. The region of separation expands with the increasing Reynolds number, namely the separation point happens sooner along the wall. When the separation happens, the boundary-layer arguments and equations downstream are no longer valid, as the boundary-layer and Reynolds number can be predicted only up to the point of separation. The geometries that involve flow separation are difficult to resolve analytically, and it is mostly done with empirical and/or numerical models [27].

In this work the flow around the geometry is assumed to be fully turbulent and the numerical simulation is set up to resolve the region of separation with RANS turbulence models available in ANSYS Fluent. However, the RANS turbulence models solve for the eddies with time-averaged velocity contours. Figure 4.1 discusses the dependency of the energy spectrum function  $E(k)$  for velocity fluctuations in terms of the wave number  $k$ .

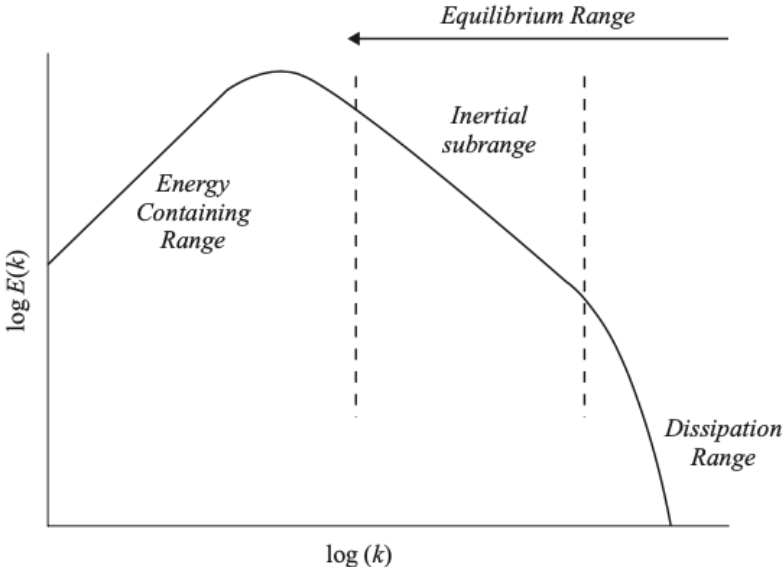


**Figure 4.1:** Qualitative Presentation of the Energy Spectrum in Isotropic Turbulence [28]

The wave number is related to frequency in the form  $k = 2\pi f/U$ . The larger the eddies the more energy they contain. The area under the curve represents a turbulent kinetic energy. The RANS models use this approach for calculation of the turbulent kinetic energy. The mesh, in practical applications, does not resolve all the eddies of the turbulent flow and only resolves a fraction of the turbulent kinetic energy present in the flow field. As a rule of thumb, a “good” Large Eddy Simulation (LES), for example, resolves at least 80% of the turbulent kinetic energy. The higher percentage of the eddies’ resolution is possible with a finer mesh, which, in turn, increases the computational cost. In the dissipation range the eddies are small enough to show viscous behavior. They are affected only by their size, fluid density, and the turbulence dissipation rate,  $\varepsilon$  [28]. The Kolmogorov microscale can be expressed with (4.2), where eddies with  $10 l_D$  have laminar flow characteristics.

$$l_D = \left( \frac{\nu^3}{\varepsilon} \right)^{1/4} \quad (4.2)$$

The macroscale of the turbulence of the largest vortices that occur in the flow field is too large to be affected by the viscosity and they are defined only by inertia.

## 4.2 Turbulence Models

There is a broad variety of numerical turbulence models available for the modeling of the turbulent flow for a wide range of the geometrical complexity. These models treat the turbulence as a transported property as opposed to the classical models, where the

equilibrium is assumed among the generation, dissipation, and transported turbulent energy for the entire eddy size spectrum [28]. The accuracy of the turbulence modelling and near the wall flow profile strongly depend on the quality of the mesh; with a finer mesh requiring more computational resources. Figure 4.2 summarizes two main computational approaches - space filtering and time-averaging - that make turbulence computationally tractable and are classified among the methodologies by which the Navier-Stokes equations are solved.

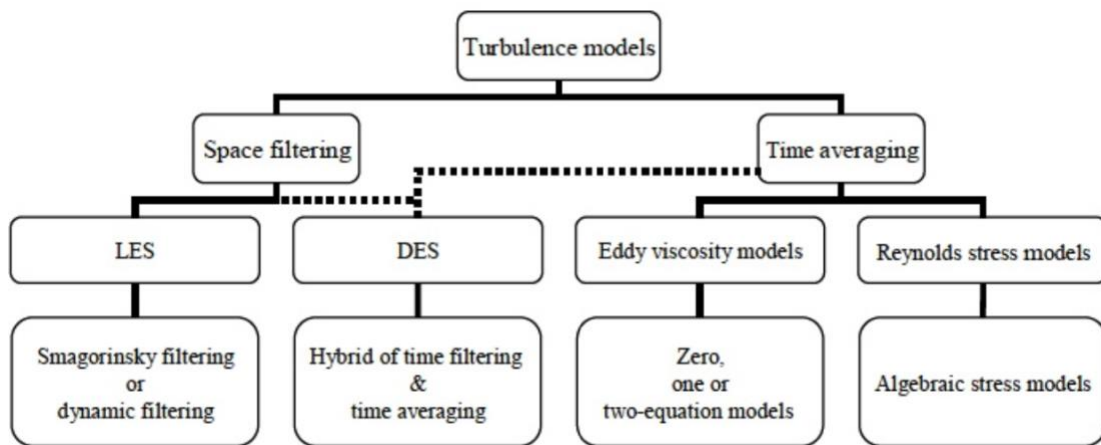


**Figure 4.2:** Classification of Turbulence Models [29]

The Large Eddy Simulation (LES) solves the spatially averaged Navier-Stokes equations, where the large eddies are directly resolved, but the eddies smaller than the mesh are modeled. It is less expensive than Direct Numerical Simulation (DNS), but the required computational resources are still very significant to apply it in practical applications. The Direct Numerical Simulation (DNS) solves the full unsteady Navier-Stokes equations and resolves the whole spectrum of scales that does not require a space filtering or time averaging and eliminates the need for the turbulence modeling. However, the computational cost can be too prohibitive. Reynolds Averaged Navier-Stokes Simulation (RANS) solves

time-averaged Navier-Stokes equations, while all turbulent length scales are modeled. There are various different RANS models available and they are most widely used for industrial applications. Figure 4.3 illustrates the way the turbulent flow is modeled and visualized with the three different turbulent approaches.

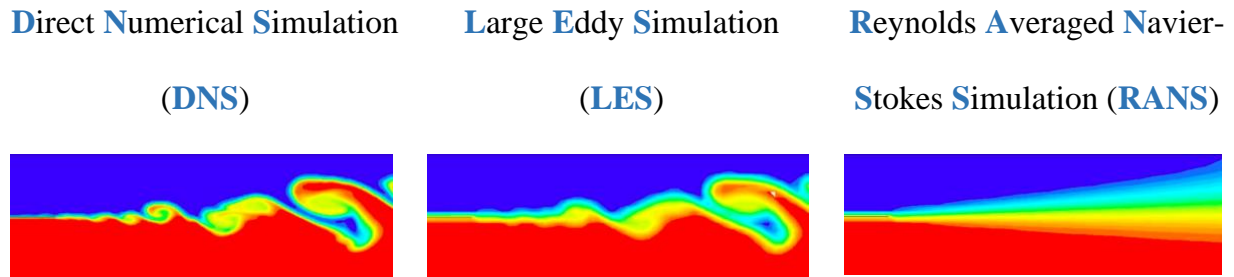


**Figure 4.3:** Turbulence Resolution by Three Leading Computational Approaches [30]

As it was already mentioned, the meaningful solution of the flow field using RANS is obtained by modeling the largest and smallest eddies in the flow field. The semiempirical analysis methods of the RANS are very popular practical methods. The observation is that even for very random flow the turbulent fluctuations can successfully be resolved with respect to their statistical patterns, where Navier-Stokes equations are averaged [28]. The RANS models contain empirical correlations that cannot be derived from the fundamental principles. As a result, some calibration to the observed empirical solutions is required, while a certain amount of “guessing” is always present in the model. The RANS models can be subdivided in various methods with their strengths and weaknesses for specific fluid mechanics problems. Figure 4.3 depicts selected RANS turbulent models available in ANSYS Fluent. The turbulent models are organized in a way that the least computationally demanding model is placed on top of the list with the increasing demand downstream.

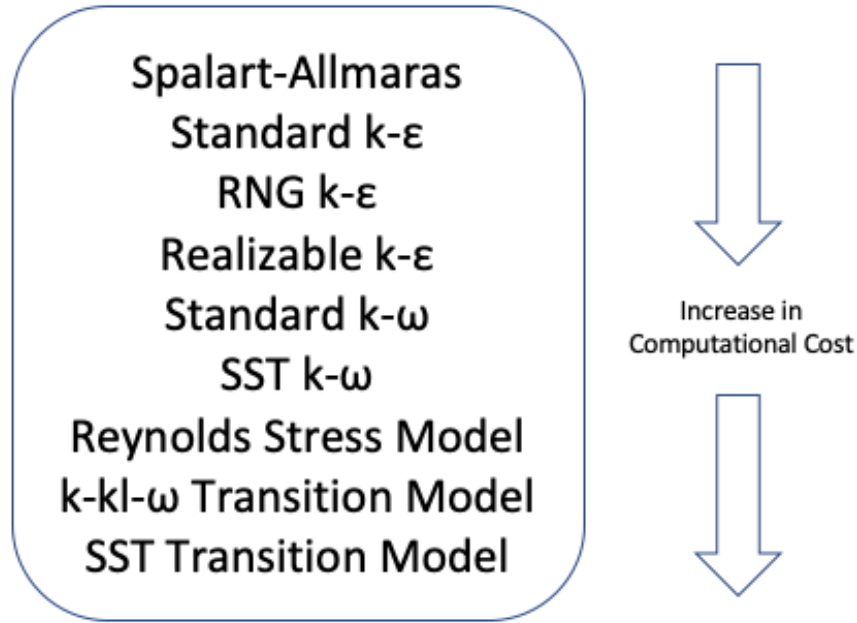


**Figure 4.4:** Popular RANS Turbulence Models

Below are summarized the methodologies by which some of the turbulent models are solved, while comparing their limitations and strengths. Some of these models can be characterized as a one-equation and two-equation models. For example, Spalart-Allmaras (1992, 1994) model is a one-equation model that solves only one transport equation for the turbulent viscosity,  $\mu_{tu}$ . This model has proved to be successful in aerospace applications showing good correlation with the external boundary-layer calculations involving well-bounded flows. It also requires the least amount of computational resources. However, this model is unsuitable for complex geometries, as it is difficult to define the length scale. It also is rarely used for heat transfer problems due to lack of accuracy.

The  $k - \epsilon$  turbulent model and  $k - \omega$  turbulent model are the two-equation models and solve two transport equations utilizing two independent scales for calculating the turbulent viscosity. These models are the most popular in industrial applications. The  $k - \epsilon$

two-equation models include two additional transport equations to represent the turbulent kinetic energy,  $k$  and the turbulent dissipation rate,  $\varepsilon$ . The model is suitable for a wide range of applications, but it has several limitations. It performs poorly for flows with larger pressure gradient, strong separation, high swirling component and large streamline curvature.

The Realizable  $k - \varepsilon$  model (Shih 1995 [34]) provides superior performance for flows involving rotation, boundary layers under strong adverse pressure gradients, separation, and recirculation. This model derives the dissipation rate,  $\varepsilon$ , equation from the mean-square vorticity fluctuation, which is fundamentally different from the Standard  $k - \varepsilon$  model.

The  $k - \omega$  model, which is also derived based on the  $k - \varepsilon$  model, calculates the specific dissipation rate,  $\omega$  instead of  $\varepsilon$ , (Wilcox 1998 [35]). This model shows much better performance than  $k - \varepsilon$  for boundary layer flows. It is more accurate for separation, transition, low-Re effects, and boundary layer flows with pressure gradient. However, separation is typically predicted to be excessive and early [31].

The Shear Stress Transport (SST)  $k - \omega$  model uses both  $k - \varepsilon$  and  $k - \omega$  models combining their advantages. The  $k - \omega$  model performs much better for boundary layer flows, so it solves the region near the wall. As the  $k - \omega$  is very sensitive to the freestream value of  $\omega$ , while  $k - \varepsilon$  is not, the  $k - \varepsilon$  model solves the region far from the wall.

The Reynolds Stress Model (RSM) closes the Reynolds-Averaged Navier-Stokes equations by solving model transport equations for the Reynolds stresses, together with an equation for the dissipation rate. As a result, seven additional transport equations are required for three-dimensional problems. It is more computationally expensive and is difficult to

converge due to close coupling of equations [31]. As the RSM estimates the effects of streamline curvature, swirl, rotation, and rapid changes in strain rate more rigorously, it is more accurate in predictions of complex flows with strong swirls such as a cyclone.

### 4.3 Governing Equations

In the Reynolds-Averaged Navier-Stokes (RANS) Model, each fluid property is decomposed to mean and fluctuating components [32]. Equation 4.3 shows the general rule of the Reynolds decomposition for any fluid characteristic  $\phi$  such as velocity, pressure, temperature, mass concentration, and density:

$$\phi = \phi' + \bar{\phi} \quad (4.3)$$

The fluid properties in this form are then inserted in the local and instantaneous mass conservation Equation 4.4, the momentum conservation Equations 4.5 (only one coordinate shown), and the thermal energy conservation Equation 4.7. All these equations are written in the Cartesian coordinate system and formulated using Einstein's summation rule.

$$\frac{\partial u_j}{\partial x_j} = 0 \quad (4.4)$$

Momentum in  $i$ -coordinate,

$$\frac{\partial}{\partial t}(\rho u_i) + \frac{\partial}{\partial x_j}(\rho u_i u_j) = -\frac{\partial P}{\partial x_i} + \frac{\partial \tau_{ij}}{\partial x_j} + \rho g_i \quad (4.5)$$

where

$$\tau_{ij} = \mu \left( \frac{\partial u_i}{\partial x_j} + \frac{\partial u_j}{\partial x_i} \right) \quad (4.6)$$

Thermal energy equation,

$$\frac{\partial}{\partial t}(\rho C_p T) + \frac{\partial}{\partial x_j}(\rho C_p u_j T) = -\frac{\partial q_j''}{\partial x_j} + \mu \Phi \quad (4.7)$$

where

$$q_j'' = -k \frac{\partial T}{\partial x_j} \quad (4.8)$$

$$\mu \Phi = \frac{\mu}{2} \left( \frac{\partial u_i}{\partial x_j} + \frac{\partial u_j}{\partial x_i} \right)^2 \quad (4.9)$$

After substituting all fluctuating properties (Eq. 4.3) in all the terms in Equations 4.4, 4.5, and 4.7, and performing Reynolds averaging on all the terms in these equations, we get the Reynolds-averaged conservation equations.

$$\frac{\partial \bar{u}_j}{\partial x_j} = 0 \quad (4.10)$$

$$\frac{\partial}{\partial t}(\rho \bar{u}_i) + \frac{\partial}{\partial x_j}(\rho \bar{u}_i \bar{u}_j) = -\frac{\partial \bar{P}}{\partial x_i} + \frac{\partial}{\partial x_j}(\bar{\tau}_{ij} - \rho \overline{u_i' u_j'}) + \rho g_i \quad (4.11)$$

$$\frac{\partial}{\partial t}(\rho C_p \bar{T}) + \frac{\partial}{\partial x_j}(\rho C_p \bar{u}_j \bar{T}) = -\frac{\partial}{\partial x_j}(\bar{q}_j + \rho C_p \overline{u'_j T'}) + \mu \bar{\Phi} \quad (4.12)$$

where,

$$\mu \bar{\Phi} = \frac{\mu}{2} \overline{\left( \frac{\partial \bar{u}_i}{\partial x_j} + \frac{\partial u'_i}{\partial x_j} + \frac{\partial \bar{u}_j}{\partial x_i} + \frac{\partial u'_j}{\partial x_i} \right)^2} \quad (4.13)$$

These equations are complicated because of the presence of terms such as  $\overline{u'_i u'_j}$  and  $\overline{u'_i \phi'}$ , where  $\phi'$  is the fluctuation of any scalar transported property. All the flux terms have now a laminar and a turbulent component shown in Equations (4.14) and (4.15)

$$\tau_{ij} = \rho \left[ \nu \left( \frac{\partial u_i}{\partial x_j} + \frac{\partial u_j}{\partial x_i} \right) - \overline{u'_i u'_j} \right] \quad (4.14)$$

$$q''_j = \rho C_p \left( -\alpha \frac{\partial T}{\partial x_j} + \overline{u'_j T'} \right) \quad (4.15)$$

The Reynolds stress is defined in Equation 4.16. This non-linear acceleration term cannot be solved directly, which is why it has to be modeled.

$$\tau_{ij,tu} = -\rho \overline{u'_i u'_j} \quad (4.16)$$

The turbulence models for RANS provide the terms that are required to calculate the eddy viscosity  $\mu_{tu}$ , which is then used in Boussinesq approximation to model the Reynolds stresses and solve the NS with considering the additional mixing provided by the turbulent

fluctuations. It is further assumed that turbulence is locally isotropic, which makes the eddy diffusivity,  $E$  (or equivalently  $\mu_{tu} = \rho E$ ), a scalar

$$-\rho \overline{u'_i u'_j} = \rho E \left( \frac{\partial \bar{u}_j}{\partial x_i} + \frac{\partial \bar{u}_i}{\partial x_j} \right) - \frac{2}{3} \delta_{ij} \rho k \quad (4.17)$$

The turbulent kinetic energy is defined as,

$$k = \frac{1}{2} \overline{u'_i u'_i} \quad (4.18)$$

The term  $\frac{2}{3} \delta_{ij} k$  is added to avoid unphysical prediction, such as zero turbulence kinetic energy for an incompressible fluid.

Similarly, as for molecular diffusion we can define the turbulent Prandtl number (Eq. 4.19), which allows solving Equation 4.17 by replacing the eddy diffusivity,  $E$  with “known” variables. These variables are determined empirically.

$$Pr_{tu} = \frac{E}{E_{th}} \quad (4.19)$$

After several mathematical manipulations of the turbulent terms, the mass, momentum, and thermal energy equations take the laminar form of the same equations, which now can be more easily solved.

### 4.3.1 Standard $k - \varepsilon$ Model

In the  $k - \varepsilon$  model the velocity scale ( $U_{tu}$ ) and the length scale ( $l_{tu}$ ) are treated as the transported properties. The Prandtl mixing-length model assumes that the turbulent viscosity ( $\mu_{tu}$ ) is related to these properties in a form shown in Equation 4.20.

$$\mu_{tu} = \rho l_{tu} U_{tu} \quad (4.20)$$

The Equation 4.20 can be rewritten with  $l_{tu} = (k^{3/2}/\varepsilon)$  and  $U_{tu} = \sqrt{k}$  to a following form:

$$\mu_{tu} = C_\mu \rho \frac{k^2}{\varepsilon} \quad (4.21)$$

Now that we treat the turbulent kinetic energy ( $k$ ) and the dissipation of turbulent kinetic energy ( $\varepsilon$ ) as transported properties, two additional transport equation can be derived to solve for them (Equation 4.22 and 4.23). The derivation of these equations can be found in Appendix A. The resulting transport equations are

$$\rho \frac{Dk}{Dt} = \frac{\partial}{\partial x_i} \left[ \left( \mu + \frac{\mu_{tu}}{\sigma_k} \right) \frac{\partial k}{\partial x_i} \right] + \mu_{tu} \frac{\partial \bar{u}_i}{\partial x_j} \left( \frac{\partial \bar{u}_i}{\partial x_j} + \frac{\partial \bar{u}_j}{\partial x_i} \right) - \rho \varepsilon \quad (4.22)$$

$$\rho \frac{D\varepsilon}{Dt} = \frac{\partial}{\partial x_i} \left[ \left( \mu + \frac{\mu_{tu}}{\sigma_\varepsilon} \right) \frac{\partial \varepsilon}{\partial x_i} \right] + C_{\varepsilon 1} \frac{\varepsilon}{k} \mu_{tu} \frac{\partial \bar{u}_i}{\partial x_j} \left( \frac{\partial \bar{u}_i}{\partial x_j} + \frac{\partial \bar{u}_j}{\partial x_i} \right) - C_{\varepsilon 2} \rho \frac{\varepsilon^2}{k} \quad (4.23)$$

These equations contain five constants, the values of which are shown in Equation 4.24. These constants were determined empirically, with the most widely used values determined by the Launder and Sharma (1974).

$$C_{\mu} = 0.09, C_{\varepsilon 1} = 1.44, C_{\varepsilon 2} = 1.92, \sigma_k = 1, \sigma_{\varepsilon} = 1.3 \quad (4.24)$$

The assumption in the  $k - \varepsilon$  model that there is local isotropy in the turbulent field hinders application of the  $k$  and  $\varepsilon$  transport equations all the way to the walls. These equations are invalid in the near-wall region. Also, it is assumed in the model that the Reynolds stresses are linearly related to the local mean strain rate. That leads to a relatively poor performance for the flows with strong curvature or rotation. The modifications of the standard  $k - \varepsilon$  allowed to address these issues and are discussed next.

#### 4.3.2 Standard $k - \omega$ Model

The standard  $k - \omega$  model has superior performance compared to the  $k - \varepsilon$  model in the near-wall region, as long as the mesh adjacent to walls is defined fine enough to model the flow boundary layer. The specific turbulence dissipation rate ( $\omega$ ) is defined in Equation 4.25. Both  $k$  and  $\omega$  describe the dissipation of turbulent kinetic energy, so we can solve the transport equation of either of them, while these entities can be easily converted using the relationship below, where  $\beta^*$  is a constant.

$$\omega = \frac{1}{\beta^*} \frac{\varepsilon}{k} \quad (4.25)$$

For an incompressible flow the standard transport equations for  $k$  and  $\omega$  are

$$\rho \frac{Dk}{Dt} = \frac{\partial}{\partial x_i} \left[ \left( \mu + \frac{\mu_{tu}}{\sigma_k} \right) \frac{\partial k}{\partial x_j} \right] + \tau_{ij,tu} \frac{\partial \bar{u}_i}{\partial x_j} - \rho \beta^* \omega k \quad (4.26)$$

$$\rho \frac{D\omega}{Dt} = \frac{\partial}{\partial x_i} \left[ \left( \mu + \frac{\mu_{tu}}{\sigma_\omega} \right) \frac{\partial \omega}{\partial x_j} \right] + \frac{\gamma \omega}{k} \tau_{ij,tu} \frac{\partial \bar{u}_i}{\partial x_j} - \rho \beta \omega^2 \quad (4.27)$$

where

$$\mu_{tu} = \frac{\gamma^* \rho k}{\omega} \quad (4.28)$$

$$\tau_{ij,tu} = 2\mu_{tu} \left[ S_{ij} - \frac{1}{3} \frac{\partial \bar{u}_k}{\partial x_k} \delta_{ij} \right] - \frac{2}{3} \delta_{ij} \rho k \quad (4.29)$$

The elements of the mean strain-rate tensor are

$$S_{ij} = \frac{1}{2} \left( \frac{\partial \bar{u}_i}{\partial x_j} + \frac{\partial \bar{u}_j}{\partial x_i} \right) \quad (4.30)$$

This model has six empirical coefficients  $(\gamma, \gamma^*, \beta, \beta^*, \sigma_k, \sigma_\omega)$ , with their optimized values summarized in the forthcoming equation

$$\gamma = \frac{5}{9}, \quad \gamma^* = 1, \quad \beta = \frac{3}{40}, \quad \beta^* = 0.09, \quad \sigma_k = 2, \quad \sigma_\omega = 2 \quad (4.31)$$

The  $k - \omega$  model is more accurate than the  $k - \varepsilon$  model, when there is an adverse pressure gradients and near-separation conditions. However, small changes in freestream turbulence lead to significant changes in the turbulent viscosity ( $\mu_{tu}$ ), which greatly affects the results. For example, this will affect the forces on the body and erroneously predict the flow separation inception. One solution is to blend the  $k - \omega$  with the  $k - \varepsilon$  model, which performs better in freestream conditions. The next subchapter discusses this solution.

#### 4.3.3 Shear Stress Transport (SST) $k$ - $\omega$ Model

The use of Shear Stress Transport (SST)  $k - \omega$  model developed by (Menter 1994 [36]) combines the strengths of two models, as it uses both  $k - \varepsilon$  and  $k - \omega$ . The turbulence viscosity is defined in a way that the transport of the principal turbulent shear stress is taken into account. Near the wall, the SST model uses the robust  $k - \omega$  model, while in the far field it switches to the  $k - \varepsilon$  model, which is free-stream independent. The SST  $k - \omega$  model is similar to the standard  $k - \omega$  model, but certain refinements are included. For example, the standard  $k - \omega$  and  $k - \varepsilon$  models are both multiplied by a blending function ( $F_2$ ) defined in Equation 4.32 and both models are added together.

$$F_2 = \tanh(\arg_2^2) \tag{4.32}$$

where

$$arg_2^2 = \min \left\{ \frac{2\sqrt{k}}{0.09\omega y}; \frac{500\mu}{\rho\omega y^2} \right\} \quad (4.33)$$

The other modifications include different modeling constants, additional terms added to the transport equations, and the definition of the turbulent viscosity is modified to account for the transport of the turbulent shear stress.

The widely used model constants are

$$\gamma_2 = 0.44, \beta_2 = 0.083, \beta^* = 0.09, \sigma_k = 1, \sigma_{\omega,1} = 2, \sigma_{\omega,2} = 1.17 \quad (4.34)$$

#### 4.3.4 Turbulent Heat Transfer

Thermal energy conservation equation (Eq. 4.12) and heat flux (Eq. 4.15) for turbulent flows can be solved with help of Equation 4.35. These equations are numerically solved along with the mass, momentum, and energy conservation equations and the transport equations for  $k$ ,  $\varepsilon$ , and  $\omega$ . Furthermore, for the energy equation one can write

$$\overline{\rho u_j' T'} = - \frac{\mu_{tu}}{Pr_{tu}} \frac{\partial \bar{T}}{\partial x_j} \quad (4.35)$$

By defining a turbulent Prandtl number, we can calculate the eddy diffusivity for heat transfer with Equation 4.36

$$E_{th} = \frac{E}{Pr_{tu}} = \frac{1}{Pr_{tu}} \frac{C_\mu K^2}{\varepsilon} \quad (4.36)$$

#### 4.3.5 Near-Wall Turbulence Modeling and Wall Functions

The RANS turbulence models often use wall functions to model the turbulent effects in the proximity of the wall. An alternative method is to use Low-Reynolds number versions of the aforementioned turbulence models and resolve the boundary layers by defining much finer mesh near walls. That is necessary, because the assumption of isotropic turbulence is not valid near the wall. In addition, in comparison with low-Re models and models based on switching to one-equation representation of the turbulence in the boundary layers, wall functions are the least expensive in terms of the calculation cost making them a useful tool. The viscosity starts to play a larger role near the wall and the turbulence become very complex. However, it must be mentioned that when wall functions are used, the boundary layer is resolved only partially. That leads to the loss of considerable portions of information about the unresolved layers.

The boundary layer can be considered of two layers - the inner layer and the outer layer. The inner boundary layer is strongly influenced by the viscosity and the shear stress at the wall. The outer boundary layer, in contrast, is strongly influenced by the turbulent eddies, while viscous effects are insignificant. The inner boundary layer typically consists of 10% to 20% of the entire boundary layer. The inner and outer boundary layers smoothly merge through the overlap layer. The shape of the velocity profile in the inner and the overlap layers, to the most part, are independent of the flow conditions. That makes the models of these layers universal for different types of flow scenarios.

The inner layer can be further subdivided into sub layers – viscous sublayer, buffer sublayer, and the fully turbulent (overlap) zone. Often, in the near-wall turbulence modelling, the buffer zone and viscous sublayer are assumed to merge and the normal distance from the wall  $y_u^+ = 9$  defines the intersection between the viscous sublayer and the overlap zone [28]. Below, the three sublayers for smooth surfaces are briefly discussed in terms of the dimensionless velocity ( $u^+$ ) and the dimensionless distance from the wall ( $y^+$ ).

The viscous sublayer extends within  $y^+ < y_u^+$  and its velocity profile follows Equation 4.37. The viscous effects in the viscous sublayer are dominant and the flow field is nearly laminar, while in the overlap layer the viscous and turbulent effects are important.

$$u^+ = y^+ \quad (4.37)$$

The fully turbulent (overlap) zone is in the region  $y^+ > y_u^+$  and its velocity profile follows Equation 4.38. The turbulent eddies dominate the transport processes within this layer, while the viscous effects can be neglected.

$$u^+ = \frac{1}{\kappa} \ln y^+ + B \quad (4.38)$$

The dimensionless velocity and normal distance to the wall can be determined with Equations 4.39 and 4.40.

$$y^+ = y \frac{U_\tau}{\nu} \quad (4.39)$$

$$u^+ = \frac{\bar{u}}{U_\tau} \quad (4.40)$$

The friction velocity ( $U_\tau$ ) based on the wall shear stress with the velocity zero at the wall can be determined with

$$U_\tau = \sqrt{\frac{\tau_s}{\rho}} \quad (4.41)$$

The velocity profiles for the inner boundary layer on a complex geometry may differ from the models in Equations 4.37 and 4.38. These models work the best for the boundary layer on a flat smooth plate when the ambient velocity is constant. The large positive and negative pressure gradients along the streamline, for example, alter the velocity profile in the wake zone. It has been found, however, that moderate pressure gradient can still be predicted well [28].

The  $y^+$  helps to determine the mesh height of the first cell near the no-slip wall. It is recommended to select the first cell height  $y^+ \sim 1$ . Having the viscous sub-layer resolved is a requirement for the low Reynolds turbulence models. For a complex geometry,  $y^+$  will differ at different locations. Depending on the simulation requirements, an appropriate near-wall treatment needs to be applied with a possibility of sacrificing accuracy at certain regions of the simulated model.

Similarly, the wall function for temperature profile can be derived as well. For  $y^+ < y_T^+$ , where  $y_T^+$  can be estimated from the simulation, temperature profile in the viscous sublayer and the buffer layer is determined with

$$T^+ = Pr y^+ \quad (4.42)$$

where the dimensionless temperature is defined as

$$T^+ = \frac{T_s - \bar{T}}{\frac{q_s''}{\rho C_p U_\tau}} \quad (4.43)$$

For  $y^+ > y_T^+$ , the temperature represents the buffer zone where the temperature profile can in general be represented as

$$T^+ = Pr_{tu}(u^+ + \mathbf{P}) \quad (4.44)$$

The function  $\mathbf{P}$  provides a smooth transition from the viscous to the logarithmic temperature profile and can be calculated with Equation 4.45. In addition to this model, there are also other models proposed by Launder and Spalding (1972), but not discussed in this thesis.

$$\mathbf{P} = -\left(1 - \frac{Pr}{Pr_{tu}}\right)y_T^+ \quad (4.45)$$

ANSYS Fluent provides several near-wall treatment options with their strengths and weaknesses. For the geometry in this study, where separation is present, two near-wall treatment methods are of particular interest – “Non-Equilibrium Wall Functions” and “Enhanced Wall Treatment.” The Non-Equilibrium Wall Functions perform better for the flows with separation and adverse pressure gradient. The near-wall mesh can be relatively coarse. The Enhanced Wall treatment is used for low Reynolds flow and the flows with complex near-wall phenomena. Generally, it requires a very fine near-wall mesh capable of resolving the near-wall region, but it can handle a coarse mesh fairly well [31]. The Enhanced Wall treatment was used in this study.

#### 4.4 Calculated Parameters

As mentioned in the introduction, the aim of this study is to evaluate the heat transfer phenomena between the brake disc and the inner side of the wheel as a function of various parameters. Table 4.1 lists five selected parameters, which impact the heat transfer processes in the model.

**Table 4.1:** List of Evaluated Parameters

#	Parameter
1	Mesh dependency
2	RANS turbulence models
3	Vehicle velocity
4	Brake disc temperature
5	Brake system configurations

These parameters have been chosen in such a way as to provide insight on the thermal interaction in the wheel-brake system. The first two parameters on the list - the mesh dependency and RANS turbulence models - focus on the evaluation of the precision and quality of the simulated model. As the experimental data are not available, it is difficult to draw a definite conclusion on the precision and quality of the model. Nevertheless, the obtained results provide valuable information about the aerodynamic and thermal behavior of the simulated system.

The last three parameters – vehicle velocity, brake disc temperature, and the brake system configuration – evaluate the heat transfer on the wheel-brake system parametrically.

The results for average heat transfer coefficients and average temperature on the inner side of the wheel are plotted against the corresponding variables.

Next, the evaluated parameters listed in Table 4.1 are briefly discussed.

- 1) The mesh dependency parameter. Five cases of different cell numbers and sizes are evaluated in terms of heat transfer coefficients, mass flow rate, and the drag coefficient. The goal is to find the least computationally expensive mesh definition that provides mesh independent results for the remaining four parameters. The mesh height of the first cell adjacent to the wheel-brake system is targeted to take the value  $y^+ \sim 1$ . With an initial guess for the mesh size near the wall, a few iterations are sufficient to refine the mesh to the desired  $y^+$ . The  $y^+$  distribution plots for these iterations are extracted from the CFD results using a post-processor.
- 2) RANS Turbulence Models. Three RANS turbulent models - Realizable  $k - \varepsilon$ , Standard  $k - \omega$  and Shear Stress Transport (SST)  $k - \omega$  - are compared among each other. The (SST)  $k - \omega$  model is chosen as a baseline due to the promise of the superior performance. For all three simulations the initial conditions are set the same. That way, the differences in the calculated results are only due to the selected turbulence model. Since the empirical velocity field is not available to confirm the accuracy of the results, the best judgment is used to interpret the simulation.
- 3) Vehicle velocity. Five vehicle velocity values are chosen to perform the parametric analysis with SST  $k - \omega$  model. These values are 0.1 m/s, 1 m/s, 3 m/s, 6 m/s, 10 m/s. The first value 0.1 m/s is chosen as non-zero, so that the natural convection cooling will not be dominant. It is possible that the natural convection could take place at lower

velocities of the vehicle, but that would add an additional variable making the results comparison for the five velocities depended on more than just one variable.

- 4) Brake Disc Temperature. Four brake disc temperature values are chosen to perform the parametric analysis with SST  $k - \omega$  model. The values are 300 °C, 400 °C, 500°C, and 600 °C.
- 5) Brake system configurations. Two brake system configurations presented in Chapter 3 are simulated with Shear Stress Transport (SST)  $k - \omega$  model and compared in terms of the heat transfer phenomena on the wheel-brake system.

These five evaluated parameters are presented and discussed in the next chapter with help of post-processing results shown in Table 4.2.

**Table 4.2:** List of Post-Processing Results Calculated with ANSYS Fluent

#	Post-Processing Result
1	Velocity profile and circulation between the wheel and the brake system
2	Pressure and separation regions on the inner side of the wheel
3	Turbulence and kinetic energy around the system
4	Temperature distribution on the inner side of the rim and spokes
5	Local heat transfer coefficients on the inner side of the rim and spokes

#### 4.5 Inlet, Initial, and Boundary Conditions

The model is simulated using SST  $k - \omega$  turbulence model for a steady state case, with an exception of the RANS turbulent model comparison. The moving components are

defined as moving walls. The gravity is considered in the simulation. A no-slip boundary condition is applied to the walls. The pressure-based coupled algorithm in Fluent was used to solve the local instantaneous mass, momentum, and energy conservation equations. The air stream is modeled as incompressible fluid with air properties shown in Table 4.3. The air properties are assumed to be pressure-independent, as the air stream velocity is low for a compressibility effects to be significant.

**Table 4.3:** Air Properties for an Incompressible Fluid

<b>Variable</b>	<b>Description</b>	<b>Value</b>
$\rho_f$	Density	1.225 [kg/m <sup>3</sup> ]
$k_f$	Thermal Conductivity	0.0242 [W/m-K]
$C_{pf}$	Specific Heat	1006 [J/kg-K]
$\mu_f$	Viscosity	$1.789 \times 10^{-5}$ [kg/m-s]

For the radiation heat transfer, the model is assumed to be optically thin, meaning the fluid is transparent to the radiation at wavelengths where the heat transfer occurs. The radiation heat transfer occurs only between the walls. The natural convection is not considered in this study.

Using Equation 4.46, the angular velocity of the wheel and brake disc can be determined knowing the vehicle velocity and the outer radius of the tire.

$$N(\text{rpm}) = \frac{60}{2\pi r} v(\text{m/s}) \quad (4.46)$$

where ( $N$ ) is number of revolutions per minute, ( $v$ ) is the forward vehicle velocity, and ( $r$ ) is outer radius of the tire with  $r = 0.313$  m. The wheel's angular velocity is shown in Table 4.4 for five vehicle velocity cases.

**Table 4.4:** Wheel's angular velocity as a function of vehicle velocity

<b>Velocity, [m/s]</b>	<b>N, (rpm)</b>
0.1	3.05
1	30.5
3	91.5
6	183
10	305

## CHAPTER 5

### RESULTS AND DISCUSSION

#### 5.1 General Remarks

The simulation on the wheel-brake system was performed for a steady state case, where the temperature of the brake disc is fixed to a specified value, as well as the forward velocity of the vehicle. As discussed in Chapter 2, the actual braking of the vehicle, on the contrary, is a transient process. In this study, the prolonged braking-accelerating cycles (Figure 2.4) are modeled having a constant averaged surface temperature, which is expected to lead to an averaged heat transfer rate among the components. For example, if the experimental multi-cycle measurement constitutes the average brake disc temperature of 400°C with the minimum value of 300 °C and the maximum value of 500 °C, then the simulation of the brake disc temperature with the constant value of 500 °C would overpredict the heat transfer rate on this system. That overprediction is suggested for a hypothetical case, where a wheel with 100,000 operated miles would have revolved around 85 million times, while, statistically, experiencing a significant number of these temperature picks at different points of time. In order to simulate the potential thermal yield of the thermoplastic composite material over time, it was reasoned to perform the worst-case scenario simulation of the wheel-brake system as a steady-state case with a rotor pick temperature taken as a constant.

For the most adequate accuracy of the simulation results, the numerical model should be correlated with the experiments on a physical model. The parametric study in this thesis answers to what extent the changes of the selected parameters impact the heat transfer on the wheel-brake system. It is expected that the degree of change in output parameters estimated numerically, would correlate well with the degree of change measured on a physical system, even if the mean values are different to some extent. However, this statement needs to be validated with the experimental work, in order to reduce uncertainty in the interpretation of the results.

#### 5.1.1 Convergence

For all simulations in this study, the convergence criterion with a tolerance of  $10^{-3}$  was applied on the residuals for the continuity and momentum equations. A convergence criterion of  $10^{-4}$  was used for the energy equation residuals. These tolerance criteria are acceptable for performance of an adequate simulation with Fluent, however, a tolerance of  $10^{-6}$  is preferred for improved accuracy [31]. The convergence of the inlet and outlet mass flow rate and drag coefficient on the wheel for all simulations were monitored as well.

#### 5.1.2 Grid Dependency Study

The grid dependency study was carried out for five different mesh cases ranging from 3.09 million to 8.12 million cells. Table 5.1 illustrates the details of the grid dependency

study. The cell volume increase was mostly due to refinement of the elements in the boundary layers on the wheel surfaces, so that the  $y^+$  would become less than 1. To determine if the solution was mesh independent, the drag coefficient on the wheel, the average temperature and the average heat transfer coefficient on the surfaces of the rim and spokes were recorded.

**Table 5.1:** Details on various grid configurations with estimated parameters

Grid	Cell Volume	Cells in Boundary	Max. $y^+$	Min. $y^+$	Average $y^+$	$C_d$	Mass Flow Rate	Rim Surface Temperature
	$\times 10^6$ [-]	[-]	[-]	[-]	[-]	[-]	[kg/sec]	[°C]
I	3.09	3	12	6.5	5.5	0.643	28.6	184
II	4.76	5	9.5	3.2	4.35	0.721	28.6	198
III	5.94	8	4.4	0.98	1.3	0.758	28.6	201
IV	7.38	10	2.1	0.56	1.13	0.852	28.6	204
V	8.12	14	1.4	0.31	0.89	0.880	28.6	209

The resulting average values were compared. It can be seen that the solutions IV and V have the results for the three recorded variables close to each other. The maximum differences were 0.028 and 4.6 °C for the drag coefficient and the temperature on the rim, respectively. However, the grid configuration IV has the average  $y^+$  slightly larger than 1. Therefore, the grid configuration V has been chosen to perform the simulations in the parametric study.

## 5.2 RANS Turbulent Models Comparison

Three RANS turbulent models - Realizable  $k - \varepsilon$  with Enhanced Wall-Function treatment, Standard  $k - \omega$  and Shear Stress Transport (SST)  $k - \omega$  - are compared among each other in this section. As discussed in Chapter 4, the (SST)  $k - \omega$  represents a baseline and is used for parametric studies. Table 5.2 illustrates the calculated results for inlet velocity of 3 m/s and the brake disc temperature of 500 °C.

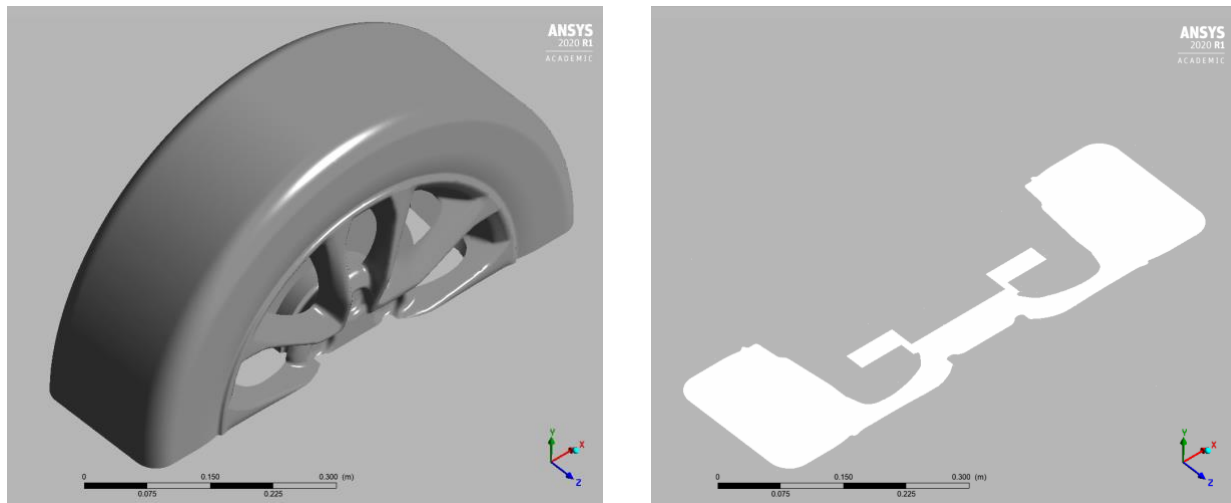
**Table 5.2:** Monitored variables on the wheel-brake system using the RANS models

RANS Turbulence Models	$C_d$	Mass Flow Rate	Rim Surface Temperature	Heat Transfer Coefficient on Inner Rim
	[-]	[kg/sec]	[°C]	[W/m <sup>2</sup> K]
$k - \varepsilon$ Realizable	0.853	28.6	205	14.1
Standard $k - \omega$	0.874	28.6	202	13.6
SST $k - \omega$	0.880	28.6	209	14.8

The comparison shows that the parameters are not very much different from each other. Therefore, it was decided not to perform a further comparison of the turbulent models for different inlet velocities. The subchapter discussed next compares the aerodynamic results in terms of velocity, pressure, and kinetic energy fields.

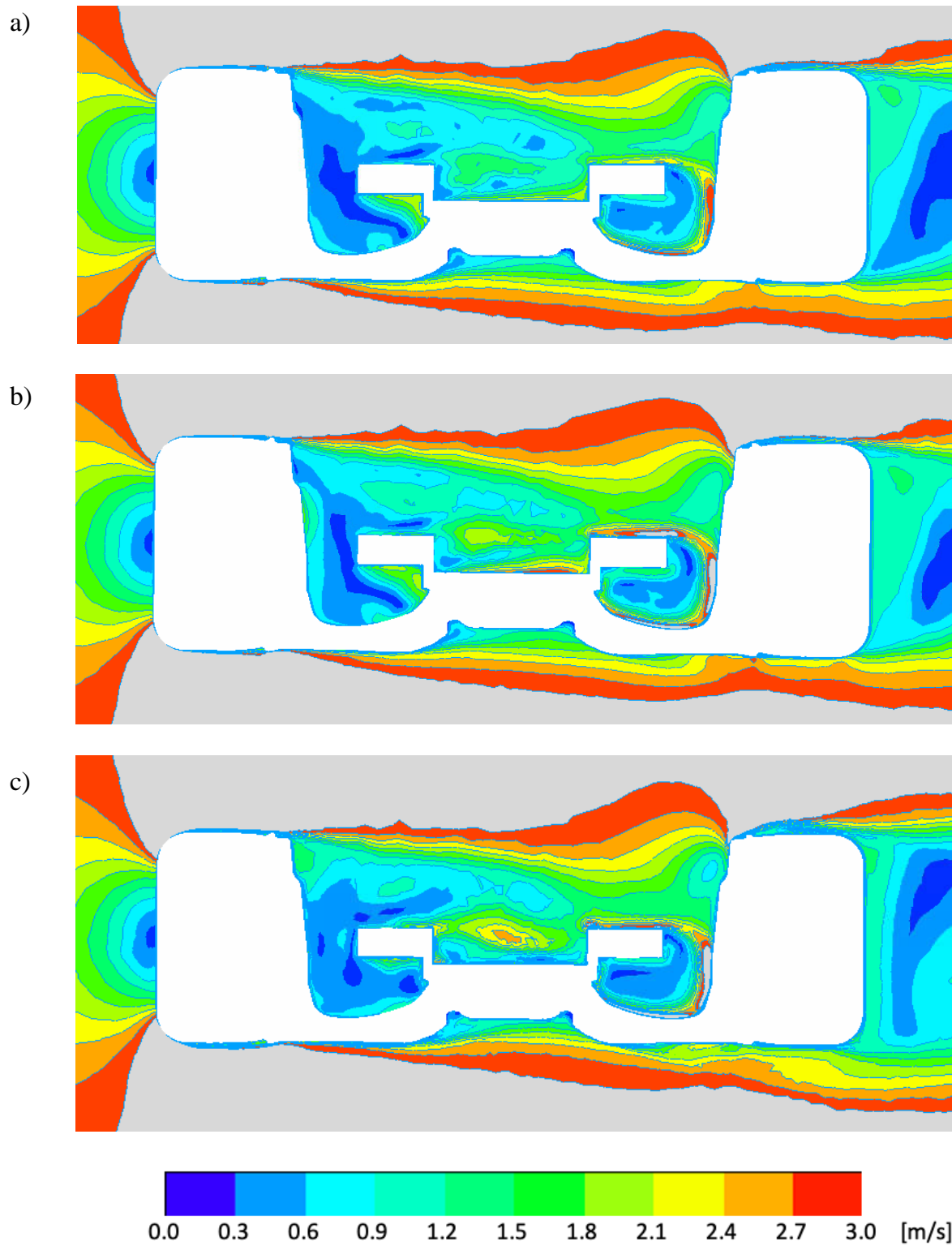
### 5.2.1 Aerodynamic Results

Figure 5.1 depicts the XZ plane through the center of the wheel model, on which the calculated results are presented and evaluated in this chapter. For additional information, Appendix B contains the discussed results plotted on a YZ plane plotted through the center of the wheel as well.



**Figure 5.1:** Depiction of the plane for the illustration of the results

Figure 5.2, Figure 5.3, and Figure 5.4 illustrate the velocity profile, pressure, and kinetic energy for three RANS turbulence models, respectively. The velocity and pressure profiles for the three simulations are very similar. The Realizable  $k - \varepsilon$  model underpredicts slightly the pressure in the center of the brake disc. The (SST)  $k - \omega$  model calculated less kinetic energy in front and on the sides of the wheel. The out of the range data are not displayed in the result images.



**Figure 5.2:** Velocity profile for a) Realizable  $k - \varepsilon$ , b) Standard  $k - \omega$  c) SST  $k - \omega$

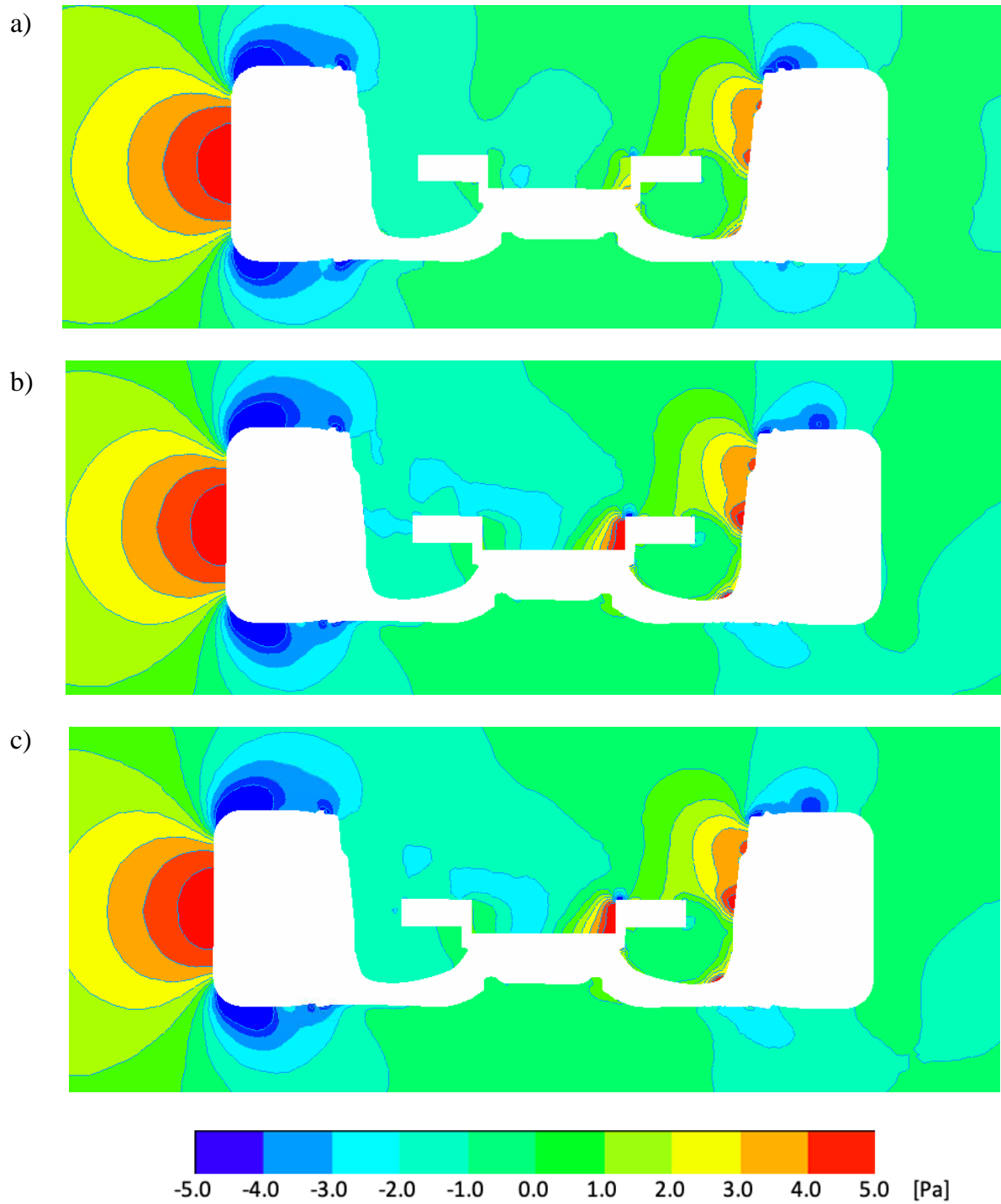


**Figure 5.3:** Pressure profile for a) Realizable  $k - \varepsilon$ , b) Standard  $k - \omega$  c) SST  $k - \omega$

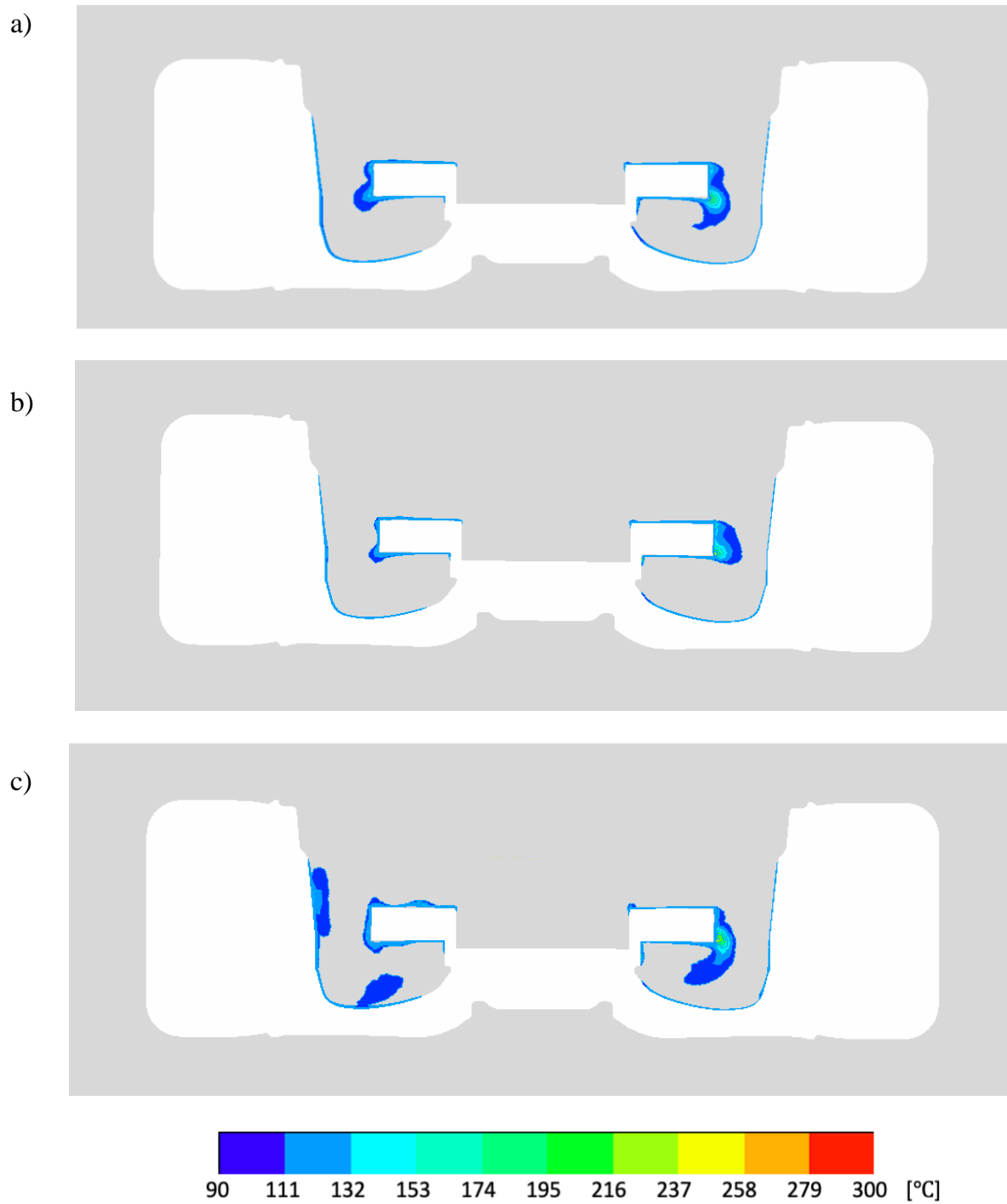


**Figure 5.4:** Kinetic Energy for a) Realizable  $k - \epsilon$ , b) Standard  $k - \omega$  c) SST  $k - \omega$

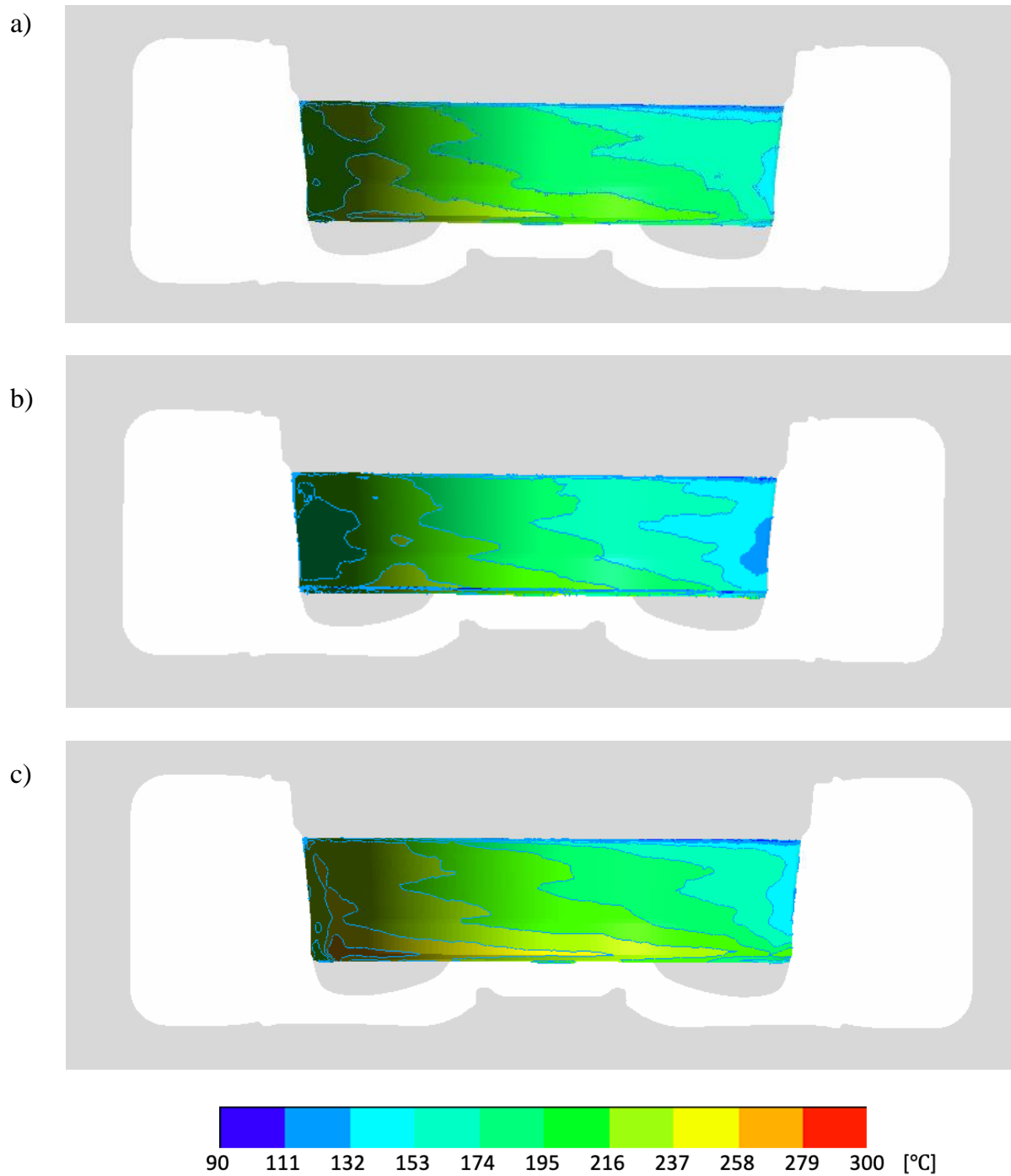
### 5.2.2 Heat Transfer Results

Figure 5.5 illustrates the temperature profile of the air adjacent to the surfaces of the brake disc and the rim. The temperatures out of the specified range are not displayed in the presented results to simplify the interpretation of the results. It can be seen that the inner surface of the rim heats up through radiation from the brake disc. As a result, the rim surface transfers heat to the adjacent air, while there is no visual indication that the convection contributes in any way to the heat transfer between the brake disc and the rim. The c) SST  $k - \omega$  model calculates the air temperature distribution close to the hot surfaces to be slightly larger than for the other two models. It also can be seen in Table 5.2, that the average surface temperature of the rim for the SST  $k - \omega$  model is only 7 °C higher than the Standard  $k - \omega$  turbulent model and only 4 °C higher than the Realizable  $k - \varepsilon$  turbulent model.

Figure 5.6 presents the temperature distribution on the inner side of the rim for three RANS turbulence models. The temperature distribution is not uniform in the axial direction and on the circumference of the inner side of the wheel. This can be explained with the way the simulation was set up. As the simulation was defined as a steady-state without moving dynamic mesh, the temperature distribution was calculated for that specific instance in time. That set up prevents each point of the rim to be periodically exposed to different temperatures and heat transports during every wheel revolution. For the transient case, the rim temperature is expected to look more uniform on the circumference and vary only in an axial direction.



**Figure 5.5:** Temperature of the air for a) Realizable  $k - \epsilon$ , b) Standard  $k - \omega$  c) SST  $k - \omega$



**Figure 5.6:** Temperature on the surface of the wheel for a) Realizable  $k - \epsilon$ , b) Standard  $k - \omega$  c) SST  $k - \omega$

## 5.3 Effect of Parameter Variations on Heat Transfer

### 5.3.1 Parametric Tests

The parametric tests were performed using the SST  $k - \omega$  turbulence model and the same mesh definition on all simulations. The only two variables were the vehicle velocity with the corresponding angular velocity of the wheel and the temperature of the brake rotor.

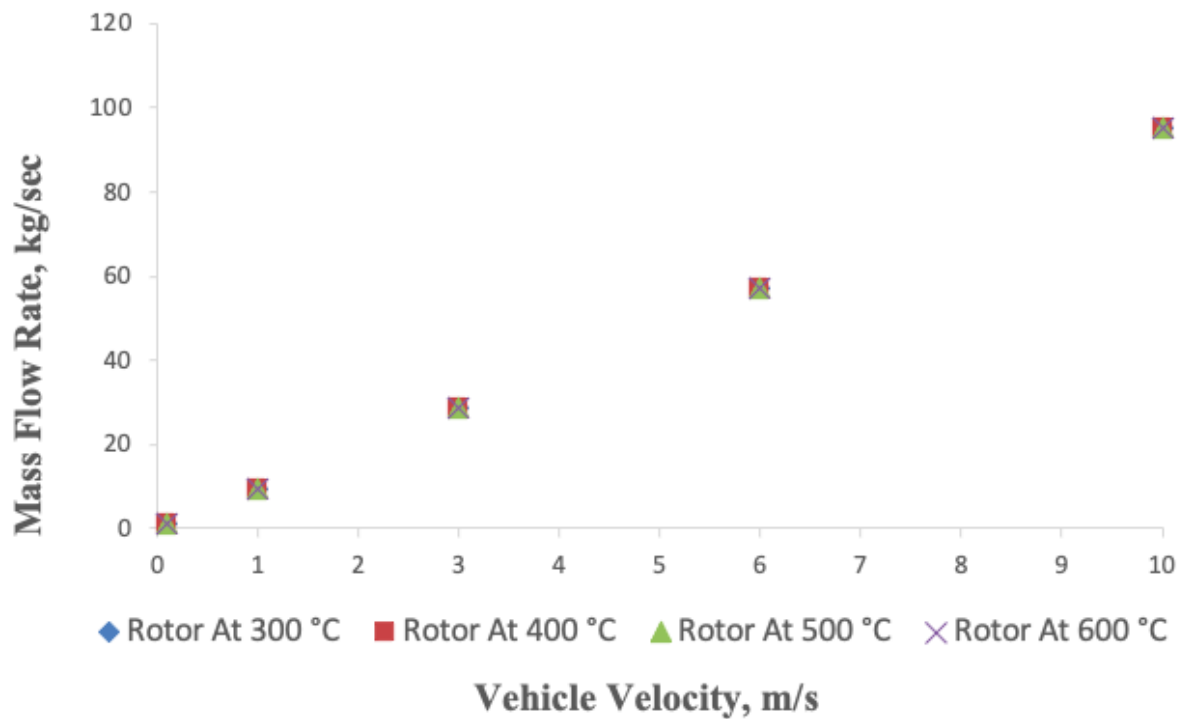
Table 5.2 sums up the 20 parametric tests discussed in this chapter.

**Table 5.3:** Varied parameters

#	Vehicle Velocity	Wheel RPM	Brake Rotor Temperature
	[m/sec]	[1/min]	[°C]
1	0.1	3.05	300
2	1	30.5	300
3	3	91.5	300
4	6	183	300
5	10	305	300
6	0.1	3.05	400
7	1	30.5	400
8	3	91.5	400
9	6	183	400
10	10	305	400
11	0.1	3.05	500
12	1	30.5	500
13	3	91.5	500
14	6	183	500
15	10	305	500
16	0.1	3.05	600
17	1	30.5	600
18	3	91.5	600
19	6	183	600
20	10	305	600

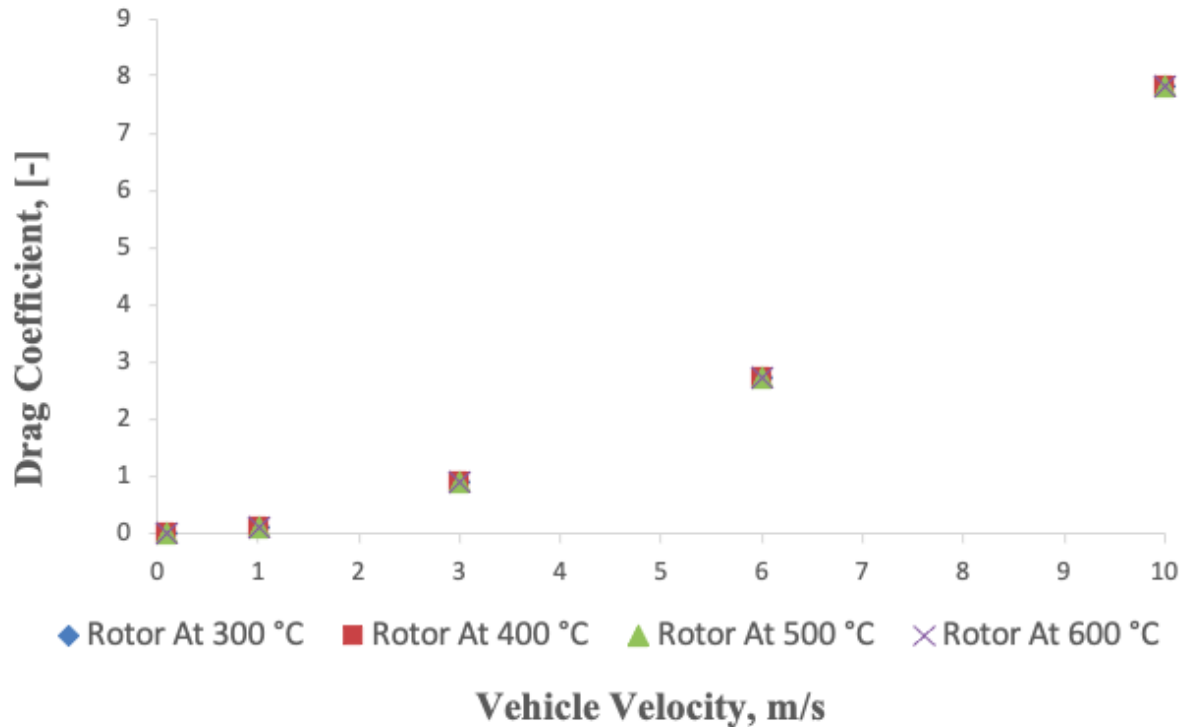
### 5.3.2 Aerodynamic Results

The mass flow rate for twenty parametric tests is shown in Figure 5.7. The temperature of the brake rotor has no effect on the mass flow rate, while it is linearly proportional to the vehicle velocity.



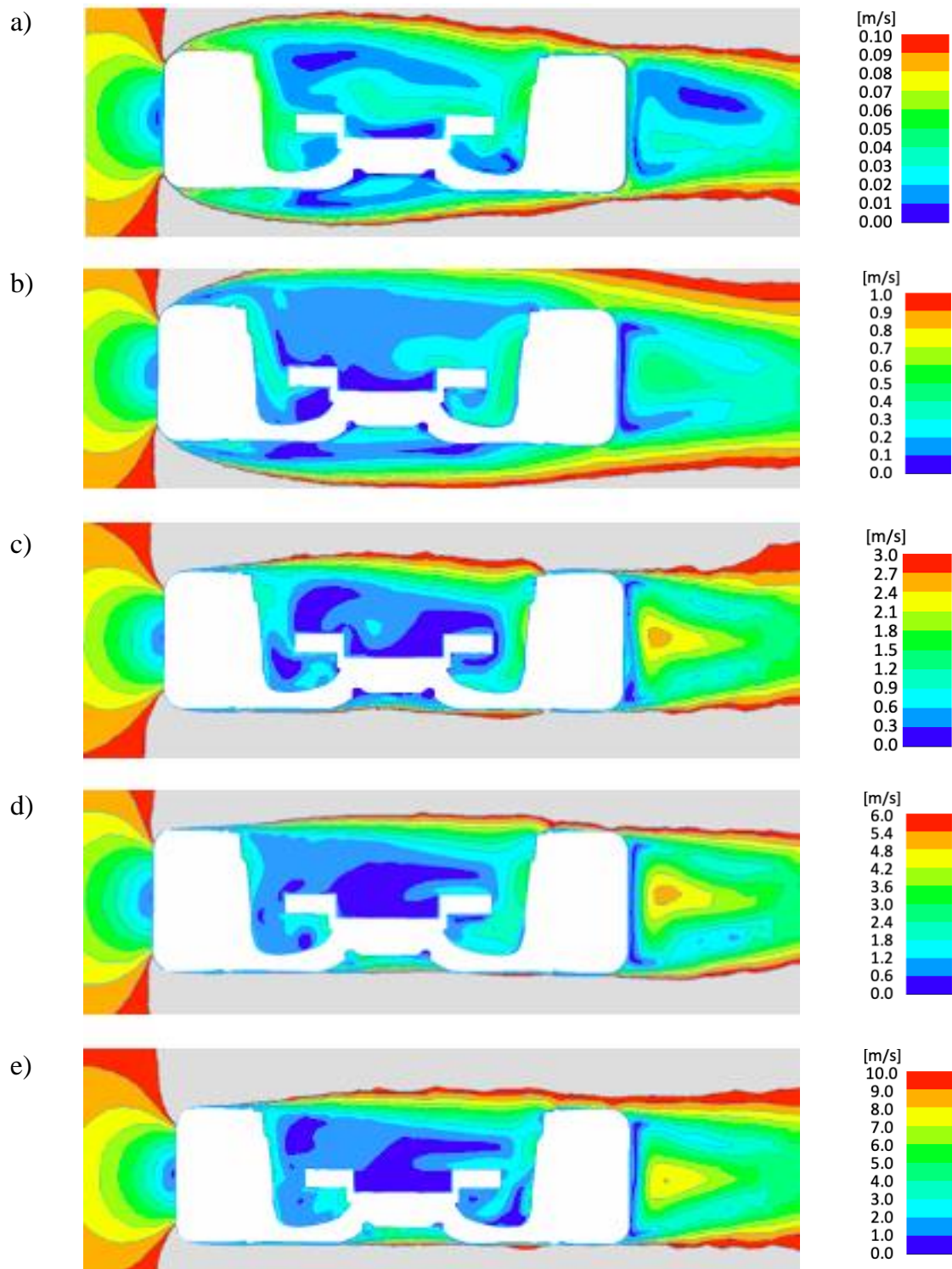
**Figure 5.7:** Mass Flow Rate

The drag coefficients for the parametric tests plotted in Figure 5.8 shows no dependency on the temperature of the system. The drag coefficient parabolically increases with the increasing vehicle velocity.

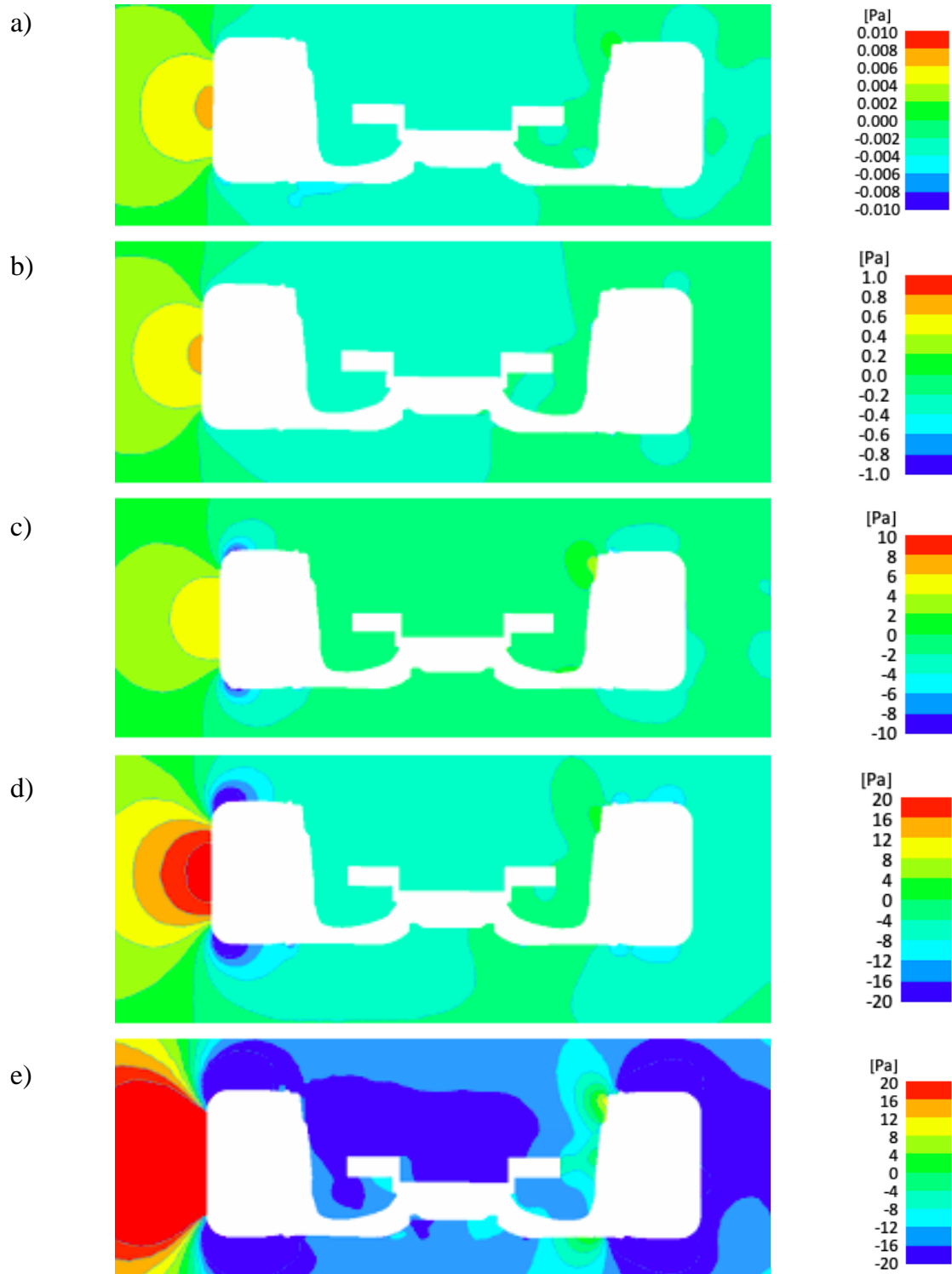


**Figure 5.8:** Drag Coefficient

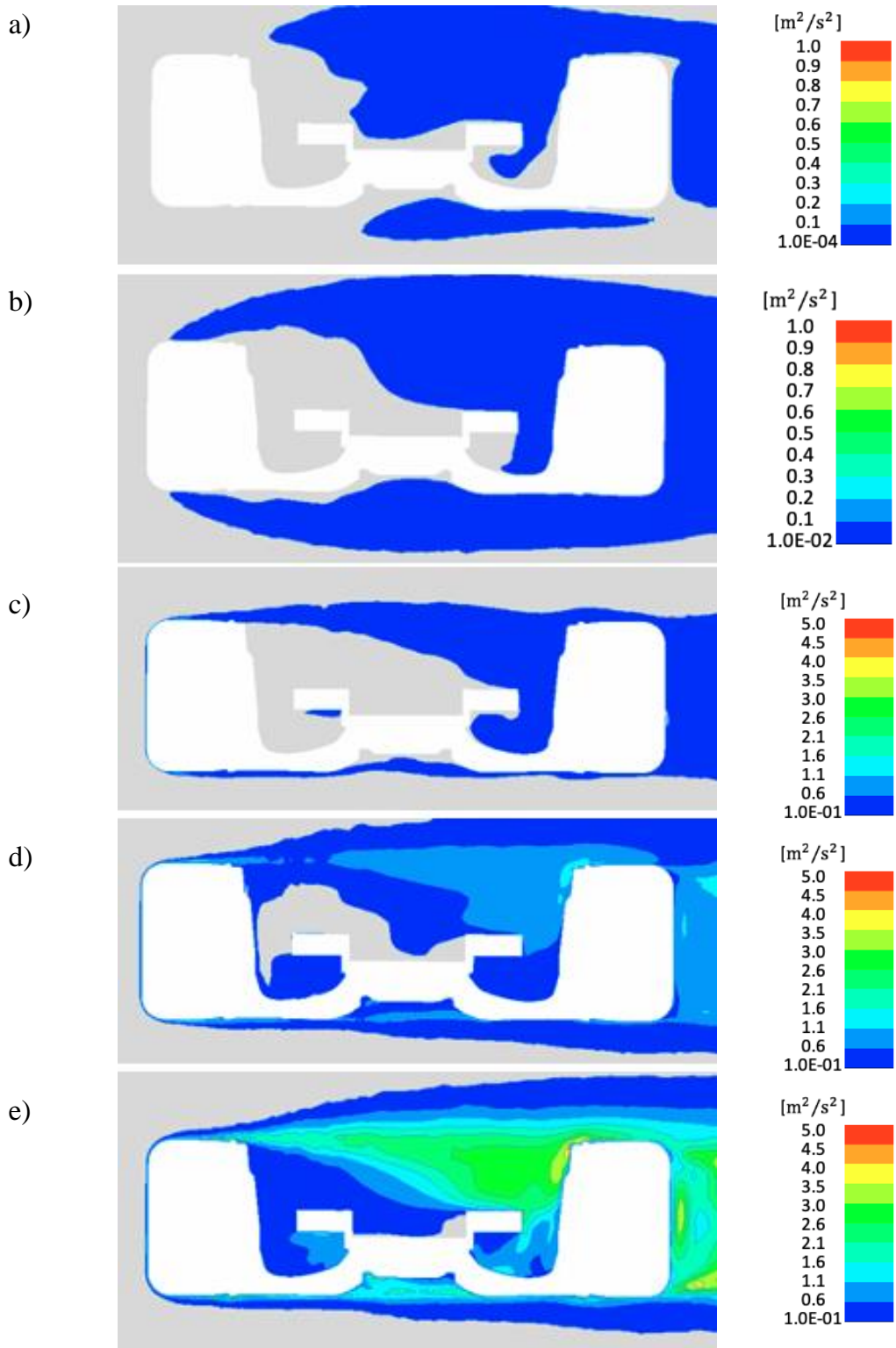
Figure 5.9, Figure 5.10, and Figure 5.11 depict the air velocity, pressure, and kinetic energy for the parametric tests, respectively. The brake disc temperature has no effect on the aerodynamic results, at least, using this method of CFD modeling. The calculated aerodynamic results only vary as a function of the vehicle velocity. All plotted results for different parametric tests have different scales. That way the gradients were visually captured.



**Figure 5.9:** Air velocity for vehicle velocities a) 0.1 m/s, b) 1 m/s, c) 3 m/s, d) 6 m/s, e) 10 m/s



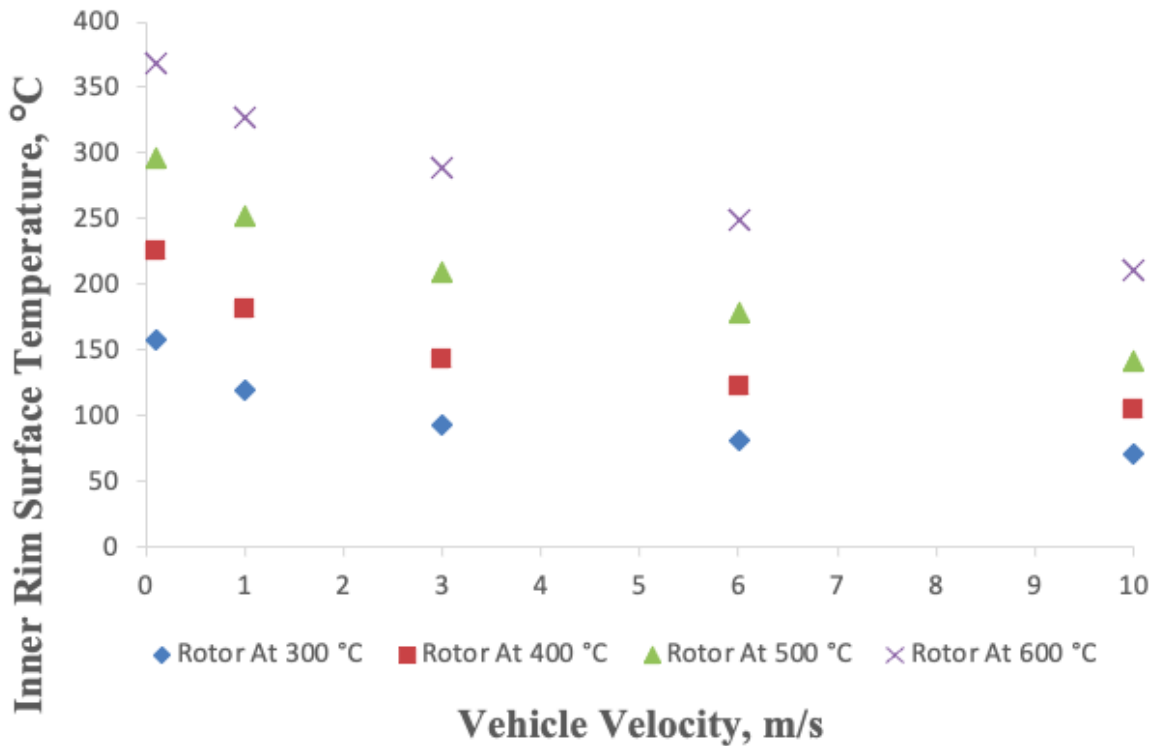
**Figure 5.10:** Pressure for vehicle velocities a) 0.1 m/s, b) 1 m/s, c) 3 m/s, d) 6 m/s, e) 10 m/s



**Figure 5.11:** Kinetic Energy for vehicle velocities a) 0.1 m/s, b) 1 m/s, c) 3 m/s, d) 6 m/s, e) 10 m/s

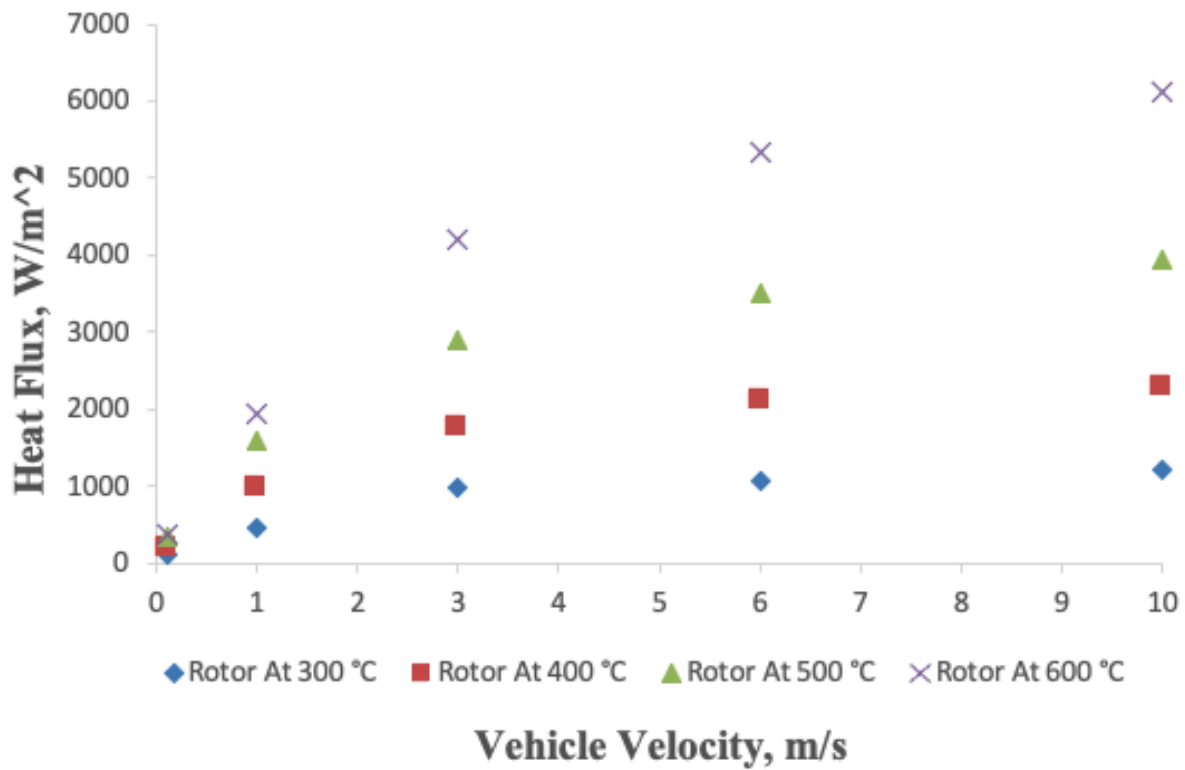
### 5.3.3 Heat Transfer Results

Figure 5.12 shows the average inner rim surface temperature plotted against the vehicle velocity for various brake rotor temperatures. It is noticed that the rim surface temperature increases with decreasing vehicle velocity and increasing brake rotor temperature. That confirms the importance of the well circulated brake system for adequate cooling of the brake rotor.

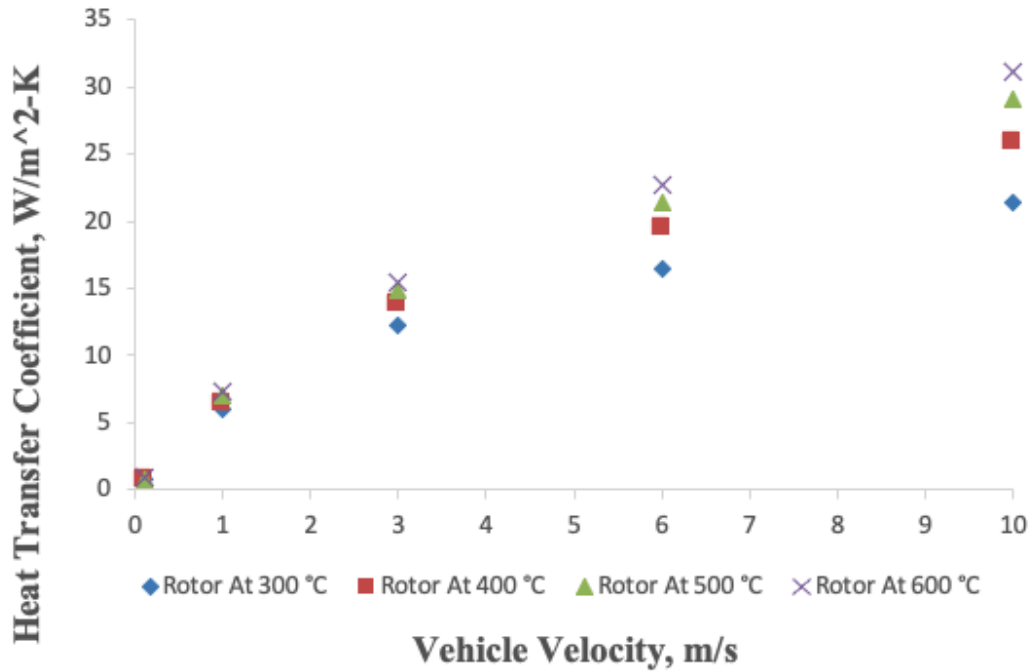


**Figure 5.12:** Inner Rim Surface Temperature vs. Vehicle Velocity for variable brake rotor temperatures

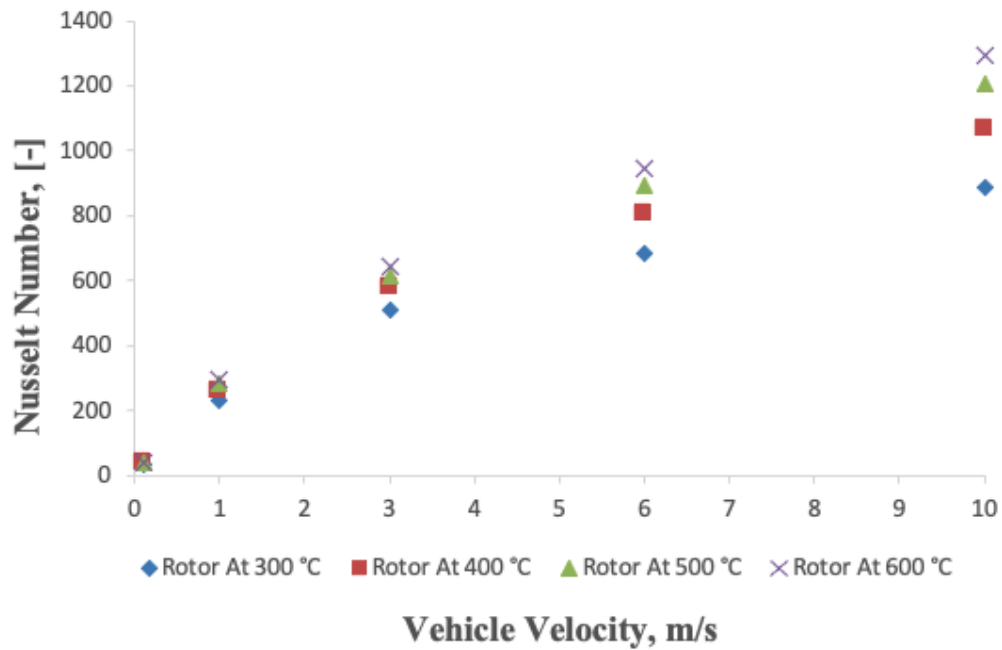
Figure 5.13, Figure 5.14, and Figure 5.15 depict the heat flux, the convective heat transfer coefficient, and Nusselt number on the inner surface of the rim for variable brake rotor temperatures, respectively. These three parameters increase in accordance to the plots with the increasing vehicle velocity and increasing brake rotor temperature.



**Figure 5.13:** Heat Flux on the rim vs. vehicle velocity for variable brake rotor temperatures

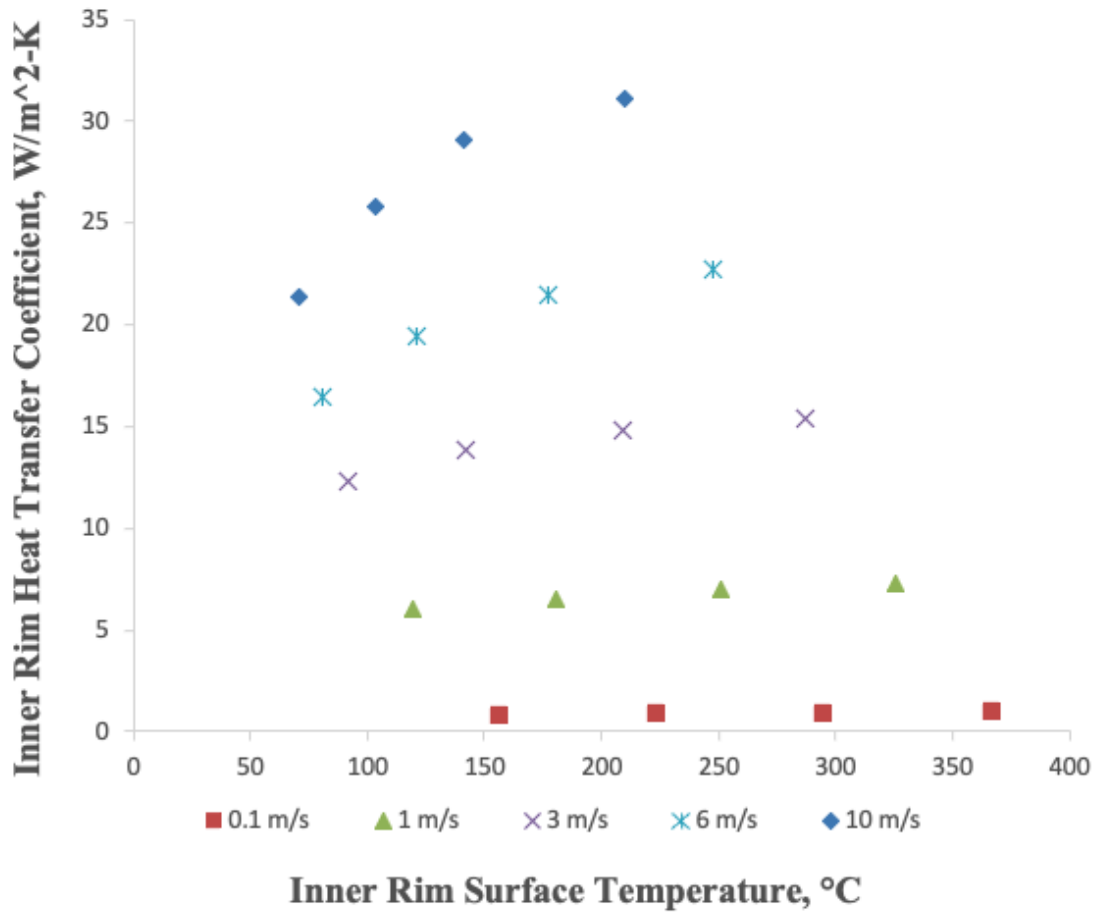


**Figure 5.14:** Rim Heat Transfer Coefficient vs. vehicle velocity for variable brake rotor temperatures



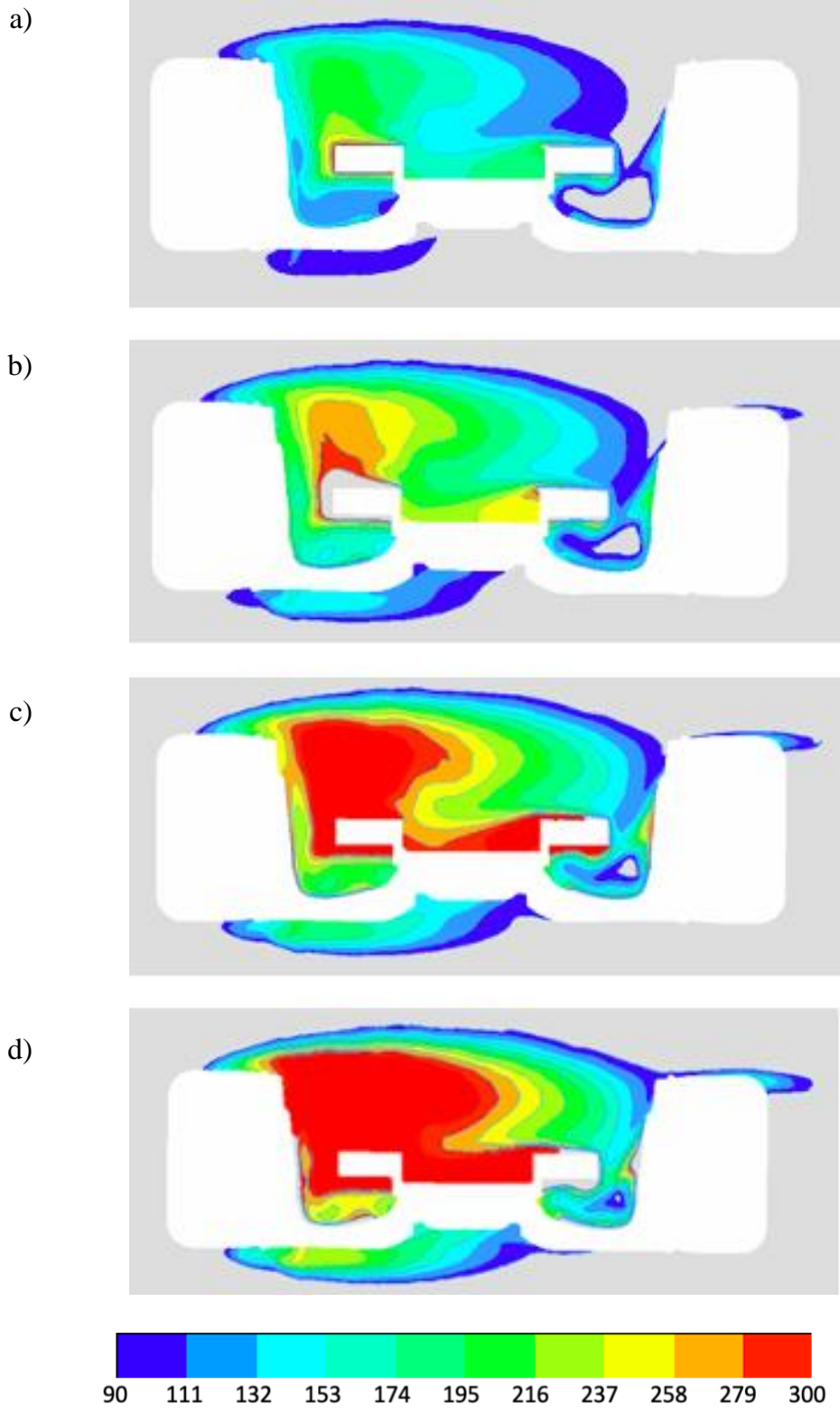
**Figure 5.15:** Nusselt Number on the rim vs. vehicle velocity for variable brake rotor temperatures

Figure 5.16 shows the inner rim heat transfer coefficient plotted against the inner rim surface temperature. The heat transfer coefficient has a significant degree of dependency on the air flow near the surface and the inner rim surface temperature.



**Figure 5.16:** Heat transfer coefficient versus temperature on the inner rim surface for various parametric variables

Figure 5.17 to Figure 5.21 depict the air temperature for all twenty parametric tests, while the scale was kept the same for all of them and the results that were out of range are not displayed.



**Figure 5.17:** Air Temperature at the vehicle velocity 0.1 m/s and a) 300°C, b) 400°C, c) 500°C, d) 600°C

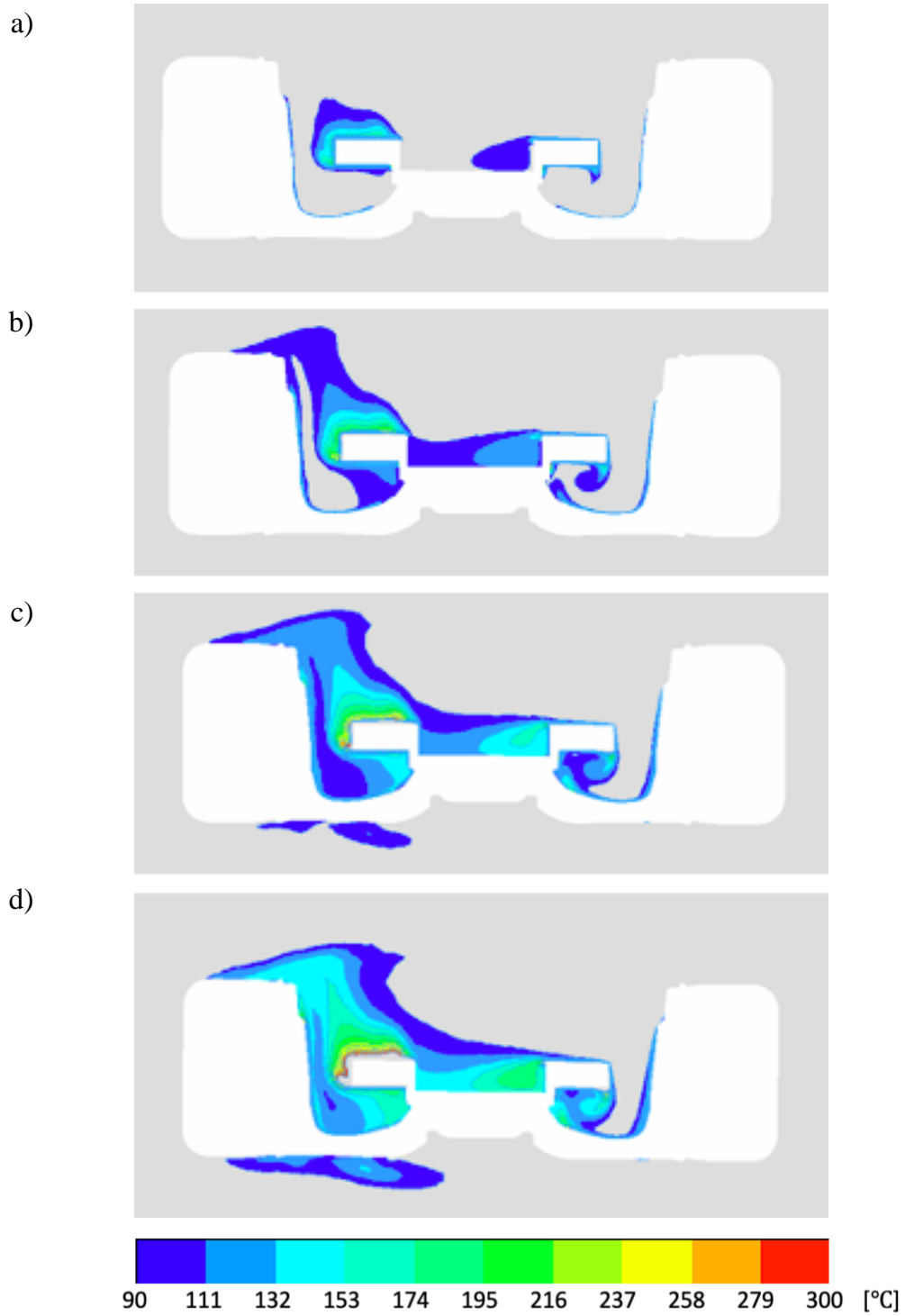


**Figure 5.18:** Air Temperature at the vehicle velocity 1 m/s and a) 300°C, b) 400°C, c) 500°C, d) 600°C

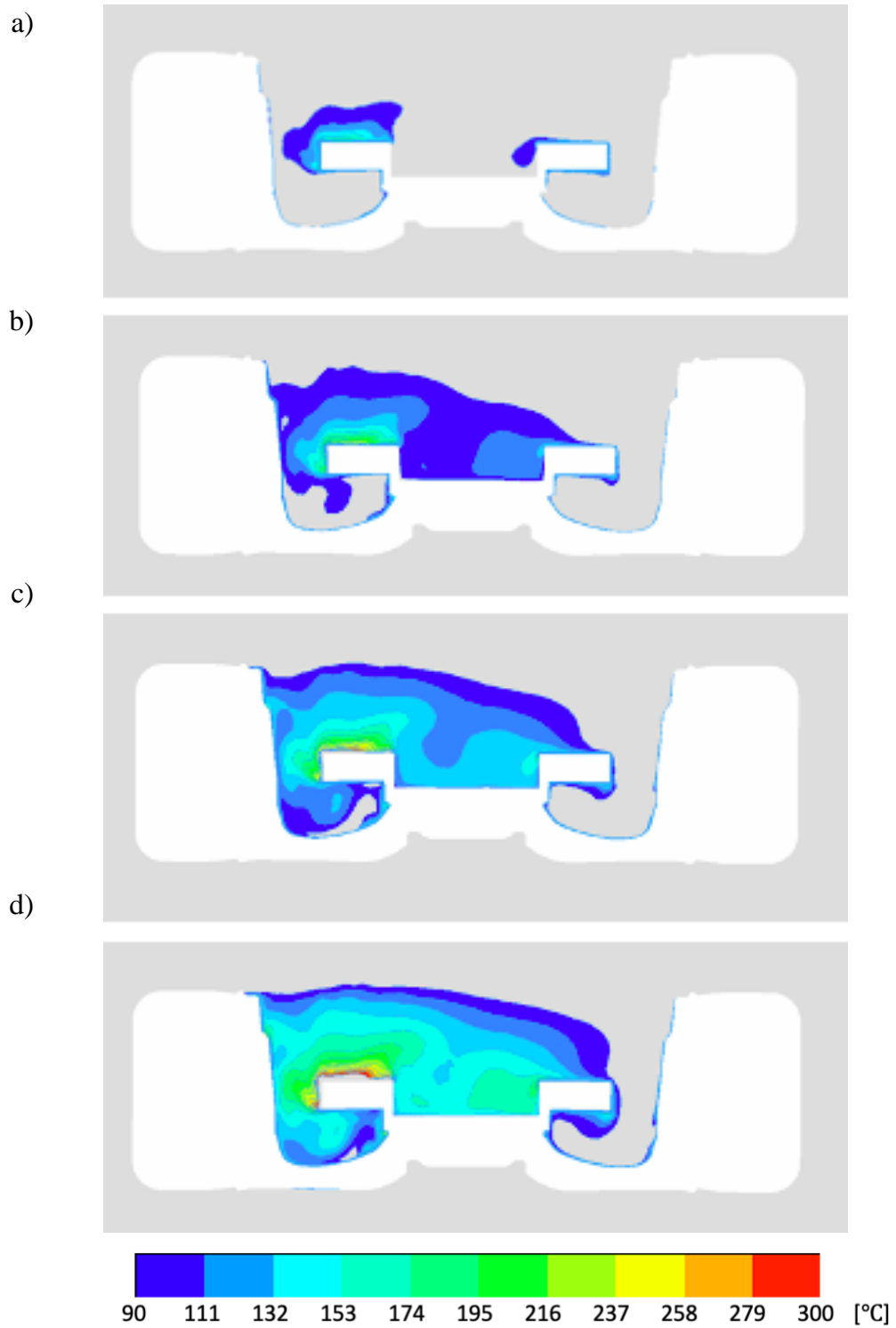


**Figure 5.19:** Air Temperature at the vehicle velocity 3 m/s and a) 300°C, b) 400°C, c) 500°C, d) 600°C

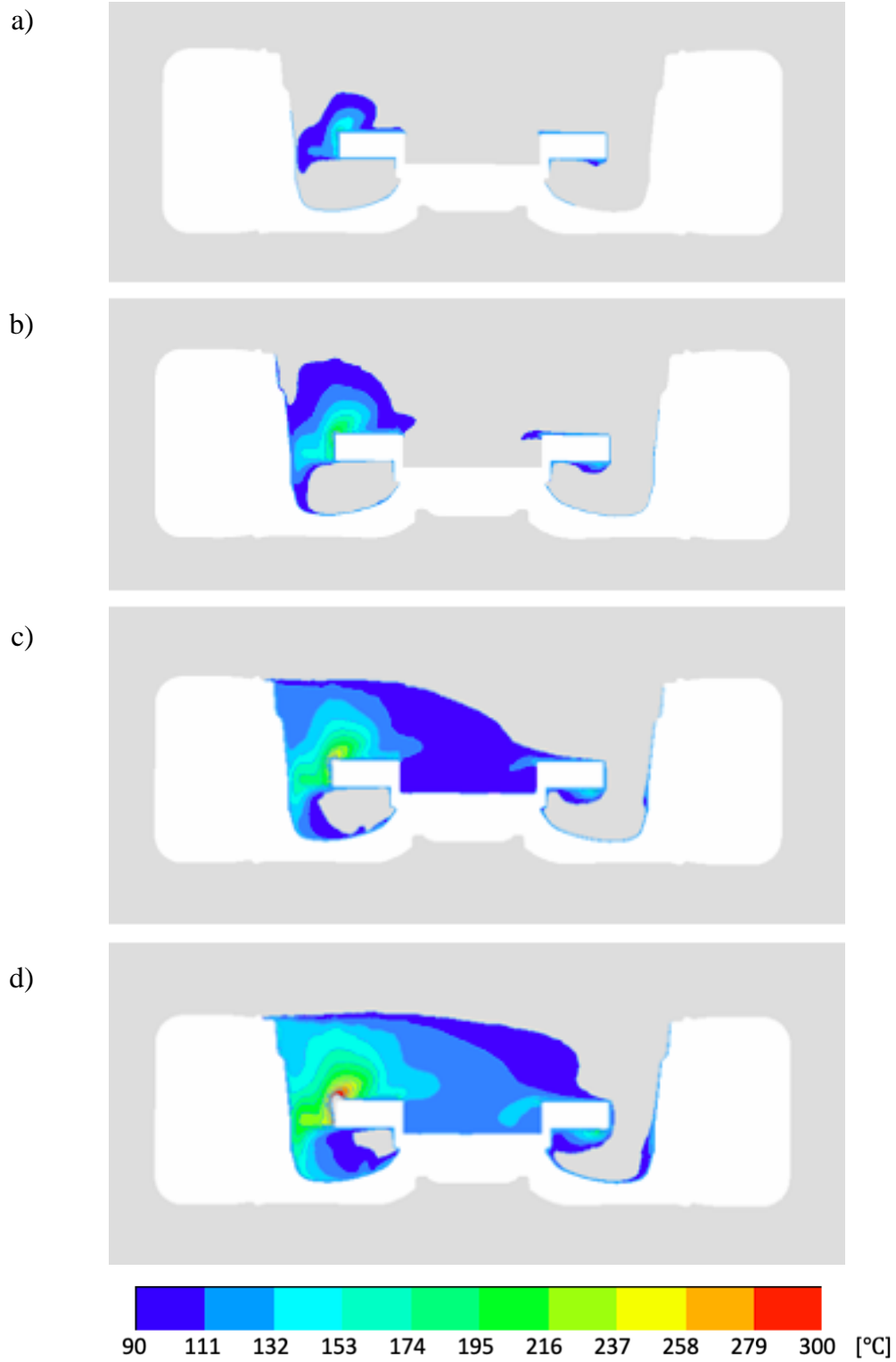


**Figure 5.20:** Air Temperature at the vehicle velocity 6 m/s and a) 300°C, b) 400°C, c) 500°C, d) 600°C

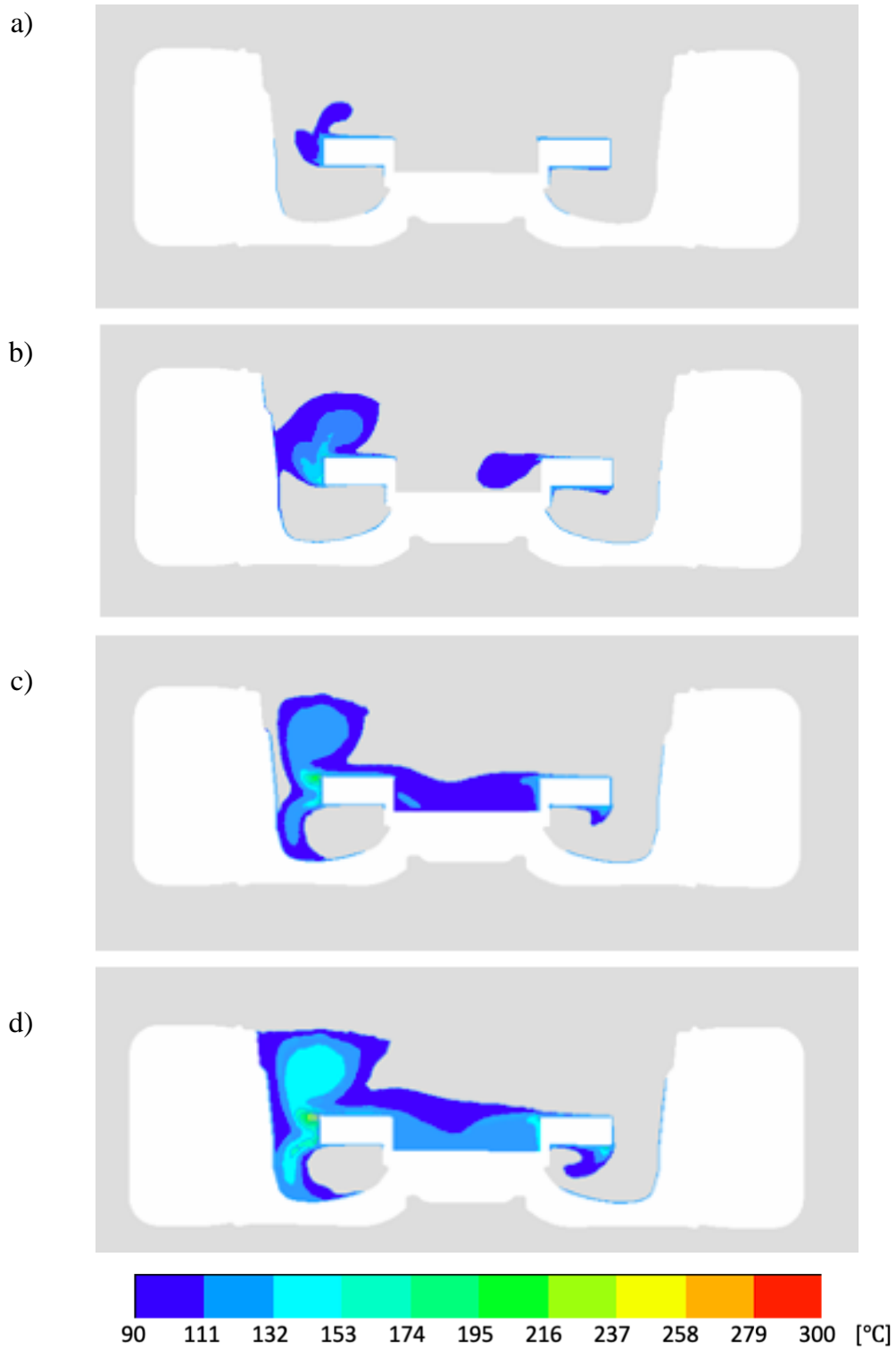


**Figure 5.21:** Air Temperature at the vehicle velocity 10 m/s and a) 300°C, b) 400°C, c) 500°C, d) 600°C

## 5.4 Brake System Configurations Comparison

### 5.4.1 Aerodynamic Results

The comparison of air velocity, pressure and kinetic energy for the two brake rotor configurations are shown in Figure 5.22, Figure 5.23, and Figure 5.24, respectively. The air velocity field slightly varies for the two different cases, while the pressure fields are nearly identical. There is a subtle difference in the kinetic energy result in the wake region.

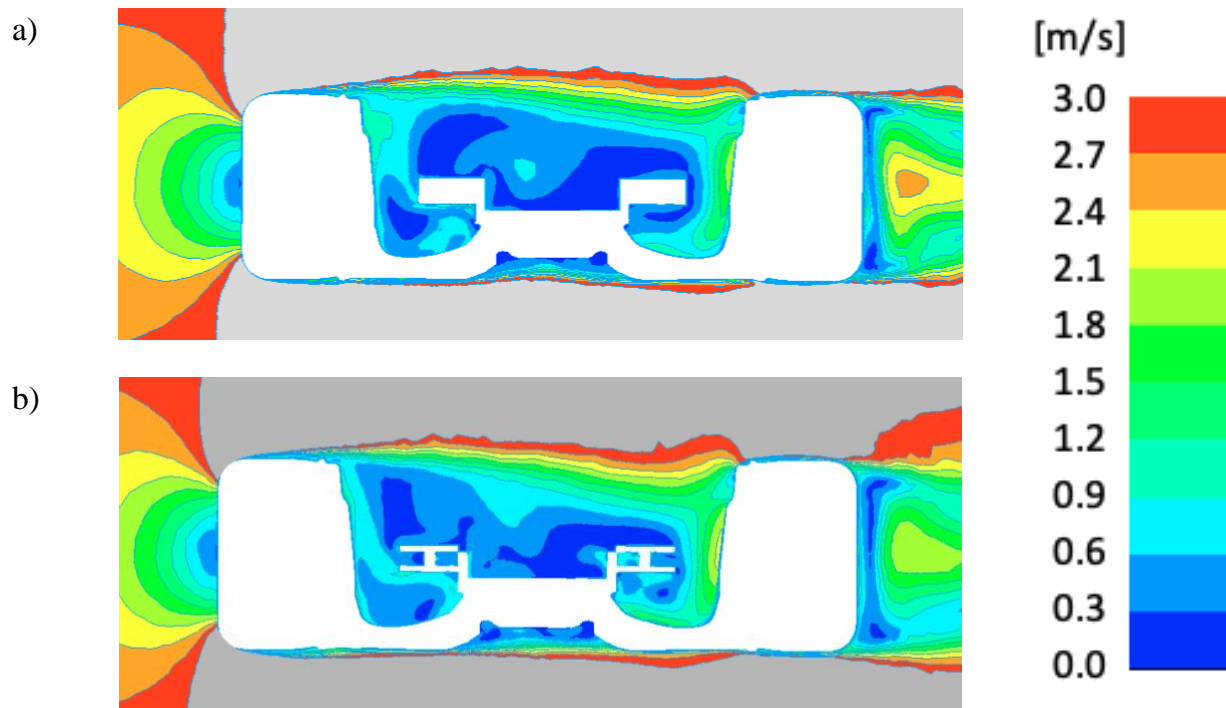


**Figure 5.22:** Air velocity for a) Solid rotor b) rotor with vents

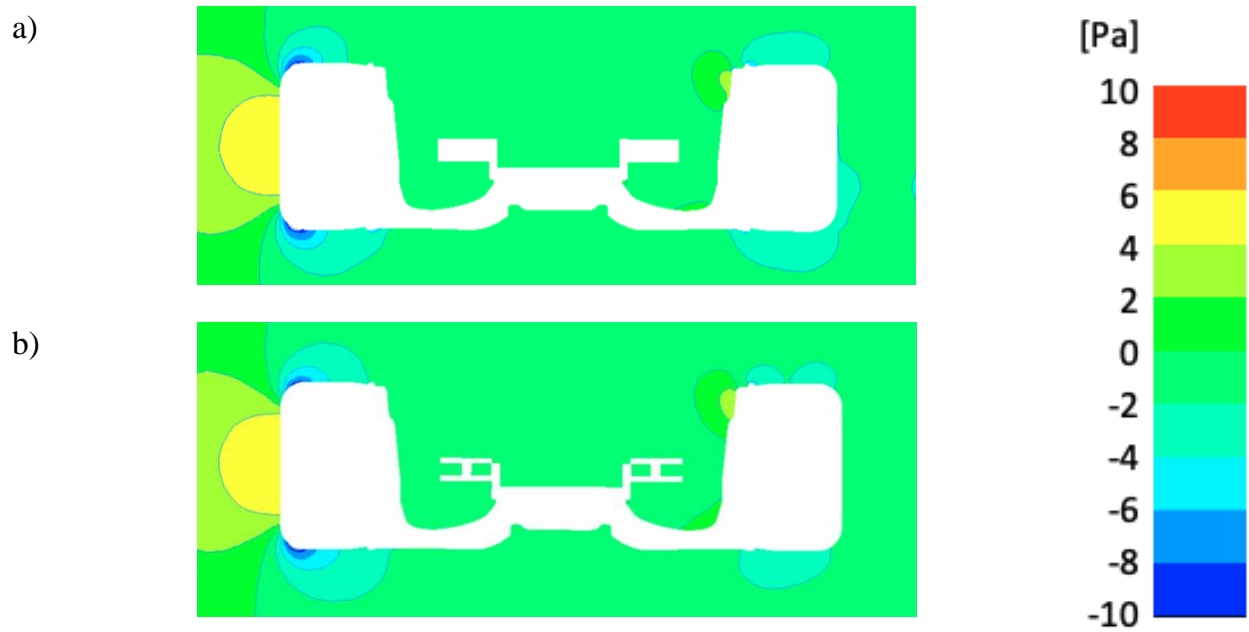


**Figure 5.23:** Pressure for a) Solid rotor b) rotor with vents



**Figure 5.24:** Kinetic Energy for a) Solid rotor b) rotor with vents

Figure 5.25 and Figure 5.26 illustrate the air velocity vectors inside the vents. It can be noticed that the air stream in vents is established from the outer toward the inner regions of the brake disc. As a result, the pre-heated air stream does not move toward the rim eliminating the danger of the additional heat transport to the rim by convection. It is possible though that in certain instances and, potentially, with different wheel-brake system design, the air flow in the vents would flow outward transporting heat from the brake disc to the rim.

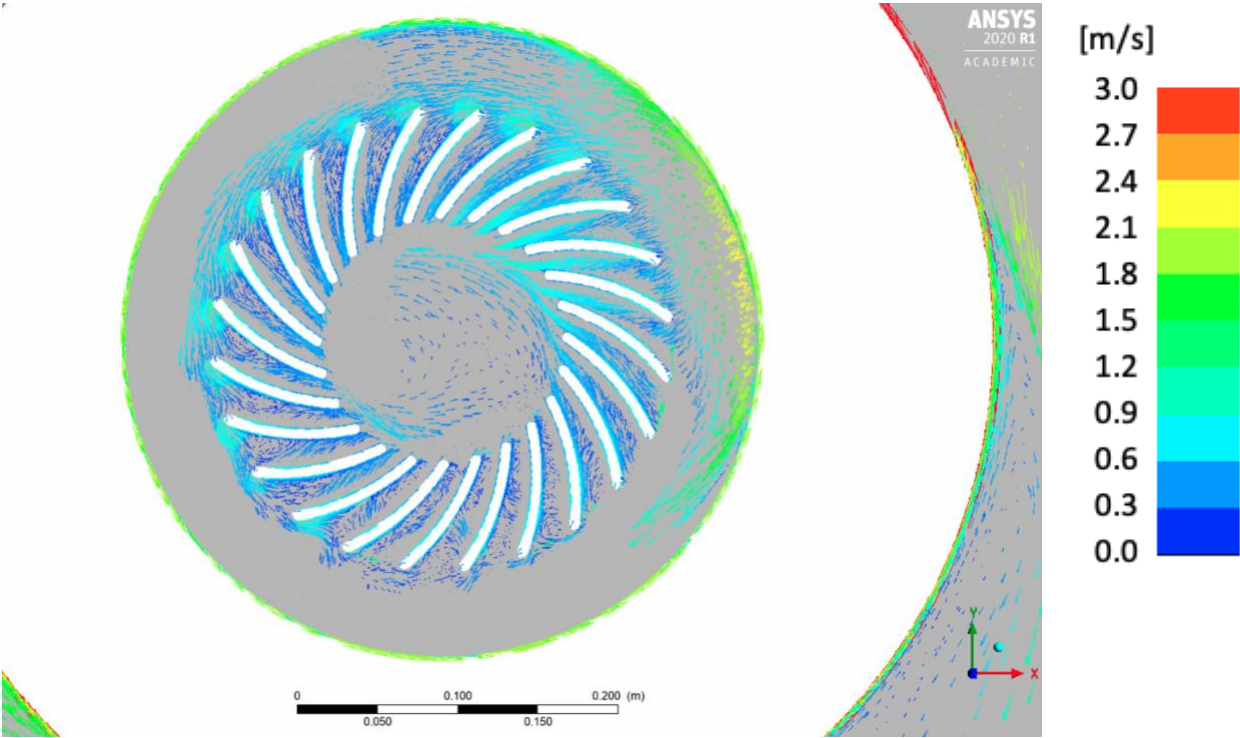


**Figure 5.25:** Air velocity vectors inside the vented rotor

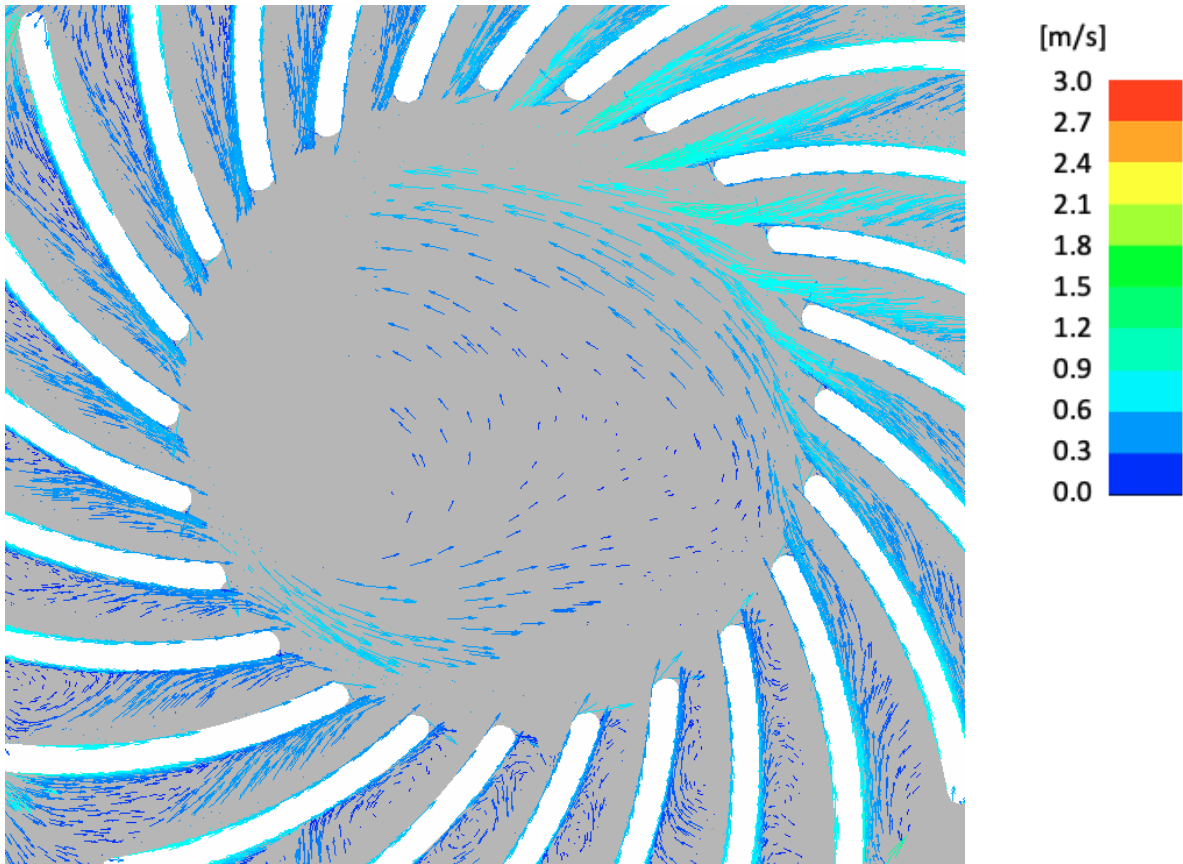


**Figure 5.26:** Air velocity vectors inside the vented rotor (close-up view)

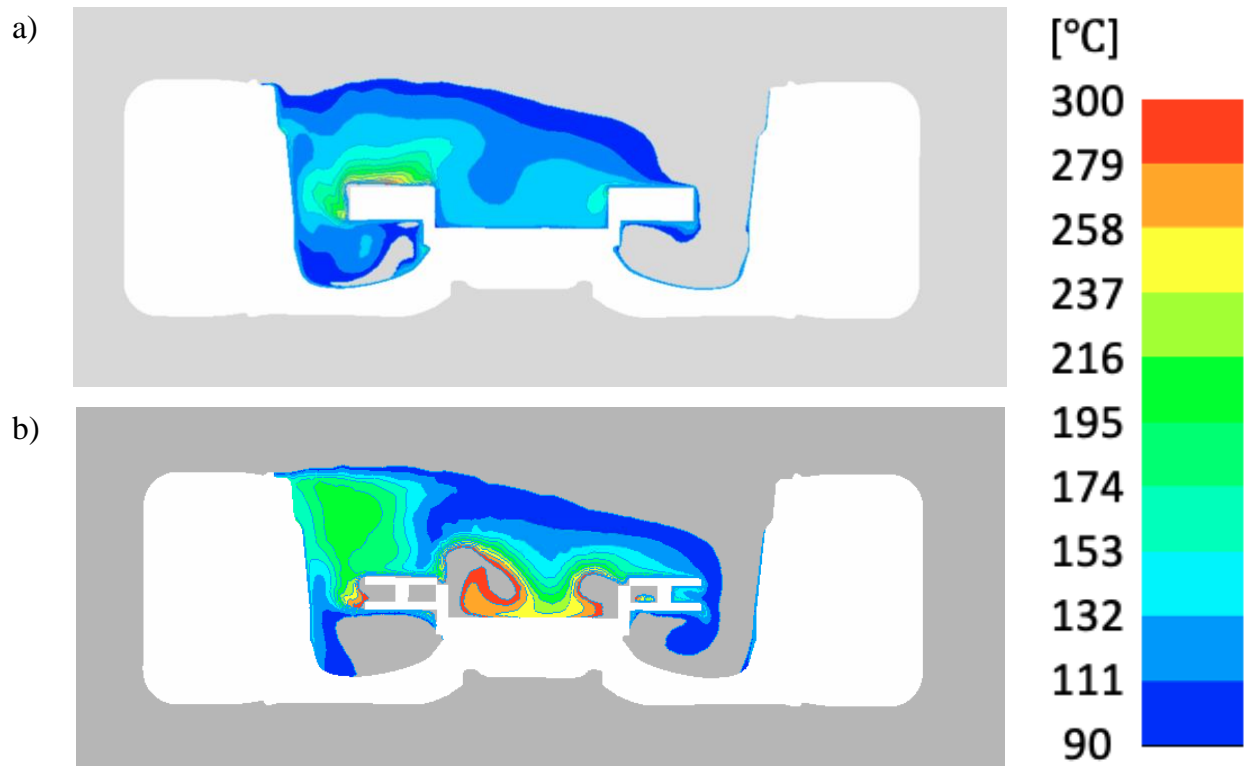
#### 5.4.2 Heat Transfer Results

Table 5.4 summarizes the estimated parameters for two brake rotors with and without the vents. It can be noted that the brake rotor configuration with vents caused the temperature and heat transfer coefficient increase on the inner side of the rim. Both models had to be discretized slightly differently, as the vents had to be modeled with a finer mesh. It is possible that the grid dependency may impact the results as well.

**Table 5.4:** Calculated Parameters for brake rotor with and without vents

Parameter	Units	Brake Rotor without Vents	Brake Rotor with Vents	Difference, %
Inlet Mass Flow Rate	kg/sec	28.6	28.6	0.00%
Drag Coefficient of Wheel-Brake system	-	0.84	0.88	4.38%
Inner Rim Surface Temperature	°C	213	221	3.51%
Heat Flux on Inner Rim Surface	W/m <sup>2</sup>	2633	2891	8.93%
Heat Transfer Coefficient on Inner Rim	W/m <sup>2</sup> K	13.3	14.8	10.5%
Nusselt Number on Inner Rim	-	549	613	10.4%

The air temperature near the brake rotor and the inner side of the rim are shown for both rotor configurations in Figures 5.27 and 5.28. The temperature results that are out of the scale range are not displayed. It can be seen that the interior region of the brake disc b) displays the air temperature with higher temperatures than for the solid disc a). As it was shown in Figure 5.25 and Figure 5.26, the air flows in the vents inward heating up the center of the brake system and the wheel. Nevertheless, the temperature of the air near the rim is slightly higher for the case of the vented brake disc as shown below.



**Figure 5.27:** Air temperature for a) solid rotor b) vented rotor

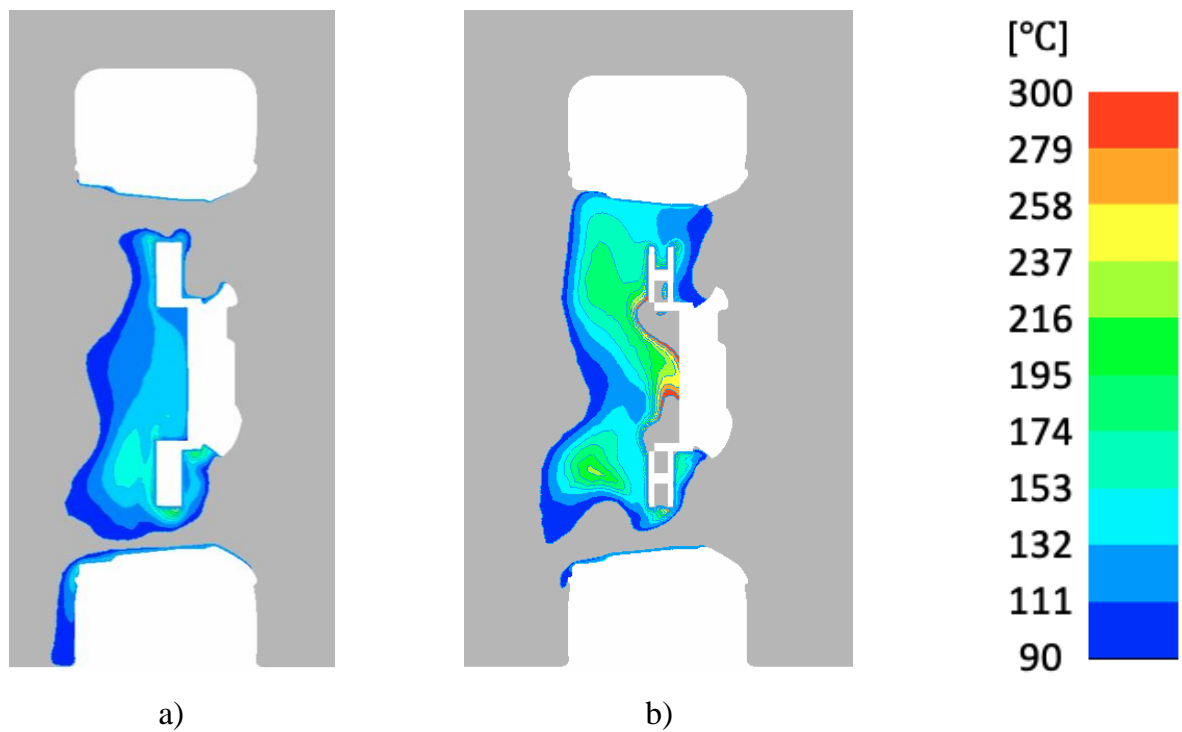


**Figure 5.28:** Air temperature for a) solid rotor b) vented rotor (Side View)

## CHAPTER 6

### CONCLUSION AND RECOMMENDATIONS

#### 6.1 Concluding Remarks

The modern personal vehicles are built with a brake system integrated right next to every wheel. Once the brake system is activated to slow down the vehicle, the friction forces between the brake pads and the brake disc generate heat, which is transferred to the surrounding air and the surrounding components of the vehicle. The convection and conduction are the major heat transfer processes that cool down the brake system. The radiative heat transfer plays an increasing role, when the brake discs reach critical temperatures, typically, 500 °C and above. At these temperatures some brake system components, especially, the one made of plastic based materials can be damaged. The reinforced thermoplastic composites are, increasingly, becoming more popular in the manufacturing of the automotive wheels, replacing the aluminum and steel alloys. The structural strength of the thermoplastic matrix, however, can be compromised at elevated temperatures. For some types of the thermoplastic matrices, the operation temperatures are below 200 °C.

The heat transfer phenomena on the brake discs have been investigated extensively in the past, however, not much work is published on the heat transfer between the brake discs and the wheel at critical brake disc temperatures. In this study, heat transfer phenomena on

the wheel-brake system were investigated. The aerodynamic effects, radiation, and convection heat transfer phenomena were numerically studied for various incoming air stream velocities and the brake disc temperatures. The conduction was simulated only on the rim with 10 mm rim thickness. The numerical investigation was performed using ANSYS Fluent.

The theoretical investigation revealed that the radiative heat transport is the dominant source of heating of the wheel's inner surface, while only insignificant heat transfer rate is transported by the circulating air stream per convection. The average temperature on the wheel inner surface increases with the increasing temperature of the brake disc and decreasing velocity of the vehicle. The average heat transfer coefficient on the inner surfaces of the rim increases with the increasing vehicle velocity and the increasing temperature on the inner surface of the rim. Similar trends were found for the average Nusselt number and the average heat flux on the rim. Also, it was found that the temperature on the inner rim surface reached the 200 °C limit for certain combinations of the incoming air stream velocity and the brake disc temperature. Finally, the heat transfer phenomena were compared for the cases of the brake disc with and without vents. It was found that the vents have insignificant impact on the heat transfer between the brake disc and the wheel. The vents transport the air from the outer to the inner vent end, which is a desirable effect for the reduction of the temperature on the inner surface of the wheel.

## 6.2 Recommendations for Future Work

- The numerical simulation performs the best when confirmed with the experimental observations on the physical system with the same initial and boundary conditions. Therefore, it is recommended to conduct a series of experiments to correlate the temperatures on the inner side of the wheel and the brake disc.
- The numerical model of the wheel-brake system was created with several geometrical simplifications. For computational feasibility, the vehicle was not included in the studied model, even though it would have a significant effect on the air stream profile around the brake system and, therefore, brake rotor cooling. It is recommended to incorporate the entire vehicle with suspension components in the numerical model for the more complete results.
- The current study was an initial investigation of the heat transfer on the wheel-brake system; however, the simulation can render more accurate results if modeled as a transient multi-cycle brake case. The numerical modelling of the conduction heat transfer on the wheel-brake-suspension system can be beneficial as well.
- The study was performed with an emissivity coefficient value of 0.64 as a most realistic case for this specific simulated system. However, it is reasonable to perform a sensitivity study for different emissivity coefficients, in order to estimate how the system responds on the wider range of the emissivity coefficients.

- Finally, more wheel designs with different numbers of spokes and different proximities of the rim to the brake disc would be interesting and useful to investigate. Some geometries, naturally, foster the air circulation around the brake system, while others may hinder it.

## APPENDIX A: Turbulent Fluxes

Turbulent fluxes and properties can be written as shown in the forthcoming equations

$$\tau_{tu} = \mu_{tu} \frac{\partial \bar{u}}{\partial y} = \rho E \frac{\partial \bar{u}}{\partial y} = -\rho \overline{u'v'} \quad (\text{A.1})$$

$$q''_{y,tu} = -k_{tu} \frac{\partial \bar{T}}{\partial y} = -\rho C_p E_{th} \frac{\partial \bar{T}}{\partial y} = -\rho C_p \frac{E}{Pr_{tu}} \frac{\partial \bar{T}}{\partial y} = -\rho C_p \overline{v'T'} \quad (\text{A.2})$$

$$\tau_{ij} = \rho(\nu + E) \left( \frac{\partial \bar{u}_j}{\partial x_i} + \frac{\partial \bar{u}_i}{\partial x_j} \right) \quad (\text{A.3})$$

$$q''_j = -\rho C_p \left( \frac{\nu}{Pr} + \frac{E}{Pr_{tu}} \right) \frac{\partial \bar{T}}{\partial x_j} \quad (\text{A.4})$$

The Reynolds-averaged conservation equations in Cartesian coordinates for an incompressible fluid are

$$\frac{\partial \bar{u}_i}{\partial x_i} = 0 \quad (\text{A.5})$$

$$\rho \frac{D\bar{u}_i}{Dt} = -\frac{\partial P}{\partial x_i} + \frac{\partial \tau_{ij,lam}}{\partial x_j} + \frac{\partial \tau_{ij,turb}}{\partial x_j} + \rho g_i \quad (\text{A.6})$$

$$\rho C_p \frac{D\bar{T}}{Dt} = \tau_{ij} \frac{\partial \bar{u}_i}{\partial x_j} - \frac{\partial q''_{i,lam}}{\partial x_i} - \frac{\partial q''_{i,tu}}{\partial x_i} + \Phi_{tu} \quad (\text{A.7})$$

## APPENDIX B: RANS Models Simulation Results (Front View)

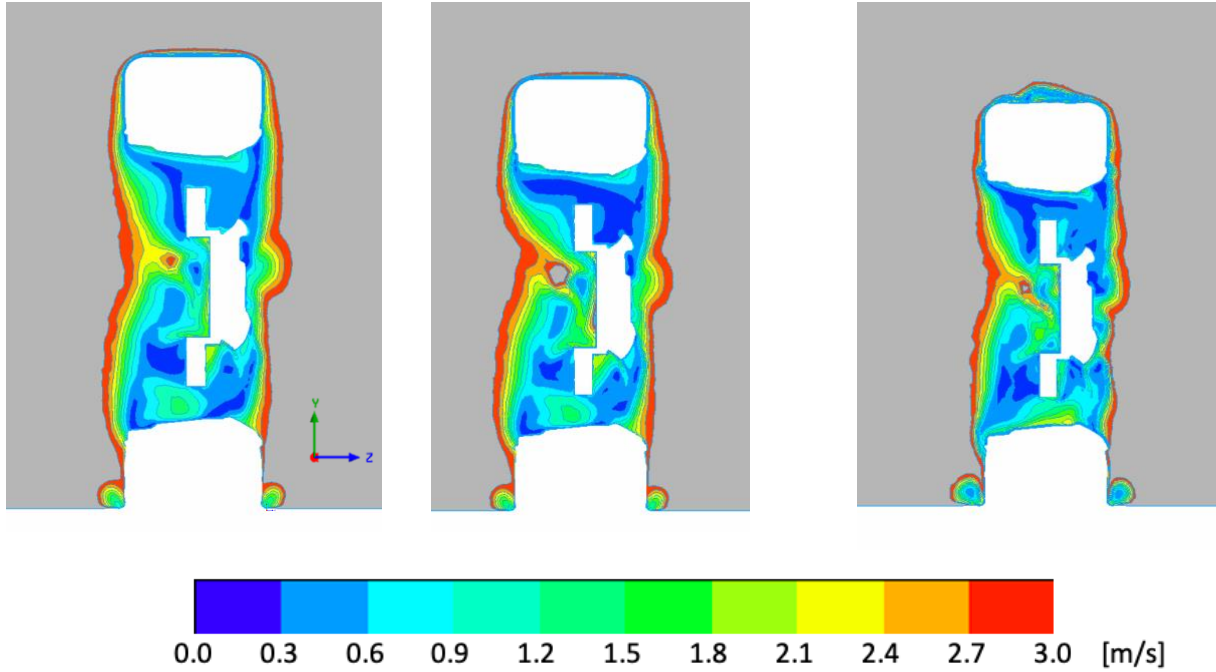


**Figure B.1:** Velocity profile for a) Realizable  $k - \epsilon$ , b) Standard  $k - \omega$  c) SST  $k - \omega$

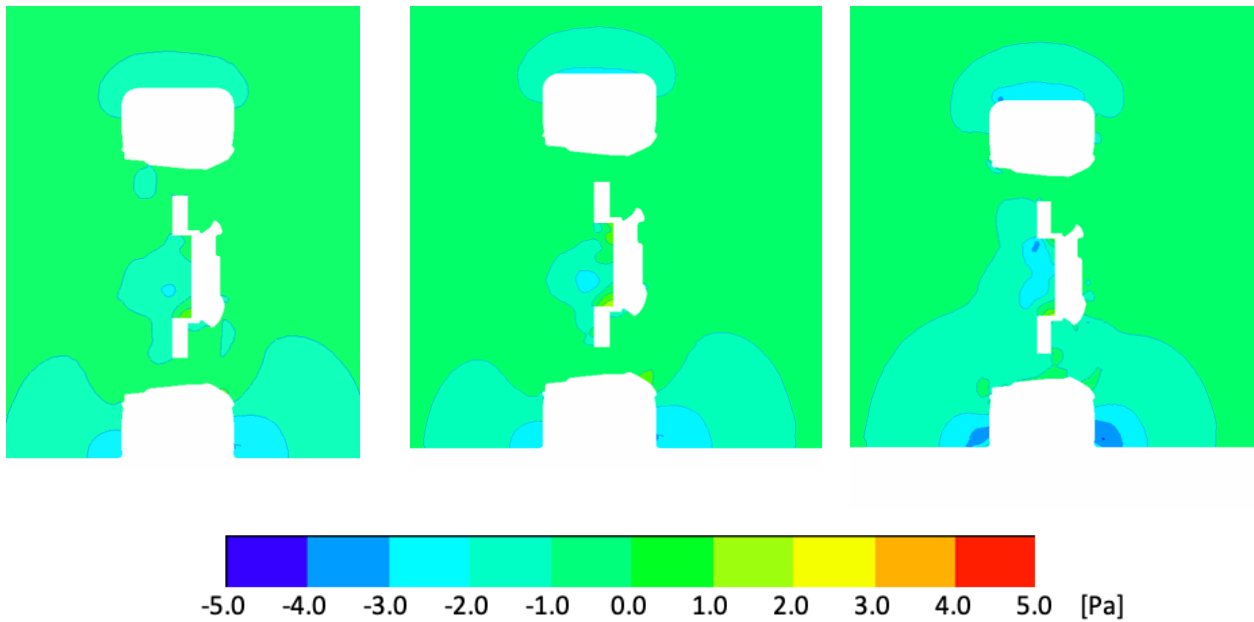


**Figure B.2:** Pressure profile for a) Realizable  $k - \epsilon$ , b) Standard  $k - \omega$  c) SST  $k - \omega$

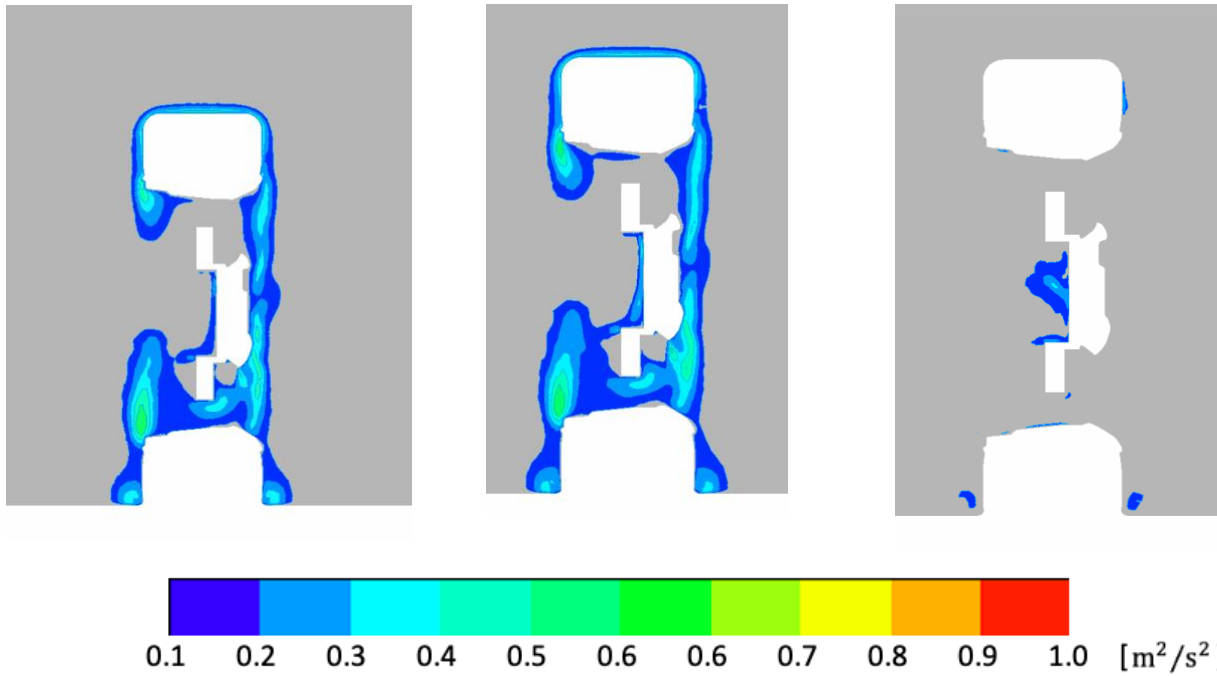


**Figure D.3:** Kinetic Energy profile for a) Realizable  $k - \epsilon$ , b) Standard  $k - \omega$  c) SST  $k - \omega$

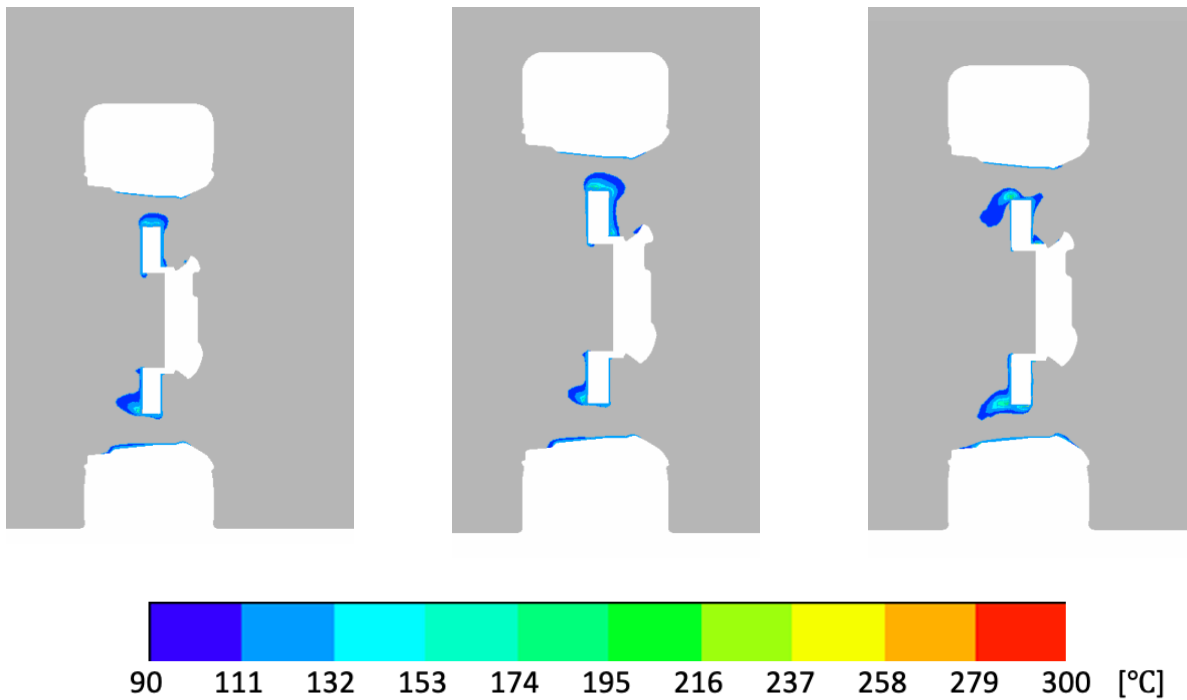


**Figure D.4:** Kinetic Energy profile for a) Realizable  $k - \epsilon$ , b) Standard  $k - \omega$  c) SST  $k - \omega$

## REFERENCES

- [1] J. Reimpell, *The Automotive Chassis: Engineering Principles* 2<sup>nd</sup> ed., Butterworth Heineman, 1986.
- [2] K. Reif, *Fundamentals of Automotive and Engine Technology*, Springer Vieweg, 2014.
- [3] G. Mom, *The Evolution of Automotive Technology: A Handbook*, SAE International, 2014.
- [4] W. Krenkel, *Ceramic Matrix Composites: Fiber Reinforced Ceramics and their Applications*, WILEY-VCH Verlag, 2008.
- [5] R. Limpert, *Brake Design and Safety* 3<sup>rd</sup> ed., SAE International, 2011.
- [6] P. Childs, *Mechanical Design Engineering Handbook*, Elsevier, 2014.
- [7] J. Wiedemann, *Progress in Vehicle Aerodynamics and Thermal Management*, Springer, 2017.
- [8] Plastics Today, Community for Plastics Professionals, “World’s First Thermoplastic Composite Wheel: Polyetherimide/Carbon Fiber Combination” Article, June 17, 2014.
- [9] [http://speed.academy/rotor-one-two-piece-how-to-choose-the-right-disc-brakes-for-your-needs-and-budget/?doing\\_wp\\_cron=1597869248.5564439296722412109375](http://speed.academy/rotor-one-two-piece-how-to-choose-the-right-disc-brakes-for-your-needs-and-budget/?doing_wp_cron=1597869248.5564439296722412109375)
- [10] <https://motorreview.com/new-chevy-camaro-tech/>
- [11] Stephens, A. Aerodynamic Cooling of Automotive Disc Brakes. Master’s Thesis, RMIT University, Melbourne, Australia, 2006.
- [12] A. Favre-Marinet, S. Tardu, *Convective Heat Transfer – Solved Problems*, Wiley, 2008.
- [13] R. Noyes, and P. Vickers. *Prediction of Surface Temperatures in Passenger Car Disc Brakes*, 1969.

- [14] A. Stephens, *Aerodynamic Cooling of Automotive Disc Brakes*, Thesis, 2006.
- [15] R. Limpert, *The Thermal Performance of Automotive Disc Brakes*. Automobile Engineering Meeting, Detroit Michigan, SAE, 1975.
- [16] R. Limpert, *Brake Design and Safety, Second Edition*, SAE International, 1999.
- [17] K. Cooper, *Bluff-Body Aerodynamics as Applied to Vehicles*. Second International Colloquium on Bluff Body Aerodynamics (BBAA II), Melbourne Australia, 1992.
- [18] R. Renz, *Integration of CMC Brake Disks in Automotive Brake Systems*, *International Journal of Applied Ceramic Technology*, Volume 9, Issue 4, 2012.
- [19] A. Sisson, *Thermal Analysis of Vented Brake Rotors*, SAE International, 1978.
- [20] W. Hucho, *Aerodynamics of Road Vehicles*, SAE, 1998.
- [21] A. Belhocine and M. Bouchetara, "Thermal Analysis of a Solid Brake Disc," *Applied Thermal Engineering* 32, 2012.
- [22] A. Kulkarni and R. Mahale, "Impact of Design Factors of Disc Brake Rotor on Braking Performance," *IJERT*, 2020.
- [23] W. Hunt, A. Price, S. Jelic, "A Coupled Simulation Approach to Race Track Brake Cooling for a GT3 Race Car," 11<sup>th</sup> FKFS Conference, Stuttgart. Springer, 2017.
- [24] T. Dekker and V. Krishnan, "Numerical Investigations of Brake Cooling Performance," Master's Thesis in Automotive Engineering, Chalmers, 2018.
- [25] R. Noyes and T. Vickers, "Prediction of Surface Temperatures in Passenger Car Disc Brakes," SAE International, 1969.
- [26] W. H. Giedt, Investigation of variation of point unit-heat-transfer coefficient around a cylinder normal to an air stream. *Trans. ASME* 71, 1949.

- [27] Y.A. Gengel and A.J. Ghajar, *Heat And Mass Transfer Fundamentals And Applications*, 5<sup>th</sup> ed., 2015.
- [28] S. M. Ghiaasiaan, *Convective Heat and Mass Transfer*, 2<sup>nd</sup> Edition, CRC Press, 2018.
- [29] A. Chandram, Numerical Investigation of Flow Past a Circular Cylinder and in a Staggered Tube Bundle Using Various Turbulence Models. Master's Thesis, Lappeenranta University of Technology, 2010.
- [30] D. Sofialidis, "Lecture 3 Turbulence Modeling, Heat Transfer and Transient Calculations," ANSYS, PRACE Autumn School 2013, September 21-27.
- [31] ANSYS FLUENT 12.1 Theory Guide, (2010).
- [32] H. K. Versteeg, and W. Malalasekera, *An introduction to computational fluid dynamics*, 2<sup>nd</sup> ed.. Prentice Hall, England, 2007.
- [33] "Matlab," ed: Mathworks Inc., 2019.
- [34] T. Shih, W. Liou, "A new k- $\epsilon$  eddy viscosity model for high reynolds number turbulent flows", *Computers & Fluids* Vol. 24, Issue 3, March 1995
- [35] Wilcox, D. C., *Turbulence Modeling for CFD*, 2nd edition, DCW Industries, Inc., La Canada CA, 1998.
- [36] Menter, F. R., "Two-Equation Eddy-Viscosity Turbulence Models for Engineering Applications," *AIAA Journal*, Vol. 32, No. 8, August 1994, pp. 1598-1605.